Analysis of co-registered bathymetric and sidescan data

Goodfellow, Iain T.

Award date:
1996

Awarding institution:
University of Bath

Analysis of co-registered bathymetric and sidescan data

Submitted by Iain T. Goodfellow

for the degree of Ph.D.
of the University of Bath

1996

ProQuest LLC
789 East Eisenhower Parkway
P.O. Box 1346
Ann Arbor, MI 48106-1346

Analysis of co-registered bathymetric and sidescan data

Submitted by Iain T. Goodfellow

for the degree of Ph.D.
of the University of Bath

1996

Abstract

This thesis presents the development of an acoustic model which is capable of seabed classification using co-registered bathymetric and sidescan sonar data from a calibrated Interferometric Sidescan Sonar. The data was from Plymouth Sound, England, and small datasets which had ground truthing associated with them were examined. A 117 kHz and 234 kHz Interferometric Sidescan Sonar was used.
The motivation behind this work was to generate a tool which could use co-registered sidescan sonar data to generate easy to understand colour coded contour plots of the backscatter coefficients, generated by the acoustic model, with the topographic effects removed.

The thesis shows, for a small area of seabed, how the acoustic model utilises the co-registered data, the motion of the sidescan sonar, directivity of the transducers and the calibration of the system. The area of seabed under investigation is gridded and each nodal point on the grid has a backscatter coefficient and a grazing angle value associated with it. A method is presented which uses the co-registered data to calculate the grazing angles associated with each backscatter coefficient using vector cross-product and dot products. Using a method developed in this thesis the grazing angle dependency is removed and the resultant backscatter coefficient values presented.

The benefits of this model is an easy to use method for classifying the seabed, and an easy to understand graphical displays. The resultant data can be either presented in the usual two dimensional line plot, or a more relevant colour coded contour plot, which can represent a small area of seabed where the sidescan sonar moves a few metres, or large areas of seabed where the seabed type might change.

The acoustic model successfully detected different seabeds using the real-time data, with higher backscatter coefficients calculated for seabed types which have a large mean grain size, such as Gravel, and low backscatter coefficients for seabed types which have a small mean grain size, such as Mud.

Acknowledgements

I am sincerely grateful to my Supervisor Dr. Nick Pace, especially for his enthusiasm and guidance throughout the project and for making the internet connection work.

I would also like to thank Dr. Victor Humphrey and Dr. Andy Baker for the discussions and help during this project.

I am indebted to Submetrix, and especially Matt Geen for supplying me with the sidescan and calibration data from their systems.

This project wouldn't have been feasible without the SUN Workstation supplied by the Defence Research Agency, thank you.

Many thanks go to Mark Prior, Steven Taylor, Stuart and Janeen Linsley for being there to supply distractions and enlightenment in even measures.

A special thank you has to go to the members of the School of Physics, both past and present, for providing such a pleasant working environment, especially Mair Jones, Barry Ward and Barbara Brooks for proof-reading this document.

Finally, I am very grateful for the support and encouragement from my mother, father, Carole, Anthony, Auntie Jenny and the little chap, Sean.

Abstract i
Acknowledgments ii

Chapter 1: Objectives and Literature review 1
1.1 Objectives 1
1.2 Literature Review 3

Chapter 2: Backscatter of sound from the ocean bottom 7
2.1 Introduction 7
2.2 Backscattering of sound 8
2.3 Seabed inhomogeneities. 9
2.4 Determination of Seabed Roughness 10
2.5 Seabed roughness 12
2.6 Lamberts Law 14
2.7 Slightly rough surfaces: 'Perturbation' theories 15
2.8 Kirchoff theory 15
2.9 Composite Model - Perturbation-Kirchoff model 17
2.10 Experimental 20
2.11 Summary 29
Appendix 2.1 A2-1

Chapter 3: Sidescan Sonar 30
3.1 Introduction 30
3.2 Basic introduction to the operation and principles of Sidescan 30
3.3 Sidescan Sonar 34
3.4 Sonar equations 37
3.4.1 Introduction 37
3.4.2 Sonar equation 37
3.4.2.1 Parameters determined by the sonar system 37
3.4.2.2 Parameters determined by the seabed 38
3.4.2.3 Parameters determined by the environments 38
3.5 Interferometric Seabed Inspection Sonar (ISIS) 40
3.5.1 Introduction 40
3.5.2 Background 40
3.5.3 Basic theory of Interferometric side-scan sonar 41
3.5.4 Accuracy 45
3.6 Errors 46
3.6.1 Interference 46
3.6.2 Changes in the speed of sound 48

Chapter 4: Towfish Motion 50
4.1 Attitude system output summary 50
4.2 Roll 53
4.3 Pitching 53
4.4 Yaw 54
4.5 Variable ship speeds 55
4.6 Sidescan sonar motion 55
4.7 Errors 56

Chapter 5: Acoustic Model 57
5.1 Introduction 57
5.2 Generating the Acoustic Model 57
5.2.1 Source Level 58
5.2.2 Transmission Loss 58
5.2.3 Seabed backscatter Strength 58
5.2.4 Using the sonar equations to build the resulting linear equation 59
5.3 Parameters which make up the acoustic model 60
5.3.1 Area of seabed insonified - A(t) 60
5.3.2 Intensity out from the source - Io 61
5.3.3 Sidescan data - S(t) 61
5.3.4 Beam Pattern - B 62
5.4 Overview of data processing 63

Chapter 6: Datafiles and processing 64
6.1 Introduction 64
6.2 Overview of the computer hardware and software used 64
6.2.1 Computer hardware 64
6.2.2 Software 65
6.3 Overview of data supplied by Submetrix 65
6.3.1 Bathymetric datafile 65
6.3.2 Backscatter amplitude datafile 66
6.4 Problems encountered with the datafiles supplied by Submetrix 67
6.4.1 Overview of data supplied by Submetrix 67
6.4.2 117kHz datasets 67
6.4.3 234kHz datasets 68
6.5 Overview of the processing software. 70
6.6 Pre-processing routines. 70
6.7 Implementation of the acoustic model 73
6.8 Theory for calculating local seabed normal 75
6.8.1 Resulting plots from equation 6.6 77
6.9 Theory for angle fish makes to local seabed normal. 79
6.9.1 Calculating vector from seabed to the sidescan sonar using above nomenclature 79
6.9.2 Normalising the x, y, z components of the sidescan sonar vector 80
6.9.3 Results for the calculation of the vector from the fish to the grid point on the seabed. 82
6.10 Calculating the Backscatter coefficient 85
6.11 Removal of the grazing angle dependency 90

Chapter 7: Results 94
7.1 Introduction 94
7.2 Plot of Plymouth Sound with key to symbols 96
7.2.1 Key to the symbols representing seabed types 96
7.3 117 kHz dataset - Overview of Track 1 97
7.3.1 Results for seabed type: Mud 98

7.3.2 Plots covering all of Track 1 data 101
7.4 117 kHz dataset - Overview of Track 2 103
7.4.1 Results for seabed type: Gravel 104
7.4.2 Results for seabed type: Shell 107
7.4.3 Results for seabed type: Gravel/Shell/Sand 110
7.5 234 kHz dataset - Overview of Track 3 113
7.5.1 Plots covering all of Track 3 data 114
7.6 234 kHz dataset - Overview of Track 4 116
7.6.1 Results for seabed type: Sand/broken Shell/Gravel 117
7.6.2 Results for seabed type: Mud 120
7.6.3 Plots covering all of Track 4 data 123
7.7 234 kHz dataset - Overview of Track 5 125
7.7.1 Results for seabed type: Sand 126
7.7.2 Results for seabed type: fine Sand/Mud
129
7.7.3 Plots covering all of Track 5 data 132
7.8 Summary of the results for the 117 kHz Port dataset 134
7.9 Summary of the results for the 117 kHz Starboard dataset 137
7.10 Summary of the backscatter coefficients for the starboard datasets 140
7.11 Discussion of the results 141

Chapter 8: Summary and Conclusion 144

References 152

List of Figures

Figure 2.1: A schematic showing how a sound wave upon interaction with a rough seabed and its inhomogeneities, can result in forward and backscatter. 9
Figure 2.2: A schematic diagram showing the phase difference between two parallel rays scattered from different points on the surface. 10
Figure 2.3: Three cases of seabed roughness, a) flat b) semi-rough and c) rough seabed to show the difference in specular energy. Ogilvy, 1991. 12
Figure 2.4: Schematic to show grazing angle for a monostatic case 14
Figure 2.5: Seabed surface which consists of small amplitude fluctuations superimposed on a slowly varying roughness. 18
Figure 2.6: Graph of backscatter strength versus grazing angle. Jackson 1986 19
Figure 2.7: Average curves for different seabed types consisting of backscatter strength as a function of grazing angle. McKinney 1964. 23
Figure 2.8: Backscatter strength versus grazing angle for a clay seabed. Wong and Chesterman 1968. 24
Figure 2.9: Backscatter strength versus grazing angle for a Silt seabed. Wong and Chesterman,1968. 24
Figure 2.10: Backscatter strength versus grazing angle for a Sand seabed. Wong and Chesterman, 1968. 25
Figure 2.11: Backscatter strength versus grazing angle for a Rock seabed. Wong and Chesterman, 1968. 25
Figure 3.1: A schematic diagram showing the basic elements in any active sonar. 30
Figure 3.2: Block diagram of the sonar electronics and computer hardware used in a modern sidescan sonar 32
Figure 3.3: Block diagram of the real time and post-processing software required in a modern sidescan sonar 33
Figure 3.4: The sidescan sonar is seen emitting a ping. The ping insonifies a narrow strip of the seabed called a swath. 35
Figure 3.5: Geometry of the sound wave upon interaction with the sea-bed. de Moustier, 1993. 36
Figure 3.6: Schematic to illustrate sonar equation parameters 39
Figure 3.7: Arrangement of transducers relative to a flat seabed 41
Figure 3.8: Detailed view of wavefront arriving at the transducers 42
Figure 3.9: Phase angle against Elevation angle for incident wavefront, with a tranducer spacing of half a wavelength. 43
Figure 3.10: Phase angle against Elevation angle of incident wavefront, with a transducer spacing of one wavelength. 44
Figure 3.11: Phase angle against Elevation angle of incident wavefront, with a transducer spacing of two wavelengths. 44
Figure 3.12: Geometry relating the declination angle error to depth error 45
Figure 3.13: Acoustic interference will have an effect on the returning wavefront. The locus of the constant phase will no longer be a pure circle, but one with irregular corrugations. 47
Figure 4.1: Schematic of the geographical axis of the sidescan sonar with the directions the transducers on the sidescan can move. 51

Figure 4.2: Difference in the location on the transmit footprint and the location of the received footprint. 52
Figure 4.3: Beam coverage as the sidescan sonar rolls from left to right, the first picture is with the sidescan sonar steady, the middle picture is with the sidescan sonar rolling to the left, and the final picture is with the sidescan sonar rolling to the right. Bell, 1995. 53
Figure 4.4: Schematic of the effects of pitch can have on the area of seabed covered. The first picture shows the sidescan sonar in a steady state, the middle picture shows the sidescan sonar pitching downwards and scanning behind itself and the final picture shows the sidescan sonar pitching upwards which causes it to scan
ahead of itself. Bell, 1995. 54
Figure 4.5: A plan view of the sidescan sonar to show the effects of yaw on the area of seabed covered. The first picture shows the sidescan sonar in a steady state, the middle picture shows the result of the sidescan sonar yawing to the right, and the final picture shows the sidescan sonar yawing to the left.
Bell, 1995. 55
Figure 4.6: Schematic to show the effects of changes in sidescan sonar speeds. The left hand picture shows the sidescan sonar being towed at a slow speed, whilst the right hand picture shows the results of the sidescan sonar being towed at a faster speed. Bell, 1995. 56
Figure 5.1: A schematic diagram to show the relation between the source and the area of seabed insonified. 57
Figure 5.2: Schematic to show the geometry of the pulse. 60
Figure 5.3: Typical beam pattern for sidescan system used 62
Figure 6.1: A schematic diagram illustrating the conversion required to seabed depth recorded to seabed depth relative to the lowest tide recorded. 65
Figure 6.2: Contoured plot of backscatter coefficients to show high backscatter coefficients at the end of the swaths. 68
Figure 6.3: The plot shows how the backscatter amplitude values recorded on the sidescan sonar has a dynamic range of 25dB. The seabed bathymetry had to be clipped in range window to correspond to the end of the good backscatter amplitude data. 69
Figure 6.4: Plot of the backscatter amplitudes against slant range to show how the returned signal has been clipped when the 75dB gain was applied to the signal. 69
Figure 6.5: Plot of the raw seabed depth data for area of seabed under investigation. 71
Figure 6.6: Plot of the seabed depth data after being filtered. 71
Figure 6.7: Flow chart of the pre-processing software. 72
Figure 6.8: A plot showing the seabed positions with a regular grid overlaid. 74
Figure 6.9: Plot of the seabed data after it has been triangulated and trigridded to generate a regular dataset. 74
Figure 6.10: A schematic representation of the regular grid and the latitude, longitude and depth data points. 75
Figure 6.11: A schematic diagram showing the positions of the local seabed normals on the regular grid. 76
Figure 6.12: The local seabed normals for the x-axis calculated from equation 6.6. 77
Figure 6.13: The local seabed normals for the y-axis calculated from equation 6.6. 78
Figure 6.14: The local seabed normals for the z-axis calculated from equation 6.6. 78

Figure 6.15: A schematic showing the orientation of the sidescan sonar with respect to the regular grid on the seabed. 79
Figure 6.16: A schematic diagram showing the vector, q, from the seabed to the sidescan sonar. 80
Figure 6.17: A schematic diagram of the result of both the local seabed normals and the normalised vector from the seabed to the sidescan sonar 81
Figure 6.18: A plot of the vector from the seabed to the sidescan sonar for the x-axis 82
Figure 6.19: A plot of the vector from the seabed to the sidescan sonar for the y-axis 83
Figure 6.20: A plot of the vectors of the seabed to the sidescan sonar for the z-axis 83
Figure 6.21:A plot of the resulting grazing angles calculated using the dot product shown in equation 6.13, and then subtracting this angle from 90 degrees. 84
Figure 6.22: A coloured contour plot of the seabed under investigation. 85
Figure 6.23: A plot of the backscatter amplitude against slant range. This shows all the backscatter amplitude data associated with one acoustic ping. The data between about 25 metres and 78 metres would be used in the acoustic model. 86
Figure 6.24: A plot of the size of the area on the seabed insonified by the beam. This is calculated using equation 5.10 in Section 5.3.1. 86
Figure 6.25 A plot of the combined beam pattern used to account for the directivity of the transducers. 87
Figure 6.26: A plot of the backscatter coefficient values against grazing angle calculated using the acoustic model developed in section 5.2.4. 87
Figure 6.27: A plot of the mean backscatter coefficients against grazing angle. This was calculated by summing all the backscatter coefficient values in a 1 degree window and then dividing the result by the number of points used. 88
Figure 6.28: A histogram of the range of grazing angles used. The number of low grazing angles will be limited by the problems discussed in section 6.4.3. 88
Figure 6.29: Contoured plot of the backscatter coefficient values from Figure 6.26. As a regular grid is employed the Easting and Northings can be used to generate a contour plot of the resulting backscatter coefficients over the area of seabed covered.. 89
Figure 6.30: Plot of the range of offset values used to relate the original backscatter coefficients to the selected mean backscatter coefficient value. 92
Figure 6.31: A plot of the Backscatter Coefficients corrected to the mean backscatter coefficient value at a grazing angle of 50 degrees. 93
Figure 6.32: Contoured plot of the Backscatter values relative to the mean backscatter coefficient value at 50 degrees, thus removing the grazing angle dependency. 93
Figure 7.1: A plot of Plymouth Sound with the ground truthing overlaid. 94
Figure 7.2: Schematic of Plymouth Sound, with seabed types and Track 1 overlaid. For key to seabed symbols see section 7.2.1. 98
Figure 7.3: A plot of seabed depths with sidescan sonar positions overlaid. 98
Figure 7.4: Contour plot of seabed under investigation. Seabed type: Mud. 99
Figure 7.5: A plot of Backscatter Coefficient against Grazing Angle. Seabed type: Mud. 99
Figure 7.6: A plot of Mean Backscatter Coefficient against Grazing Angle. Seabed type: Mud. 100
Figure 7.7: Contoured plot of Backscatter Coefficients. Seabed type: Mud. 100

Figure 7.8: Contour plot of Backscatter Coefficients with the grazing angle dependency removed. The backscatter values are relative to a grazing angle of 25 degrees. Seabed type: Mud. 101
Figure 7.9: Colour coded plot of the backscatter coefficients along Track 1. Each point represents the average backscatter value over all grazing angles for 10 pings. 102
Figure 7.10: Contour plot of the seabed bathymetry for Track 1. 102
Figure 7.11: Contour plot of the backscatter coefficients along Track 1, this was achieved by using a sliding window technique. 103
Figure 7.12: Contour plot of the backscatter coefficients with the grazing angle dependency removed. These backscatter coefficient values are relative to the backscatter coefficient value at the middle grazing angle. 103
Figure 7.13: Schematic of Plymouth Sound, with the seabed types and Track 2 overlaid. For key to symbols , see section 7.2.1. 104
Figure 7.14: A plot of the seabed depths with the sidescan sonar positions overlaid 104
Figure 7.15: Contoured plot of seabed under investigation. Seabed type: Gravel. 105
Figure 7.16: A plot of Backscatter Coefficients against Grazing Angle. Seabed type: Gravel. 105
Figure 7.17: A plot of Mean Backscatter Coefficients against Grazing Angle. Seabed type: Gravel. 106
Figure 7.18: Contoured plot of Backscatter Coefficients. Seabed type: Gravel 106
Figure 7.19: Contoured plot of Backscatter Coefficients with the grazing angle dependency removed. The backscatter values are relative to a grazing angle of 28 degrees. Seabed type: Gravel. 107
Figure 7.20: Contoured plot of seabed under investigation. Seabed type: Shells 108
Figure 7.21: A plot of Backscatter Coefficients against Grazing Angle. Seabed type: Shells 108
Figure 7.22: A plot of Mean Backscatter Coefficients against Grazing Angle. Seabed type: Shells 109
Figure 7.23: Contoured plot of the backscatter Coefficients. Seabed type: Shells 109
Figure 7.24: Contoured plot of the Backscatter Coefficients with the grazing angle dependency removed. The backscatter values are relative to a grazing angle of 26 degrees. Seabed type: Shells. 110
Figure 7.25: Contoured plot of the seabed under investigation. Seabed type: Gravel/Shells/Sand 111
Figure 7.26: A plot of Backscatter Coefficients against Grazing Angle. Seabed type: Gravel/Shells/Sand 111
Figure 7.27: A plot of Mean Backscatter Coefficients against Grazing Angle. Seabed type: Gravel/Shells/Sand 112
Figure 7.28: Contoured plot of the Backscatter Coefficients. Seabed type: Gravel/Shells/Sand 112
Figure 7.29: Contoured plot of the Backscatter Coefficients with the grazing angle dependency removed. The backscatter values are relative to a grazing angle of 30 degrees. Seabed type: Gravel/Shells/Sand. 113
Figure 7.30: Schematic of Plymouth Sound, with seabed types and Track 3 overlaid. For key to symbols see section 7.2.1. 114
Figure 7.31: A plot of seabed depths with sidescan sonar positions overlaid. 114
Figure 7.32: Colour coded plot of Backscatter coefficient values along Track 3.

Each point represents the average backscatter value over all grazing angles for 10 pings. 115
Figure 7.33: Contoured plot of the seabed bathymetry for all of Track 3. 115
Figure 7.34: Contoured plot of Backscatter Coefficients along Track 3, this was achieved by using a sliding window technique. 116
Figure 7.35: Contour plot of the backscatter coefficients with the angle dependency removed. These backscatter coefficient values are relative to the backscatter coefficient value at the middle grazing angle. 116
Figure 7.36: Schematic of Plymouth Sound, with seabed types and track 4 overlaid. For key to seabed symbols see section 7.2.1. 117
Figure 7.37: A plot of seabed depths with sidescan sonar positions overlaid. 117
Figure 7.38: Contour plot of seabed under investigation.
Seabed type: Sand/Broken Shell/Gravel. 118
Figure 7.39: A plot of Backscatter Coefficients against Grazing Angle.
Seabed type: Sand/broken Shells/Gravel. 118
Figure 7.40: A plot of Mean Backscatter Coefficient against Grazing Angle.
Seabed type: Sand/broken Shells/Gravel. 119
Figure 7.41: Contoured plot of Backscatter Coefficients.
Seabed type: Sand/broken Shells/Gravel. 119
Figure 7.42: Contoured plot of the Backscatter Coefficients with the grazing angle dependency removed. The backscatter values are relative to a grazing angle of 29 degrees. Seabed type: Sand/broken Shells/Gravel. 120
Figure 7.43: Contour plot of seabed under investigation. Seabed type: Mud. 121
Figure 7.44: A plot of Backscatter Coefficients against Grazing Angle.
Seabed type: Mud. 121
Figure 7.45: A plot of Mean Backscatter Coefficients against Grazing Angle.
Seabed type: Mud. 122
Figure 7.46: Contoured plot of Backscatter Coefficients. Seabed type: Mud. 122
Figure 7.47: Contoured plot of the Backscatter Coefficients with the grazing angle dependency removed. The backscatter values are relative to a grazing angle of 47 degrees. Seabed type: Mud. 123
Figure 7.48: Colour coded plot of backscatter coefficient values along Track 4. Each point represents the average backscatter value over all grazing angles for 10 pings. 124
Figure 7.49: Contoured plot of the seabed bathymetry for all of Track 4. 124
Figure 7.50: Contoured plot of the Backscatter Coefficients along Track 4, this was achieved by using a sliding window technique. 125
Figure 7.51: Contour plot of the Backscatter Coefficients with the grazing angle dependency removed. These backscatter values are relative to the backscatter coefficient value at the middle grazing angle. 125
Figure 7.52: Schematic of Plymouth Sound, with seabed types and Track 5 overlaid. For key to seabed symbols see section 7.2.1. 126
Figure 7.53: A plot of seabed depths with sidescan sonar positions overlaid. 126
Figure 7.54: Contour plot of the seabed under investigation. Seabed type: Sand 127
Figure 7.55: A plot of Backscatter Coefficients against Grazing Angle.
Seabed type: Sand 127
Figure 7.56: A plot of Mean Backscatter Coefficients against Grazing Angle.
Seabed type: Sand 128

Figure 7.57: Contoured plot of the Backscatter Coefficients. Seabed type: Sand 128
Figure 7.58: Contoured plot of the Backscatter Coefficients with the grazing angle dependency removed. The backscatter values are relative to a grazing angle of 43 degrees. Seabed type: Sand. 129
Figure 7.59: Contour plot of the seabed under investigation. Seabed type: fine Sand/Mud 130
Figure 7.60: A plot of the Backscatter Coefficients against Grazing Angle. Seabed type: fine Sand/Mud 130
Figure 7.61: A plot of the Mean Backscatter Coefficients against Grazing Angle. Seabed type: fine Sand/Mud 131
Figure 7.62: Contoured plot of the Backscatter Coefficients. Seabed type: fine Sand/Mud 131
Figure 7.63: Contoured plot of the Backscatter Coefficients with the grazing angle dependency removed. The backscatter values are relative to a grazing angle of 46 degrees. Seabed type: fine Sand/Mud. 132
Figure 7.64: Colour coded plot of backscatter coefficient values along Track 5. Each point represents the average backscatter value over all grazing angles for 10 pings. 133
Figure 7.65: Contour plot of the seabed bathymetry for all of Track 5. 133
Figure 7.66: Contoured plot of the backscatter coefficients along Track 5, this was achieved by using a sliding window technique. 134
Figure 7.67: Contour plot of the backscatter coefficients with the grazing angle dependency removed. The backscatter coefficient values are relative to the backscatter coefficient value at the middle grazing angle. 134
Figure 7.68: Contour plot of Backscatter Coefficients with the grazing angle dependency removed. The backscatter values are relative to a grazing angle of 25 degrees. Seabed type: Mud. 135
Figure 7.69: Contoured plot of Backscatter Coefficients with the grazing angle dependency removed. The backscatter values are relative to a grazing angle of 28 degrees. Seabed type: Gravel. 136
Figure 7.70: Contoured plot of the Backscatter Coefficients with the grazing angle dependency removed. The backscatter values are relative to a grazing angle of 30 degrees. Seabed type: Gravel/Shell/Sand. 136
Figure 7.71: Contoured plot of the Backscatter Coefficients with the grazing angle dependency removed. The backscatter values are relative to a grazing angle of 26 degrees. Seabed type: Shell. 137
Figure 7.72: Summary of the backscatter coefficients for the 117 kHz Port dataset. 137
Figure 7.73: Contoured plot of the Backscatter Coefficients with the grazing angle dependency removed. The backscatter values are relative to a grazing angle of 47 degrees. Seabed type: Mud. 138
Figure 7.74: Contoured plot of the Backscatter Coefficients with the grazing angle dependency removed. The backscatter values are relative to a grazing angle of 46 degrees. Seabed type: fine Sand/Mud. 138
Figure 7.75: Contoured plot of the Backscatter Coefficients with the grazing angle dependency removed. The backscatter values are relative to a grazing angle of 43 degrees. Seabed type: Sand. 139

Figure 7.76: Contoured plot of the Backscatter Coefficients with the grazing angle dependency removed. The backscatter values are relative to a grazing angle of 29 degrees. Seabed type: Sand/broken Shell/Gravel. 139
Figure 7.77: Summary of the backscatter coefficient values for the 234 kHz Port dataset. 140
Figure 7.78: Summary of the backscatter coefficient values for the 117 kHz Starboard dataset. 141
Figure 7.79: Summary of the backscatter coefficient values for the 234 kHz Starboard dataset. 141

Chapter 1

Objectives and Literature review

1.1 Objectives

This thesis presents a method for classifying the seabed using the combined characteristics of both bathymetric and backscatter amplitude data. Previous attempts at characterising and classifying the seabed geology have used either the bathymetric or backscatter amplitude data, but not both.

Bathymetric classification methods such as McKinney and Anderson, 1968, Jackon D.R., 1994, work on only a relatively coarse scale as they require large amounts of data to gather statistics of seabed type, which is commonly defined in terms of the shape of the spatial power spectra of the topography. Conversely, backscatter amplitude methods such as Pace N.G. and Dyer C., 1979 and Edgecock T.M., 1994, are capable of resolving smaller features, but, they lack the information base that the bathymetry provides, since seafloor shape is a very important indication of the seabed type.

The amplitude of the backscattered sonar signal is a function of the sensor geometry, seabed topography, and the physical properties of the seabed, it is essential to obtain accurate measurements of all three parameters for a complete characterisation of the seabed.
The Interferometric sidescan sonar developed by Submetrix* , is able to generate a calibrated dataset of co-registered bathymetric and backscatter amplitude data along with the environmental data of the sidescan itself, that is roll, pitch, yaw.

* Submetrix, Minerva House, Lower Bristol Road, Bath, England BA2 9ER

With this knowledge of the backscatter amplitude, bathymetry, together with ground truthing an acoustic model was developed which calculated the backscatter coefficients for different areas of seabed over a range of grazing angles, and these values were shown to be able to distinguish between different seabed types.

1.2 Literature Review

The technical base for sidescan sonar was developed during the anti-submarine warfare effort of World War 2. Advances in the science and technique were beginning to concentrate on the medium and its boundaries but, it was not until 1958 that the first open publication in the field drew attention to the fact that bottom reverberation could be presented in such a way as to be of great value to seabed geology, Chesterman *et al* 1958, and the first application paper, Stride 1959, appeared a year later.

In 1961 the Institute of Oceanographic Sciences (formerly the National Institute of Oceanography) published a paper on the results of a sea trial where they took a newly designed sidescan, Tucker and Stubbs, 1961.

Meanwhile in the USA there was a mention of a side scan sonar by Hersey in a pre-print in the Instrument Society of America in 1960, Hersey *et al* 1960. In 1961, the house journal of the Alden company cited this reference in connection with their equipment. The first major scientific paper based primarily on sidescan sonar was by Donovan and Stride 1961.

In parallel with the interest in qualitative information of the sea revealed by sidescan sonar, there was a growth of interest in numerical bathymetry for scientific and commercial use, both in the deep sea and shelf waters, this stimulated much research in Swathe Bathymetry. The idea of swathe soundings has been put forward by a number of authors, Haines 1970, Ritchie 1970a, and accompanied by a number of paper solutions Ritchie 1970b, Tucker 1960. The first idea was to take a number of basic echo sounders and arrange them in a line athwartship, this generated a line of individual seabed depths.

A higher density of readings over a narrow swathe was obtained by Fahrentholz 1963, by the use of 25 transducers on outriggers on each side of the ship. Another approach was to use a transducer arrangement which provides a number of beams directed at different angles from the vertical. This was first put forward by Tucker 1960, and demonstrated by Howson and Dunn 1961. One of the difficulties of this otherwise simple system was

identifying the beams; by making the beam sensitivities unequal, Tucker 1961, showed that beam identification could be simplified.

Throughout the 1960's and early 1970's work was carried out on these multibeam systems, refining beam patterns, data collection techniques and generally improving the accuracy and expanding the use of them, Hickley 1966, Glenn 1970, Beldenson 1972.

Whilst using these multibeam systems it was noted that, during calm weather a side-scan sonar picture was modulated with alternate light and dark bands, orientated substantially parallel to the track. These bands were parallel to one another when received from a flat seafloor but, when topographical features are present, deviate in sympathy with their rise and fall. Investigations indicated that an interference effect took place as a result of the reflection of the sound from the sea surface, Haines 1963. This became known as the Lloyd-Mirror effect due to its similarity to the optical phenomenon. Chesterman *et al* 1967 and Heaton and Haslett 1971, have shown how depth profiles may be extracted from these Lloyd-Mirror fringes on sonographs and Greischar and Clay 1972, extended the method and produced a contour chart.

The main disadvantage of the natural Lloyd-Mirror effect, for any practical survey system, is that it does not occur often because the sea surface is too rough and the reflected sound is incoherent. One idea to overcome this limitation was to put a plane acoustic reflector over the transducer to produce the Lloyd-Mirror effect independent of sea-state and thus location and season.

Another idea was the Telesounder, Stubbs 1974. Telesounding was the name given to wide swathe measurements of seabed depths. This system replaced the acoustic reflector with another transducer, this arrangement may now be considered to be a two-element array with the well known multiple beam diffraction, or interferometer, pattern. In this form the Telesounder is very similar to the interferometer of Howson and Dunn 1961, but turned to work sideways instead of downwards.

One limitation of the Telesounder was that the angular distribution of the fringes must be known in advance. The first system published to resolve the multiple ambiguity among the fringes was by Denbigh 1983. The BAthymetric Side-scan Sonar (BASS), was an interferometer producing less than one fringe and exploiting the change of phase between the two interfering signals across the single broad fringe. The BASS system gives a rapid measurement of the acoustic backscattered amplitude from a large area of the seabed but it also and simultaneously measures the depth of the seabed. The depth is calculated from the phase difference between two closely spaced receivers, Denbigh 1977, 1979, Shishido 1979, Denbigh, 1980, 1981, 1983, Gapper and Hollis, 1985. The main practical difficulties of the single fringe system lies in extracting a smooth phase difference between two rapidly changing signals, which, are themselves corrupted by noise, Shensa 1978, Matsumoto 1990, Alexandrou 1992, Masnadi-Shirazi 1992.

Since its development, the interferometric sidescan sonar has been used in measurements such as bathymetry, providing qualitative information on the relief, acoustic imaging, which is most often used in a qualitative sense for geomorphology and for feature detection of obstacle avoidance, and acoustic bottom loss which is related to the physical properties of the substrate.

Recently bathymetric measurements and seafloor acoustic imaging have been performed with swathe mapping sonars such as phase interferometry techniques, Cloet 1985, Cloet 1986, Davis 1986, de Moustier 1988, 1990a, Denbigh 1989, Babb 1989, Lesnikowski 1989, Robinson 1989 and Geen 1993.

The raw information collected by the interferometric sonar is seafloor acoustic backscatter versus time and angle of arrival, and the character of these signals is dictated, for the most part by the material properties of the substrate and by the micro-relief in the area insonified. Therefore, it should be possible to use this information to remotely classify seafloor types. A large number of acoustic experiments have been carried out on the seafloor to determine the dependence of backscattering coefficient on the angle of incidence , bottom type (roughness and acoustic impedance), and acoustic frequency, McKinney and Anderson, 1964, Wong and Chesterman, 1968, Smailes, 1978, Bunchuk

and Zhitkovski, 1980, Chotiros *et al*, 1985, Boehme *et al*, 1985, Jackson *et al*, 1986a, Jackson *et al*, 1986b, Boehme and Chotiros, 1988, Stanic *et al*, 1988, Mourad and Jackson, 1989, Stanic *et al*, 1989, Nicholls M.J, 1991, Jackson and Briggs, 1992, Stewart and Chotiros, 1992, Chotiros N.P., 1994, Jackson, 1994, Kalra and Fulford, 1994,

Various attempts have been made to derive quantitative seafloor acoustic backscatter information from conventional sidescan sonar systems, Pace and Dyer, 1979, Reut *et al* 1985, Pace and Gao 1988, Reed and Hussong 1989, Beck R. A, 1991, Alexandrou and Pantzartzis, 1993, Edgecock, 1994. However, these theories must be validated by independent measurements such as seabed samples before bottom classification can be considered.

Another approach shown by Mitchell and Somers, 1989, de Moustier and Matsumoto 1992, converted sidescan intensity data directly into physical acoustic parameters such as backscatter coefficients. Unfortunately the side-scan sonars used by these authors, GLORIA (Geological Long Range Inclined Asdic) and SeaMARC II, were not calibrated, and the calibration of these systems is difficult, de Moustier *et al* 1990b.

A fully calibrated interferometric side-scan sonar has been developed, Geen, 1993, and it is hoped that the limitations reported by Mitchell and Somers, 1989, de Moustier and Matsumoto 1992, will be overcome.

Chapter 2

Backscatter of sound from the ocean bottom

2.1 Introduction

An incident acoustic wave striking the seabed can be reflected, absorbed and scattered. The relative magnitudes of these effects are dependent upon the seabed characteristics, its roughness, frequency of the incident acoustic wave and the angle of arrival of the acoustic wave.

The characteristics of reverberation from the seabed are interesting from two standpoints:

1) Studying the properties of reverberation as a source of sonar interference, that is, as a factor hindering detection of echo signals and the measurements of their parameters.
2) Studying reverberation as a phenomenon which can be used to investigate and predict the physical properties of the seafloor. It is this interaction of the acoustic wave with the seabed which is of primary interest

There have been two ideas proffered to account for the recorded backscatter values:

1) Sea-sediment interface roughness or inhomogeneities, which affects the reflected energy
2) Sediment volume inhomogeneities (velocity and density fluctuations) which affect the refracted energy.

Theoretical and experimental work has been carried out to determine which scattering mechanism is dominant for each seabed, and this will be detailed below.

2.2 Backscattering of sound

Inhomogeneity is a characteristic property of every real medium. Two types of inhomogeneities occur, regular and random. The backscatter of acoustic waves is due to random inhomogeneities. The backscattered waves are usually termed the diffuse or incoherent waves, because of their wide angular spread and the lack of phase relationship with the incident wave. Similarly, the specular wave, due to regular inhomogeneities, is often termed the coherent field, due to its predictable, and constant, phase relative to that of the incident wave.

The theoretical study of the wave propagation in an inhomogeneous medium can be represented by the wave equation with variable coefficients. Different theoretical methods have been put forward to try and predict the backscatter strength, the most popular are:

1) Lamberts rule.
2) Perturbation method.
3) Kirchoff theory.
4) Composite method.

A large proportion of these models have their origin in sea-surface reverberation models. A review of these sea-surface models can be found in Fortuin, 1970. The models which are of primary interest to side-scan sonar operators are those which deal with angular dependencies.

Several comprehensive reviews, such as Jackson D.R., 1986a and Stewart W.K., 1994, have been published which analyse acoustic data to determine the behaviour of bottom backscatter strengths as a function of grazing angles, effective horizontal beamwidths, transmit signal type, frequency and bottom type. The reviews generally agree that bottom backscattering can be broadly characterised according to bottom composition such as mud and silt, sand, and rock and gravel.

It has been determined that there are two basic mechanisms which lead to varying backscatter values, one is seabed inhomogeneities and the other is the roughness of the seabed. Boehme, 1988, stated that below 10kHz, the backscattering may be dominated by volume inhomogeneities, whilst at 300kHz and above, the backscattering may be dominated by interface inhomogeneities. In the mid-frequency range, however, the backscattering may be a mixture of both processes.

To determine if a surface appears rough for the frequency used, then the Rayleigh Criterion is used, see section 2.4 on determination of seabed roughness.

2.3 Seabed inhomogeneities.

As the sound enters the seabed volume it undergoes attenuation and volume scattering, a schematic representation of this can be seen in Figure 2.1.

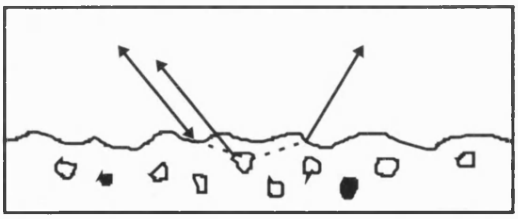

Figure 2.1: A schematic showing how a sound wave upon interaction with a rough seabed and its inhomogeneities, can result in forward and backscatter.

Urick, 1967, has shown that the backscatter cross section for volume scattering can be represented by σ_{bv}

$$\sigma_{bv} = \frac{10}{\ln 10}\left(\sigma_{vt} + \sigma_a\right) \qquad \textbf{(2.1)}$$

where σ_{vt} and σ_a are total cross sections per unit volume for scattering and absorption, respectively, by the sediment.

2.4 Determination of Seabed Roughness

In the determination of surface roughness, the Rayleigh Criterion is adopted from Optics.

Wavescattering from rough surfaces was first studied by Rayleigh 1877, who considered the problem of a plane monochromatic wave incident normally on a sinusoidal surface. This work led to the so-called Rayleigh Criterion for determining the degree of roughness of a surface, for which a simple physical interpretation is possible.

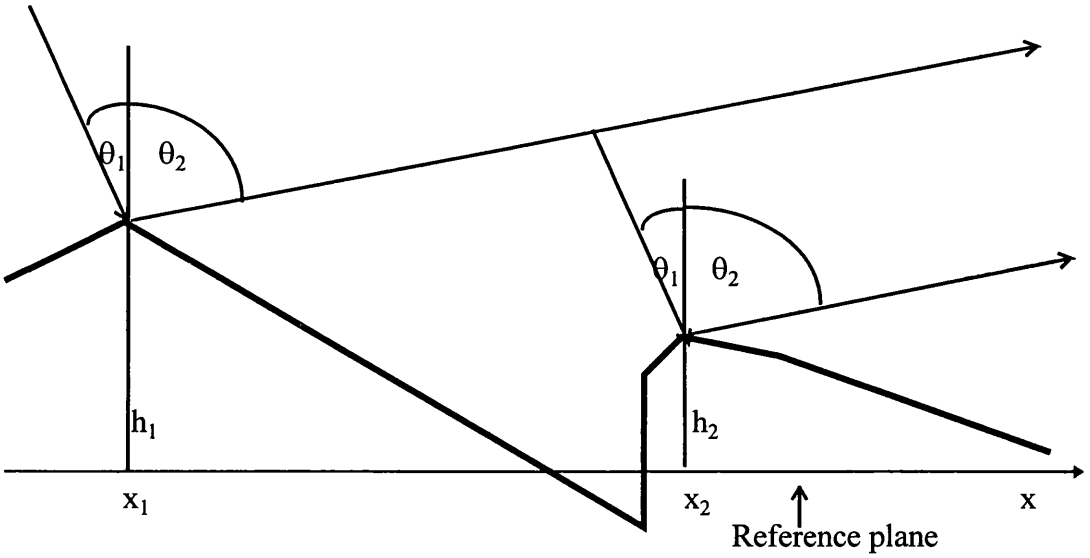

Figure 2.2: A schematic diagram showing the phase difference between two parallel rays scattered from different points on the surface.

Consider Figure 2.2, which shows a plane monochromatic wave incident at some angle θ_1, onto a rough surface. For waves scattered into the azimuthal plane, that is (x,z) plane, the phase difference $\Delta\phi$, for specular scattering, given by $\theta_1 = \theta_2$, is:

$$\text{Phase difference} = \Delta\phi = 2k\Delta h\cos\theta_1 \quad \text{where } \Delta h \text{ is } h_1 - h_2 \qquad \textbf{(2.2)}$$

Where k is the modulus of the incident (and scattered) wave vector and the scattering points are located at x_1 and x_2. The heights of the points are h_1 and h_2.

The interference between these rays depends on the magnitude of this phase difference compared with π.

For $\Delta\phi << \pi$, the two waves will be almost in phase and will constructively interfere. For $\Delta\phi = \pi$, the waves will destructively interfere leading to no contribution.
The Rayleigh Criterion states that if $\Delta\phi < \pi/2$, the surface is smooth, otherwise it is rough.
If this phase difference restriction is averaged across a surface then $\Delta h = \sigma$, where
σ = surface root mean square height deviation and the criterion becomes

$$Ra < \pi/4$$

Ra = Rayleigh parameter

$$Ra = k\sigma \cos \theta_1 \qquad \textbf{(2.3)}$$

Both the frequency and the angle of the incident wave determine how 'rough' any surface appears to be, that is its effective roughness.
If Ra is <<1 the roughness of the surface is small, and the surface scatters sound slightly - the main part of the sound energy propagates in the specular direction as a coherent wave.
If Ra >> 1 corresponding to a rough surface which causes considerable sound scattering in a relatively wide angular interval.

2.5 Seabed roughness

Figure 2.3 shows three cases of seabed roughness: the first being a flat seabed, the second being a semi-rough seafloor and the final picture shows a seabed with a roughness greater than the incident waves wavelength.

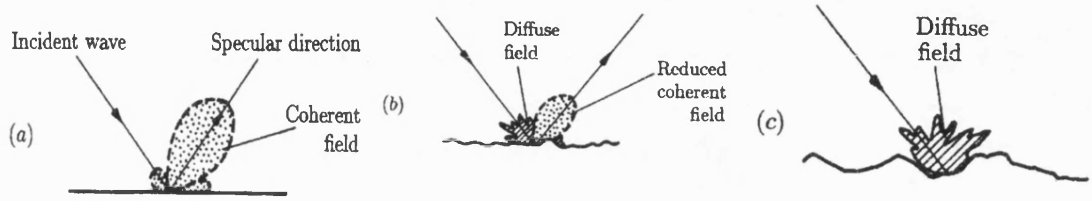

Figure 2.3: Three cases of seabed roughness, a) flat b) semi-rough and c) rough seabed to show the difference in specular energy. Ogilvy, 1991.

The main difference between the cases presented in Figure 2.3 is that the resultant specular energy is much greater for the flat seabed.

If the magnitude of the scattered energy depends upon the roughness of the seafloor, then there are two different types of models which can quantify the magnitude of the scattered energy.
One type of model can only calculate the monostatic reverberation, that is when the source and the receiver are at the same location and the other type of model can calculate the bistatic reverberation, that is when the source and receiver are at different locations.

The monostatic case is normally called backscatter and the backscattering cross section is the measure of the ability of a body to scatter sound back to a receiver that is at the same location as the transmitter.

The backscatter cross section is expressed in Equation 2.5.

σ_{bs} is the backscatter cross section per unit solid angle per unit area

$$\sigma_{bs} = \frac{I_s}{I_i}\frac{r^2}{A} \qquad \textbf{(2.4)}$$

Where I_s is the scattered intensity (W/m^2)
I_i is the incident intensity (W/m^2)
r is the range (m)
A is the area of scattering (m^2)

The term σ_{bs} is a dimensionless quantity and this is independent of the unit system employed. The scattering strength can be calculated by taking logs.

$$\text{Scattering strength} = S = 10 \log_{10} \sigma_{bs} \qquad \textbf{(2.5)}$$

This has the units of dB.

2.6 Lamberts Law

Lamberts law for calculating the backscatter strength is an empirical method. It depends upon the grazing angle and has no dependence upon the frequency used.

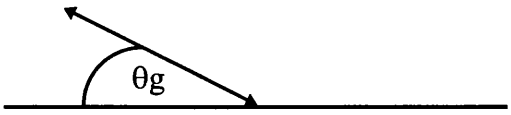

Figure 2.4: Schematic to show grazing angle for a monostatic case

Lamberts law assumes that the sound is scattered proportionally to the sine of the grazing angle, a schematic of which can be seen in Figure 2.4, and is given by equation 2.7

$$\text{Lamberts law} = Sb = \text{Backscatter Intensity} = 10 \log \mu + 10 \log \sin^2 \theta g \qquad \textbf{(2.6)}$$

The term 10 log μ is defined as the mean normalised backscatter strength, or the scattering strength. A figure for this was given by MacKenzie as -28 dB.

Although Lamberts law shows good approximation when the seabed roughness is large compared to the wavelength of the incident sound wave, the backscatter will be independent of frequency and Lamberts law will apply.

However, when the roughness of the seafloor is small compared to the wavelength, that is the Rayleight scattering parameter is much smaller than one, the scattering strength will increase with frequency and this his effect cannot be accounted for by Lamberts law. A more physically correct model is required.

2.7 Slightly rough surfaces: 'Perturbation' theories

This theory is used for seabed surfaces which have the root mean square surface height roughness small compared to the acoustic wavelength.

The scattering of waves on a seabed which is only slightly rough may be studied using the perturbation theory. For a smooth surface we choose a model which is a solution for a flat seabed, together with a 'perturbative' term arising from the slight surface roughness.

The theory does not, however, take into account multiple scattering, or other effects, such as shadowing which combine to reduce the accuracy of the perturbation approach. These effects will become more marked as the angles of incidence and scattering increase away from the mean surface normal. This leads to restrictions on both the surface root mean square height, relative to the incident wavelength and the absolute surface root mean square gradient.

2.8 Kirchoff theory

Kirchoff theory is the most widely used theory in the study of wave scattering from rough surfaces. This is perhaps due to two reasons: the theory has an easily understandable physical basis and, in some important limits, leads to relatively simple analytical expressions for scattered wave amplitudes, these being readily compared with experiments.

Kirchoff theory provides an approximation to the wave field on the surface of the scatterer by the application of Huygens principle, which states that every point on the wavefront can be considered to be a source of secondary waves. Each point on the scatterer is treated as though it is part of an infinite plane, parallel to the local surface tangent.

The scattered field is then calculated from the integral over all the elementary sources, from Huygens principle, using the Helmholtz integral and the tangent plane

approximation. The resulting Helmholtz-Kirchoff integral relates the field on the scattering surface to the field at any point. The Helmholtz-Kirchoff integral was modified and simplified by Thorne and Pace, 1983, Pace, 1990 to take into account the Fresnel phase effects on the scattered intensity.

Due to the tangent plane approximation the Kirchoff theory is exact for surfaces that are infinite, smooth and planar. For all other scatterers the theory is an approximation and suffers from two shortcomings: the theory is not self-consistent and does not conserve energy, Ogilvy, 1991.

The first limitation means that if Kirchoff Theory is used to calculate the field away from a scatterer and this field is then specialised to points on the scatterer then the surface fields do not satisfy Kirchoff Theory. This problem arises from the attempt by Kirchoff Theory to specify all the boundary conditions on the surface of the scatterer, Baker and Copson, 1950.

The lack of energy conservation suggests that propagating modes, such as surface waves are ignored by Kirchoff Theory. In the context of rough scattering this lack of energy conservation also arises through neglect of multiple scattering events.

Due to the limitations that a rough surface has, the theory is sometimes referred to as the 'High-frequency approximation', because every part of the scattering surface must be locally planar. This means that the surface must not deviate from planar over some distance $n\lambda$, where n is some small number, and λ is the wavelength of the frequency being used, then the smaller the wavelength, the smaller the distance over which the surface is restricted to being quasi-planar. In this sense therefore the theory is 'High-frequency'

This limitation gave rise to a variation of the Kirchoff theory by the insertion of a correction term, Bass & Fuks, 1979, to give the restriction on the applicability of Kirchoff to:

$$kr_c \cos\theta_1 >> 1 \qquad (2.7)$$

where k is the incident wavevector modulus,

r_c is the radius of curvature of the surface at the point A,

θ_1 is the 'global' angle of incidence measured from the mean plane normal.

For details of this correction term see Appendix 2.1.

2.9 Composite Model - Perturbation-Kirchoff model

The two previous methods on wave scattering from rough surfaces assume that any surface can be considered on a single scale. In practice all surfaces are rough on many scales, ranging from the atomic scale to a scale determined by the length of the surface, for a schematic representation of this see Figure 2.5.

This effect manifests itself in surface properties that are dependent on the length of the sample used for measurement, and the resolution of the measuring technique. A model is therefore required that describes scattering from roughness features over a finite wavelength spectrum. As yet, no such model exists but models have been developed for describing surfaces that consist of small amplitude fluctuations superimposed on a slowly varying roughness.

The surface is modelled as two independent components, a small amplitude, high-frequency roughness superimposed on a low-frequency variation of larger amplitude.

Figure 2.5: Seabed surface which consists of small amplitude fluctuations superimposed on a slowly varying roughness.

The perturbation theory is used to describe scattering from the high frequency roughness and the Kirchoff theory is used for the low frequency component, Barick & Peake, 1968, Backmann, 1973, Galybin, 1976, Brown, 1978, McDaniel & Gorman, 1982, 1983.

One of the first composite roughness models was developed by Kuryanov, 1963. This model calculated the field from the small scale high frequency roughness using perturbation techniques, and the field scattered from the low frequency, large roughness, calculated using the Kirchoff approximations. Later techniques rely on the separation of the surface roughness spectrum into the low frequency and high frequency domains.

The problems with these techniques is in determining a suitable frequency at which to separate the two roughness scales. At frequencies above the splitting frequency the Perturbation approximation is valid and at frequencies below the splitting frequency the Kirchoff approximation is valid, hence an incorrect choice of the splitting frequency may result in the application of a scattering model outside its domain of validity.

Since the early work on composite models was carried out the model has been steadily improved. In 1973, Bachmann applied a technique for the cut-off frequency between the two models, McDaniel and Gorman, 1982, included terms for the shadowing of the surface and the tilt of the large scale surface, a term for volume scattering was added in 1983 by McDaniel and Gorman. Jackson et al, 1986 extended the model for seafloor backscatter at a two fluid boundary. These models were then compared to data which has increased the confidence in the composite model.

In 1994, Jackson improved the model by adding the spectral level and an exponent of the power law to the model which already contained information on the sediment characteristics. The model still treats scattering as a function of both seabed and volume inhomogeneities, though acoustic penetration of the seabed at high frequency is slight, the sediment volume scattering can be described as a surface process and quantified by an effective interface scattering cross-section.

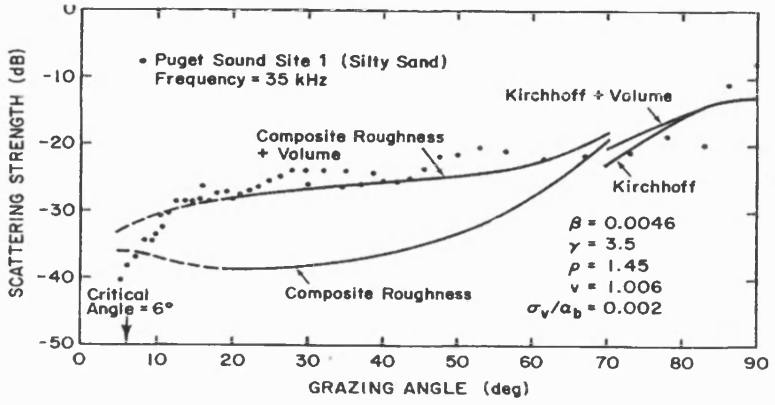

Figure 2.6: Graph of backscatter strength versus grazing angle. Jackson 1986

2.10 Experimental

A Seabed is characterised by the presence of all types of sediments ranging from fine clays and mudstones to coarse-grained sands, pebbles, shell materials and rocks and they can be grouped according to mean grain size using the Wentworth classification, see Table 2.1.

Sediment type	Mean grain size, D, mm	Mean grain size, $\phi = -\log_2 D$	Wentworth size class
Rock	>4096 1024 256	<-12 -10 -8	Boulder
Stones	64	-6	Cobble
Gravel	16 4		Pebble
	3.36 2.83 2.38 2	-1.75 -1.5 -1.25 -1	Granule
Sand	1.68 1.41 1.19 1	-0.75 -0.5 -0.25 0	Very coarse sand
	0.84 0.71 0.59 0.5	0.25 0.5 0.75 1	Coarse sand
	0.42 0.35 0.3 0.25	1.25 1.5 1.75 2	Medium sand
	0.21 0.177 0.149 0.125	2.25 2.5 2.75 3	Fine sand
	0.105 0.088 0.074 0.0625	3.25 3.5 3.75 4	Very fine sand
Silt	0.053 0.044 0.037 0.031	4.25 4.5 4.75 5	Coarse silt
	0.0156	6	Medium silt
	0.0078	7	Fine silt
	0.0039	8	Very fine silt
Clay	0.002 0.00098 0.00049 0.00024 0.00012 0.00006	9 10 11 12 13 14	Clay

Table 2.1: Wentworth size classification of sediment types

For shallow water these differences in seabed type are attributable to the greater mobility of the water medium in a shelf region (underwater and tidal currents), the penetration of dynamic surface processes to the bottom and the abundant influx of sedimentary material from the land masses, that is coastal erosion or solid discharge of rivers.

Early experiments were designed to record the backscatter coefficient versus grazing angle for different types of seabed's and note any differences in the backscatter strengths. Early papers published found a clear dependence of seabed type to backscatter strength, later papers then investigated the actual scattering method with no one scattering theory dominant with recent papers using frequency bands to explain the discrepancies between published results and theories.

One of the first experiments designed to investigate the backscatter dependence on grain size, surface roughness, frequency was done by Nolle, 1963. He measured the backscatter properties of sand in laboratory conditions. The sand was cleaned, graded, compacted, degassed and water saturated, the water sediment interface was scraped flat.

The shapes of the backscatter curves were as predicted by the theory, apart from when grazing angle of incidence became less than the critical angle. This was put down to decreased acoustical penetration of the sand medium when the angle of incidence is less than critical.

McKinney and Anderson, 1964, produced a paper whose primary interest was the dependence of backscattered reverberation on grazing angles, frequency and bottom type (particle size and relief).

McKinney and Anderson posed the question that, assuming that at fairly high frequencies that there would be relatively little penetration of sound into the ocean bottom composed of sand and gravel and more penetration into mud bottoms, then one would expect the magnitude and nature of the scattering to be a function of both the particle size of the bottom and the surface (bottom) relief.

McKinneys results showed a 25dB difference in backscatter values from seabed's ranging from Mud to Gravel, see Figure 2.7.

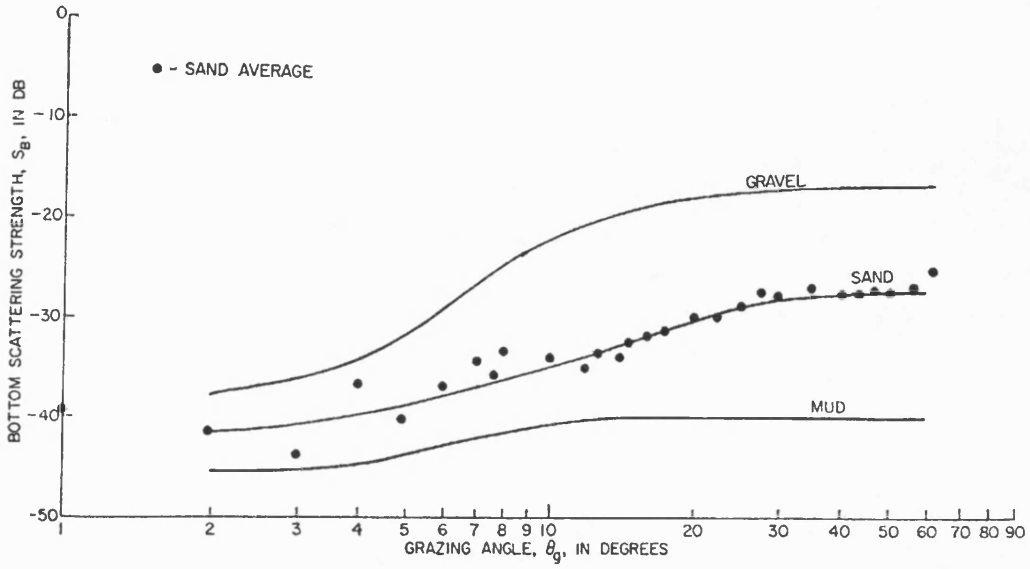

Figure 2.7: Average curves for different seabed types consisting of backscatter strength as a function of grazing angle. McKinney 1964.

The backscatter strength versus grazing angles shows the data for sands tend to group together and are different from gravel, rock and mud data, from this he deduced that at a single frequency the bottom relief is a major factor in the backscattering of sound, but also the particulate nature of the sediment is also a significant factor in the scattering process.

Wong and Chesterman, 1968, found that for every set of experimental readings there was a spread of values of the backscatter strength. A major part of this spread was accountable for by the bottom topography, but also the data shows a clear dependence of the backscatter strength on bottom type. As the textural grade changes from clay to silt, to sand to rock, the backscatter strength increases by nearly 25dB, see Figures 2.8 to 2.11.

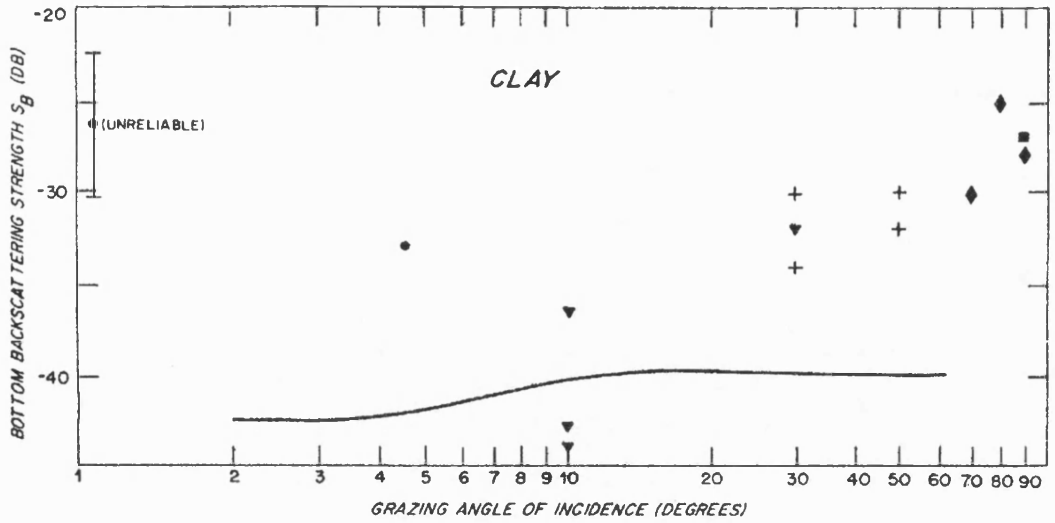

Figure 2.8: Backscatter strength versus grazing angle for a clay seabed. Wong and Chesterman 1968.

▼ UCDWR, 1946, ◆ Urick, 1956, ■ Mackenzie, 1961, + Urick and Saling, 1962, — McKinney and Anderson, 1964, ● Wong and Chesterman,1968

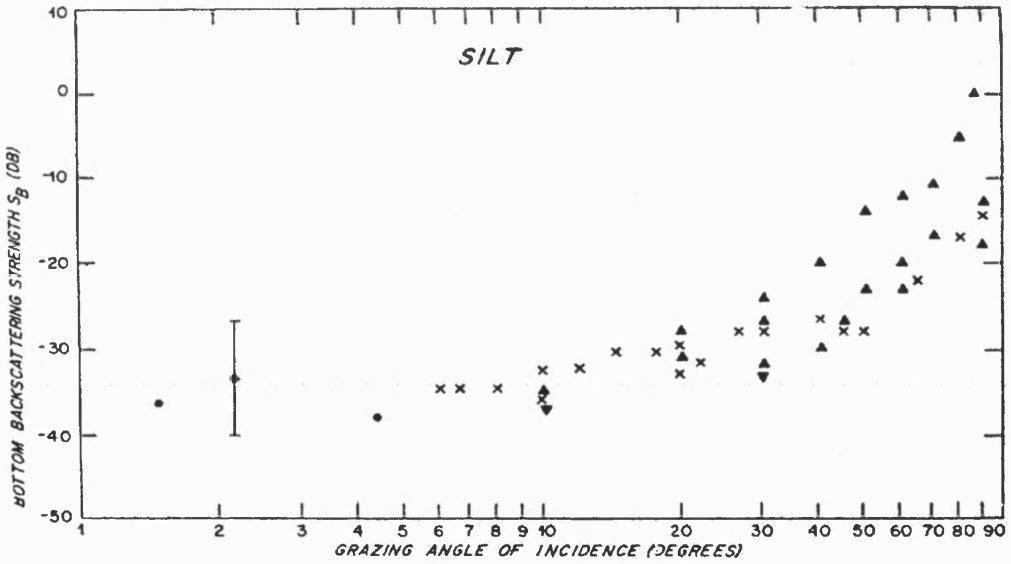

Figure 2.9: Backscatter strength versus grazing angle for a Silt seabed. Wong and Chesterman,1968.

▼ UCDWR, 1945, ▲ Urick, 1954, ■ Mackenzie, 1961, X McKinney and Anderson, 1964, ● Wong and Chesterman, 1968

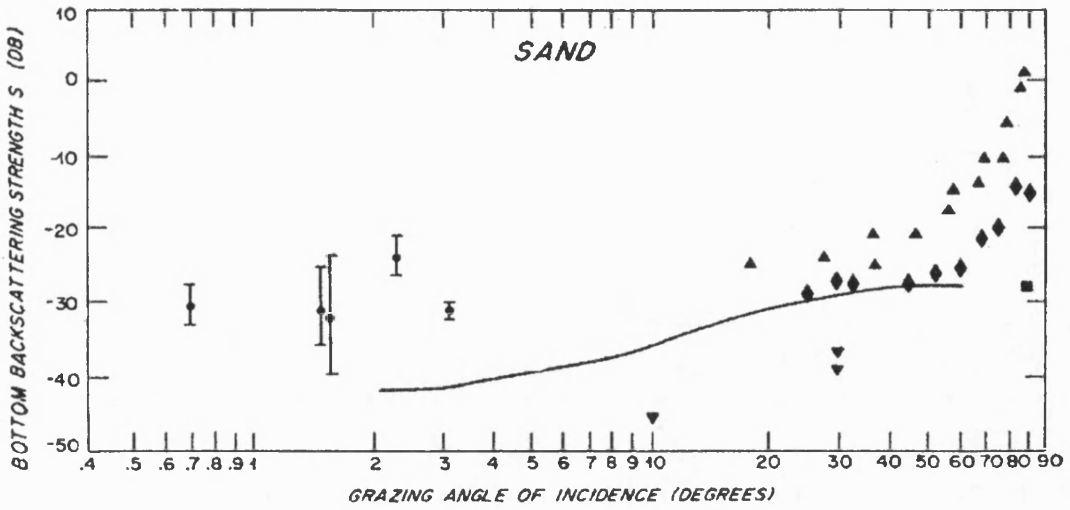

Figure 2.10: Backscatter strength versus grazing angle for a Sand seabed. Wong and Chesterman, 1968.

▼ UCDWR, 1945, ▲ Urick, 1954, ◆ Urick, 1956, ■ Mackenzie, 1961,
— McKinney and Anderson, 1964, ● Wong and Chesterman, 1968

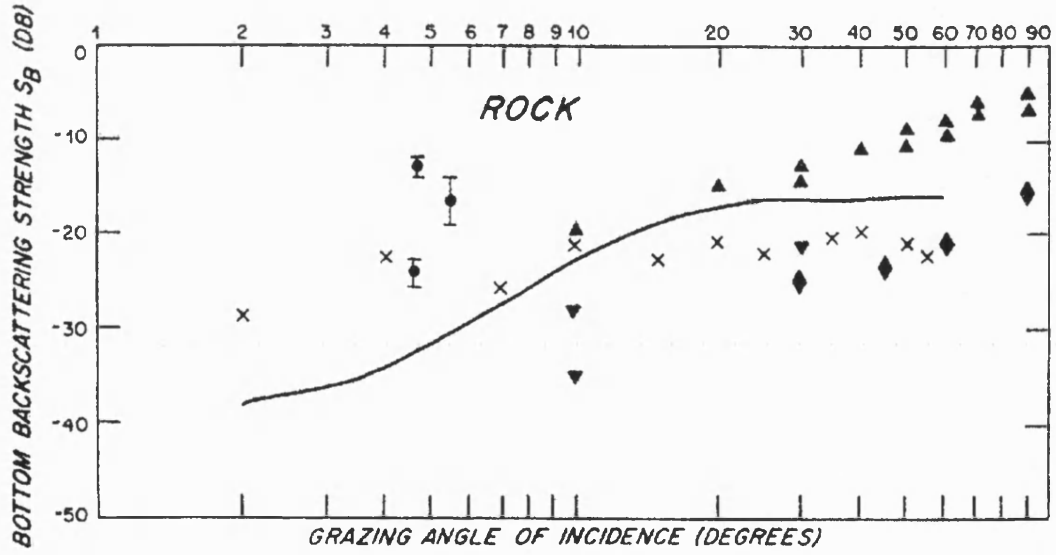

Figure 2.11: Backscatter strength versus grazing angle for a Rock seabed. Wong and Chesterman, 1968.

▼ UCDWR, 1945, ▲ Urick, 1954, ◆ Urick, 1956, ● Wong and Chesterman, 1968,
— McKinney and Anderson, 1964 (Averaged Gravel data),

x McKinney and Anderson, 1964 (Averaged Rock data)

This indicates that the particulate nature of the seabed is at least partly responsible for the backscattering, with the penetration of sound into the sub-bottom higher for clay and silt. However, the erratic distribution of the backscatter coefficients amongst bottoms of the same type suggests that bottom roughness also plays an important role in the scattering mechanism. Again this raises the question, which of the two factors is more dominant, bottom roughness or particulate nature.

Smailes, 1978, discovered that a rougher seabed exhibited lower backscatter values and also the backscatter values depended little on the actual grazing angle. He explained this by saying that it might first be assumed that rougher seabed surfaces should scatter more energy, closer inspection reveals the fact that there will be more facets presenting grazing angles greater than the critical Rayleigh angle, and hence multiple absorption will also increase, so more energy is absorbed into the seabed in rougher areas

In 1980, Bunchuk put forward the theory that it was the volume inhomogeneities which dominated the resultant backscatter strength. His experimental data was compared with the theory of scattering by random roughness of a water-sediment interface and with the theory of scattering by a layer containing inhomogeneities caused by fluctuations of the refractive index and density of the sediments. The observed experimental characteristics could not be explained theoretically by the scattering of sound from a rough surface, but it was explained satisfactorily by the theory of scattering by volume inhomogeneities of the sedimentary medium.

Boehme and Chotiros, 1985, reported that the backscatter results that they observed were attributable to bottom roughness and the scatter in the data points, as reported by Wong and Chesterman, 1968, were due to lack of information on propagation loss. They analysed the acoustic data to determine the behaviour of backscatter strength as a function of grazing angle, horizontal beam width, transit signal type, frequency and bottom type. He found the backscatter curves followed Lamberts Law and different types of seabed could be distinguished.

Jackson et al, 1986, wanted to develop a high-frequency model of the seabed, but he needed to know which parameters, that is grain size, porosity, roughness, were required to determine the high-frequency scattering properties.

He reviewed the previous publications and before he could develop an acoustic remote sensing technique, he concluded that a better understanding of the physical process of scattering would be essential. Previous datasets had shown a strong falloff in backscatter strengths at small grazing angles and other datasets showed little dependence on grazing angles, but due to the fact that these datasets were unaccompanied by detailed physical measurements no definite conclusions could be drawn.

His experimental data showed that, except at sites with extremely rough bottoms, the scattering strengths were observed to decrease rapidly as the grazing angle decreased to 5-10 degrees. At these grazing angles, which were shallower than the 'critical angle', penetration into the bottom was negligible and volume scattering should be un-important.

The variability of results was greater over a track covering a uniformly fine-grained sand bottom than over a track where the bottom material changed from coarse to fine sand, he deduced from this that grain size is not sufficient determinant of scattering strength for fine sediments.

Stanic, 1988, again re-iterated that the basic scattering mechanisms were still not completely understood, this understanding is essential for the development of an improved understanding of high-frequency reverberation. Stanic found little correlation between scattering strength and particle or grain size, he also found a lack of scattering strength dependence on root mean square bottom roughness even at low grazing angles.

Boehme, 1988, reached an important conclusion in his paper. He re-stated that the backscatter is generally considered to be composed of two principal components, backscatter at the water-sediment interface due to surface roughness and secondly scattering from inhomogeneities within the sediment volume.

Backscatter at the water-sediment interface, particularly for sandy bottoms is caused by surface roughness which is due to particle size, sand ripples and dunes that are mainly hydrodynamic in origin.

Inhomogeneities within the sediment include the effects of buried rocks or shells, marine organisms or their burrows. The main aim of bottom backscatter measurements has been to accurately relate bottom reverberation levels and variability to a small number of readily measurable bottom characteristics.

Boehme states that the frequency dependence of acoustic bottom backscattering is fundamental to an understanding of the scattering process. He states that at frequencies below about 10kHz, the attenuation coefficient in the bottom is low enough that there is significant penetration and the backscattering may be dominated by backscattering from inhomogeneities within the sediment. At very high frequencies, above about 300 kHz, penetration to any significant depth is negligible and backscattering is caused by interface inhomogeneities. In the frequency range in-between, the backscattering may be a mixture of both processes.

He also found for shallow grazing angles, less than 10 degrees, the observed relationship between bottom backscattering strength and grazing angle was found to be consistent with Lamberts rule, but no strong relationship could be found between bottom backscattering and bottom roughness or volume microstructure.

Stanic, 1989, carried out a series of high-frequency acoustic bottom backscatter measurements on an area of seabed which was chosen because the bottom roughness was characterised solely by a high-impedance surficial layer of coarse shell. The backscatter strength versus grazing angle for the seabed whose bottom was covered with a dense shell layer was on average 8-10 dB higher than those measured at a smooth homogeneous seabed location, the results showed no significant dependence on root mean square bottom roughness. At low grazing angles it was thought that the scattering strengths should be sensitive to changes in bottom roughness.

Variability of grain size at the sediment surface, where bands of coarser shell hash alternate with areas of sparser less coarse shell hash, does not appear to produce any variability in the measured acoustic backscatter strength.

More recently, Stewart, 1994, stated that you need three parameters for complete characterisation of the seabed. You need sensor geometry, seafloor topography and physical properties of the seafloor.

2.11 Summary

With the modern interferometric side-scan sonar we can calculate the seafloor topography and the sensor geometry is automatically recorded. All the reports state that there is a difference in the backscatter strengths for different types of seabed. For different bands of frequencies, different scattering mechanisms are valid. Although all experimental datasets showed different backscatter values for different seabed types, no single value could be assigned to one type of seabed.

Appendix 2.1 Correction term for Kirchoff theory

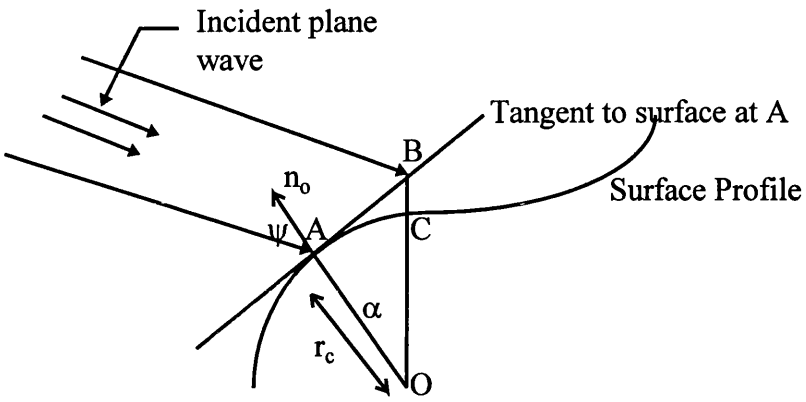

Figure A2.1: Schematic to determine the accuracy of the Kirchoff Theory

In Figure A2.1, the point A is an arbitrary point on a rough surface. The point O is the centre of the curvature of the surface at A and the point B is some distance from A, on the tangent plane to A. The deviation of the rough surface from this plane is measured by the distance BC, where C is the intersection of the radial line from O to B with the rough surface. Intuitively the distance BC must be 'small' and the distance AB 'large', for Kirchoff Theory to be appropriate, where these distances are related to the incident wavelength. A reasonable requirement is for the distance BC to be small compared with the projection of the incident wavelength onto the surface normal n_0 and for the projection of AB onto the plane normal to the incident wavevector direction to be large compared with the incident wavelength. This leads to the two inequalities

$$kAB \cos\psi >> 1 \quad \text{where k is the incident wavevector modulus} \quad \textbf{(A2.1)}$$

$$kBC \sec\psi << 1 \quad \textbf{(A2.2)}$$

Assuming the angle α, the angle subtended by AB at O, to be small in the sense that $BC \sim AB\alpha \sim (AB)^2/r_c$ where r_c is the radius of curvature of the surface at the point A, then the second inequality of the above equations becomes

$$\frac{k(AB)^2 \sec\psi}{r_c} \langle\langle 1 \qquad \textbf{(A2.3)}$$

and substituting for AB from the first equation, gives

$$kr_c\cos^3\psi >> 1 \qquad \textbf{(A2.4)}$$

For surfaces of small slope we have that $\psi \approx \theta_1$ where θ_1 is the 'global' angle of incidence, measured from the mean plane normal, the above equation becomes

$$kr_c\cos^3\theta_1 >> 1 \qquad \textbf{(A2.5)}$$

This being the most often quoted restriction on the applicability of Kirchoff theory. The radius of curvature of the surface is restricted, relative to the wavelength of the incident wave, the severity of the restriction being dependent on the angle of incidence.
An alternative inequality sometimes quoted as determining the range of validity of Kirchoff theory is

$$kr_c\cos\theta_1 >> 1 \qquad \textbf{(A2.6)}$$

This is equivalent to restricting AB, rather than its projection onto the normal to the incident wavevector, to being very much larger than the incident wavelength.

Chapter 3

Sidescan Sonar

3.1 Introduction

This chapter will discuss the basic principles of the sidescan sonar and some of the terms used. It will then go into detail as to what an Interferometric sidescan sonar is and its importance.

3.2 Basic introduction to the operation and principles of Sidescan

The sidescan sonar transmits a time limited pulse of acoustic energy into the water medium. A volume of water and the sea surface or sea bottom maybe insonified. The signal is partially scattered by various irregularities in the water medium and by any changes in acoustic impedance. It is then received, displayed and analysed; Figure 3.1 shows a diagrammatic representation of this.

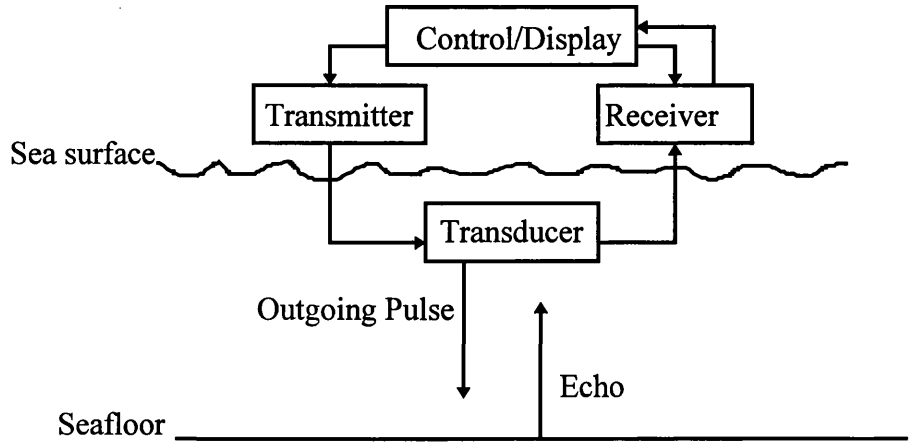

Figure 3.1: A schematic diagram showing the basic elements in any active sonar.

The process for producing the outgoing pulse of acoustic energy is to generate an oscillating electric field of the required frequency, duration and energy. This electrical pulse is then applied across the transducer which in most sonar systems consists of a piezoelectric material. This material expands or contracts when an oscillating voltage is applied across it, producing an oscillating pressure wave, or the acoustic pulse which is transmitted into the water medium.

The acoustic pulse then propagates through the water column until it encounters something such as the seabed, sea surface or an object, some of that signal is scattered back towards the source of the acoustic signal.

In most circumstances the same aperture which transmitted the pulse is used to receive the scattered signal, and the acoustic pressure is converted back to a voltage using the piezoelectric properties of the transducer. The system electronics then amplify, display and store the signals for post-processing. In addition to the sonar signals, deployment sensors may also record the environmental data of the sidescan sonar, such as roll, pitch, heave and the navigation information.

The ability to process the data off-line means that only the minimum amount of on-line processing is required and the post-processing can include all forms of data correction and processing. Figures 3.2 and 3.3 below give an indication of the hardware and software used in a modern sidescan sonar.

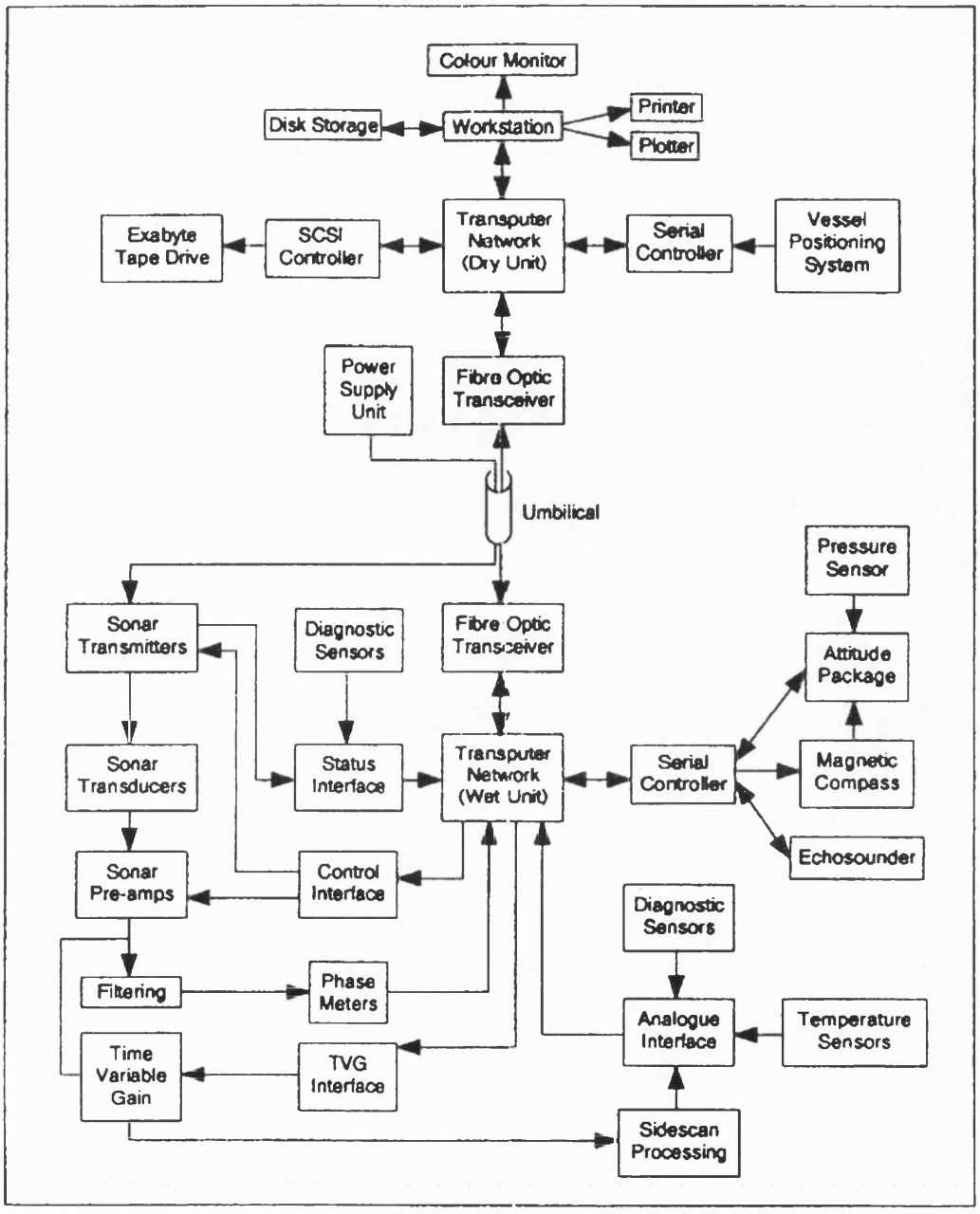

Figure 3.2: Block diagram of the sonar electronics and computer hardware used in a modern sidescan sonar

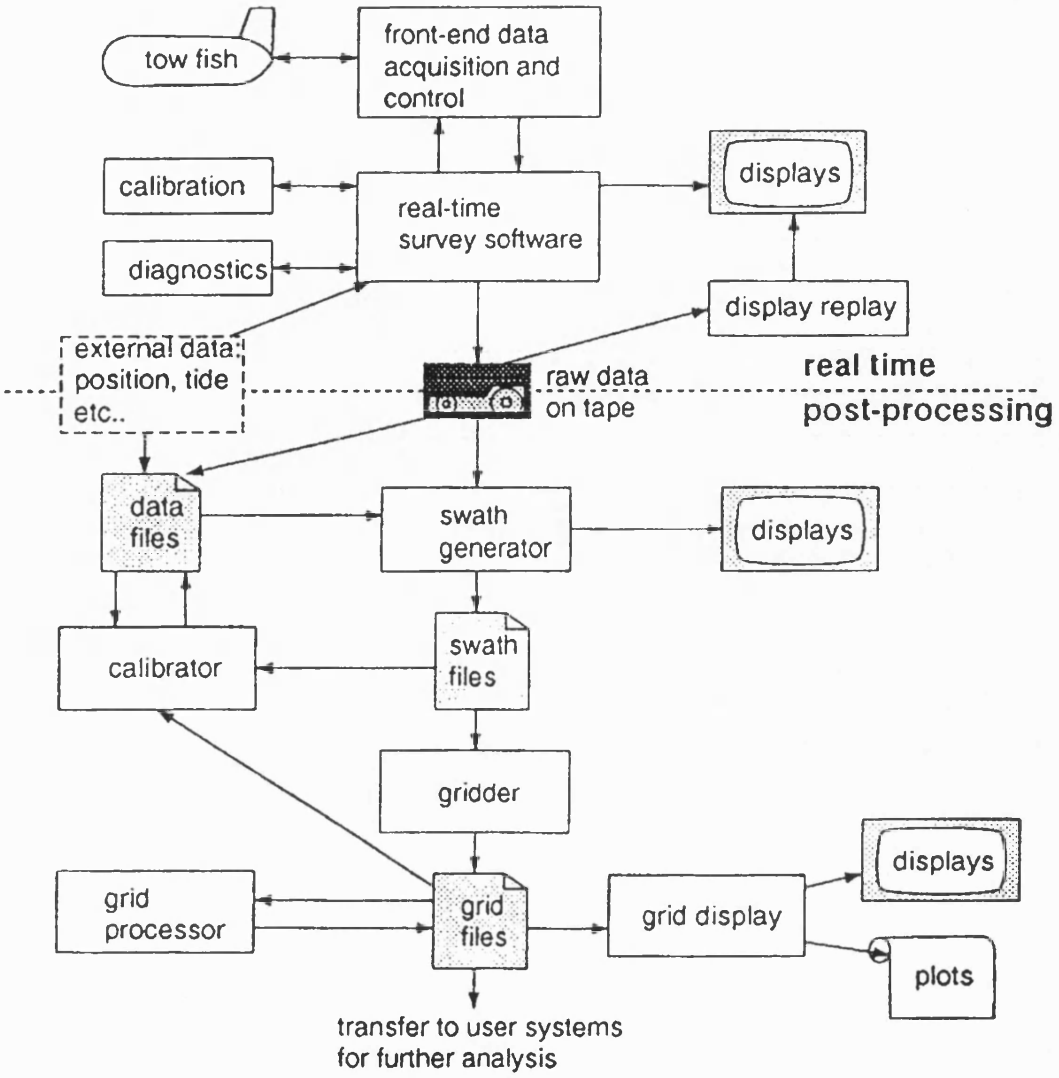

Figure 3.3: Block diagram of the real time and post-processing software required in a modern sidescan sonar

3.3 Sidescan Sonar

The important point in the name sidescan is that this means that the transducers are perpendicular to the direction of travel of the sidescan sonar system and a pulse is sent out which scans the seafloor.

The sidescan sonar is normally towed behind a vessel and is connected by a cable which supplies the power and communication lines.
The transducers are normally mounted on both sides of the sonar system, the data is recorded on two separate channels, this ensures that the maximum amount of seabed is covered at any one time. The transducers normally consist of many individual transducer elements distributed in such a way as to occupy as much of the active face of the array as possible. These transducers are used to radiate and receive in phase. Usually the same transducers are used to transmit and receive. A number of transducer elements are used as this makes the array more sensitive so they can either produce more voltage or current depending upon if they are connected in series or parallel. They would also posses better directional and signal-to-noise properties.

The transducers are normally shaped so that they produce a beam which is very narrow in the horizontal and large in the vertical. A large vertical beam means that as much of the seabed is covered away from the fish as possible and narrow in the horizontal to achieve high resolution along the area insonified.

The scanning process occurs in two directions. A pulse in the form of a fan-beam is sent out perpendicular to the sidescan sonar with the main beam axis at a set angle down from the horizontal, and at the same time the sidescan sonar has moved along its track and the next pulse would insonify a different area of seabed.

Figure 3.4 is a schematic of a pulse being emitted from the sidescan sonar. The pulse travels out from the sidescan sonar and insonifies a narrow area of the seabed, which is normally called a swath. The area of seabed which is contributing to the return signal, as shown in Figure 3.4 can be seen in more detail in Figure 3.5.

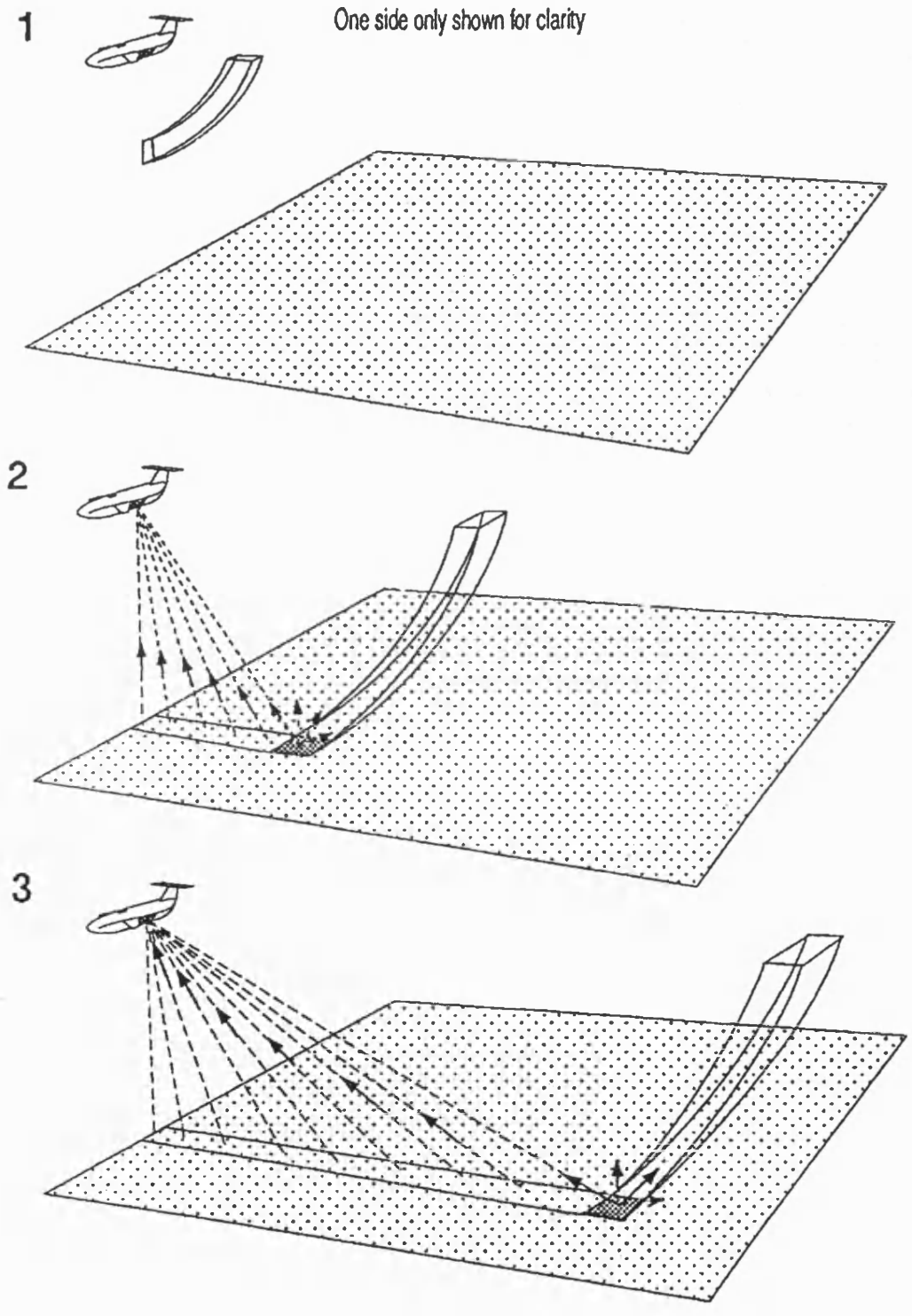

Figure 3.4: The sidescan sonar is seen emitting a ping. The ping insonifies a narrow strip of the seabed called a swath.

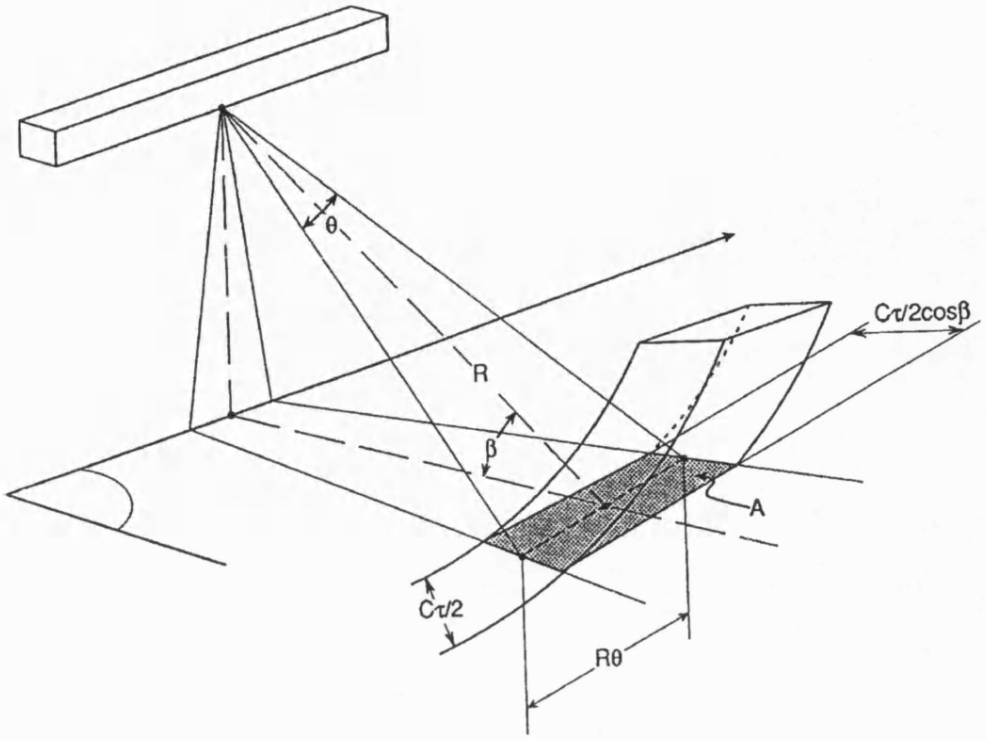

Figure 3.5: Geometry of the sound wave upon interaction with the sea-bed. de Moustier, 1993.

3.4 Sonar equations

3.4.1 Introduction

In the previous section the essential features and principles of the sidescan sonar were presented and now the equations which link the sidescan sonar to the effects the medium has on the acoustic pulse will be discussed. A basic understanding of these principles need to be developed before any acoustic model can be generated.

The sonar equations are a basic equality between the desired and undesired portions of the received signal at some point in the sonar equipment.

The sonar system receives acoustic energy from the seabed or an object and of this total acoustic energy some will be the signal from the seabed and some will be background noise and it is this understanding of the unwanted background noise which determines the success of the sidescan sonar

3.4.2 Sonar equation

The sonar parameters can be split into three sections:

1) Parameters determined by the Equipment
2) Parameters determined by the Seabed.
3) Parameters determined by the Medium

3.4.2.1 Parameters determined by the sonar system

a) Detection Threshold

This is perhaps the most obvious parameter as it is a measure of the intensity of the wanted signal to that of the unwanted signal. The signal-to-noise needs to be as large as possible.

b) Transmitted source level (SL)

This is defined as the intensity (in dB) of the transmitted pulse 1 metre from the transducer and it is measured along the acoustic axis, it is quoted with respect to a far-field intensity (or pressure) value reduced to 1m.

c) Directivity index (DI)

This term represents the directional properties of the transducer. It determines the amount by which the transducer array, through its beam pattern can improve the signal-to-noise ratio. Array directivity is highly desirable characteristic as it reduces the noise arriving at the array from directions other than that of the signal.

3.4.2.2 Parameters determined by the seabed

a) Backscattering cross section for a unit area of seabed (TS)

This is the measure of the backscatter properties of the seabed, it is usually called Target Strength but it can be replaced by the parameter Backscattering cross section, as discussed in Section 2.5. It is defined as the ratio of the backscattered intensity scattered by a unit area measured at 1m to the incident intensity at the seabed and is expressed in dB.

3.4.2.3 Parameters determined by the environments

a) Transmission loss (TL)

This represents the combined effects of spreading, absorption and scattering. Propagation loss depends on a number of factors of which the more important ones are sonar frequency, depth, temperature and sea state.

b) Background noise (BN)

The background noise level will in general be a combination of self and ambient noise and represents the intensity of the noise in the water around the transducer array. The

background noise is often assumed to be isotropic and is expressed in the same units as the source level.

c) Reverberation level (RL)

This is the intensity of the backscattered sound due to the transmitted pulse. Backscattering will occur from the volume of the sea due to sea surface, sea bed and suspended particles

All the above definitions can be best illustrated by the simple diagram shown in Figure 3.6

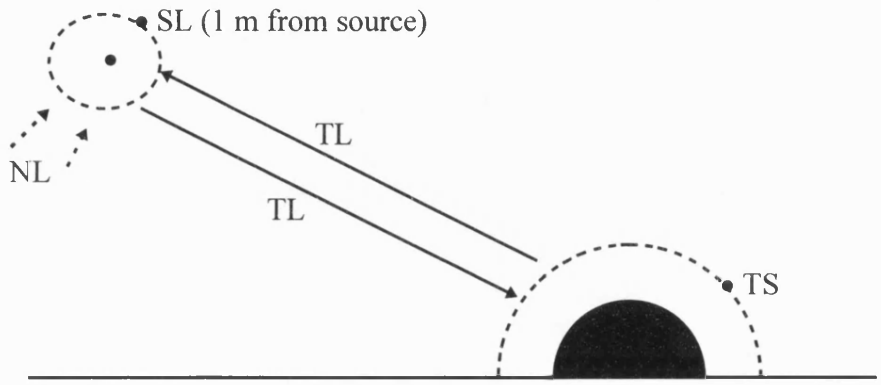

Figure 3.6: Schematic to illustrate sonar equation parameters

To calculate how much backscattered energy is received, going from the source to a target on the seabed and back to the receiver, the sonar equation would be generated in the following manner.

From the source to the target the result is SL-TL, on reflection or scattering the result would be as follows

$$SL - TL - TL + TS = SL - 2TL + TS \qquad \textbf{(3.1)}$$

This relationship can be used to relate the backscatter amplitude values to the acoustic properties of the seafloor and the medium the acoustic wave travelled through, the use of equation 3.1 will be discussed in Chapter 5.

3.5 Interferometric Seabed Inspection Sonar (ISIS)

3.5.1 Introduction

The standard technique of surveying the seabed for charting is to use a ship-mounted echo-sounder. This only measures the depth directly beneath the ship, and any area coverage must be achieved by running a series of closely spaced sounding lines that are approximately parallel to one another.

This method is not very effective and multibeam systems were developed. These are effectively a large set of echo sounders mounted perpendicular to the direction of travel, each inclined to a different angle to the vertical.

An Interferometric side-scan sonar has been developed as an alternative which gives accurate depth measurements whilst providing a large contiguous seabed coverage. This method measures the declination angle of a ray from the seabed by the simple procedure, in principle, of measuring the phase difference of the signals of two closely spaced receivers, one above the other.

3.5.2 Background

The first system which used two receivers for measuring depth was inspired by the interference patterns sometimes observed in conventional sidescan records and known as the Lloyd mirror effect. The effect was more noticeable when the sea surface was flat and it was caused by the interference between the direct path signal and a return signal reflected off the sea surface. It was realised by Chesterman, 1965, and by Heaton and Haslett 1971, that each fringe corresponded to a particular and predictable declination angle and could therefore provide useful depth information.

However the drawback of these early systems was the reliance of the system on a flat, or smooth, sea surface.

In 1974, Stubbs, developed the Telesounder which was not reliant upon a smooth sea surface. This independence was achieved by placing an acoustic reflector above the transducer. This provided a much more reliable and controllable source of interference fringes than that obtained using reflections from the sea surface. The use of a protruding plate was inconvenient and the next stage of the development was to obtain the same interference fringes using two transducers. These were spaced one above the other and their outputs added. The first description in the literature of such a system was by Denbigh, 1977.

3.5.3 Basic theory of Interferometric side-scan sonar

The Interferometric process involves a transducer consisting of a transmit stave and at least two receive staves, positioned above the seabed. The transmit and receive beams are narrow in the azimuth, and wide in elevation. the following analysis is therefore an essentially two-dimensional. The argument also assumes (initially) that the pulse is of a short duration, so that at any one instant a single point on the seabed is insonified by the pulse.

Figure 3.7 shows the location of the transducers relative to the seabed.

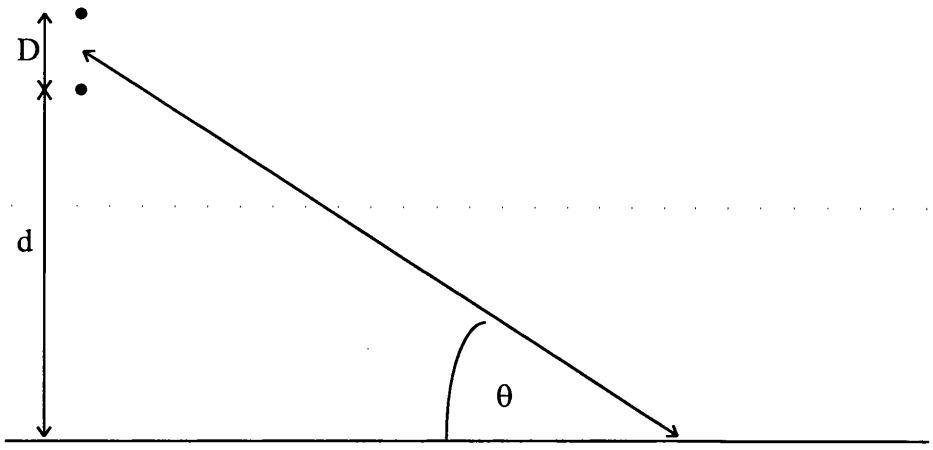

Figure 3.7: Arrangement of transducers relative to a flat seabed

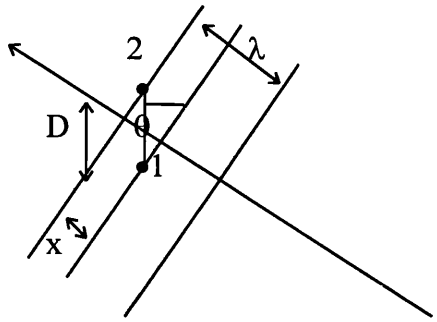

Figure 3.8: Detailed view of wavefront arriving at the transducers

Figure 3.8 shows in detail a wavefront arriving at the transducers. The objective of this pair of transducers is to measure very precisely the phase, or time, difference of each arriving wavefront and from this deduce the elevation angle, θ. Using Figure 3.8, we can show that the elevation angle, θ, can be related to the transducer spacing, D and the distance the wavefront has to travel between the transducers, x , this is shown in equation 3.2.

$$x = D \sin(\theta) \tag{3.2}$$

The ratio between the phase difference, ϕ, between the transducers and the 2 π radians is the same as the ratio between x and one wavelength, λ:

$$\frac{x}{\lambda} = \frac{\phi}{2\pi} \tag{3.3}$$

substitute x in equation 3.3 into equation 3.2:

$$\frac{D\sin(\theta)}{\lambda} = \frac{\phi}{2\pi} \tag{3.4}$$

re-arranging 3.4 to get the phase difference with respect to the elevation angle:

$$\phi = \frac{2\pi D\sin(\theta)}{\lambda} \tag{3.5}$$

Which can be solved to give the elevation angle:

$$\theta = arcsin\left(\frac{\phi\lambda}{2\pi D}\right) \tag{3.6}$$

Note that the phase angle, ϕ, wraps around at 2π., so that the range of angles which can be measured unambiguously with a given transducer spacing is also limited.

From equation 3.5, the relationship of the phase between the transducers and the elevation angle of the incident wavefront is a sine wave, with an amplitude of $\frac{2\pi D}{\lambda}$. This relationship can be seen in Figure 3.9, 3.10 and 3.11 for transducer spacings of D = 0.5λ, 1λ and 2λ respectively. Note that a phase of magnitude greater than 2π is observed as (ϕ - 2π) and a phase less than 0 as (ϕ + 2π). The solid lines in Figures 3.9, 3.10 and 3.11 are the theoretical phases, the thick lines are the measured phases and the dashed line is the phase value measured. Only the front face of the transducer, the area on the graphs in white, is able to receive signals, so the valid part of the graph is from $\theta = \frac{-\pi}{2}$ to $\theta = \frac{\pi}{2}$.

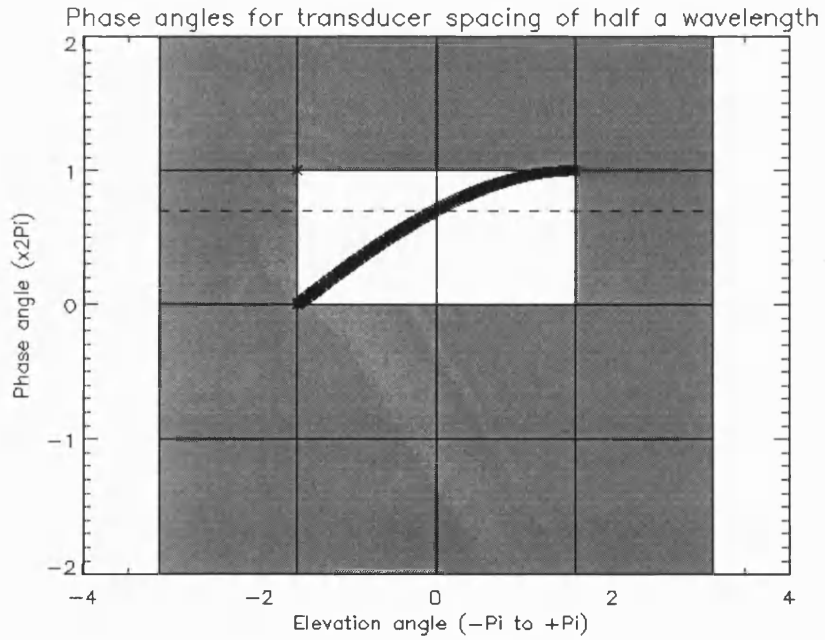

Figure 3.9: Phase angle against Elevation angle for incident wavefront, with a tranducer spacing of half a wavelength.

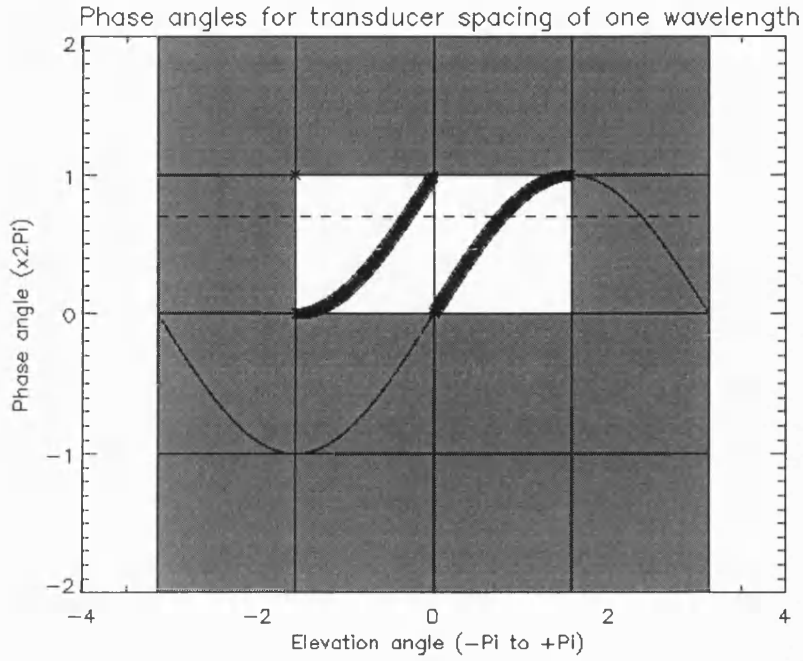

Figure 3.10: Phase angle against Elevation angle of incident wavefront, with a transducer spacing of one wavelength.

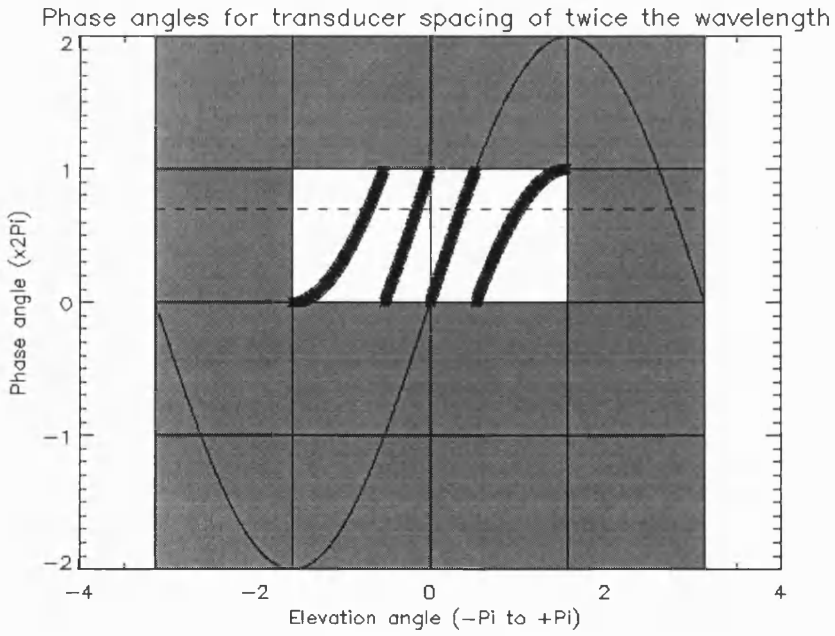

Figure 3.11: Phase angle against Elevation angle of incident wavefront, with a transducer spacing of two wavelengths.

The characteristic 'phase ramps' of an Interferometric signal may clearly be seen. The figures for 3λ and 4λ. can be easily imagined.

From Figure 3.9, the dashed line shows the output value from the phase meter. Due to the shallow phase ramp, no accurate elevation angle can be found.
From Figure 3.11, four possible solutions are presented, although the phase ramps are steeper the ambiguity cannot be resolved independently. The vernier technique used for resolving these ambiguities uses two pairs of transducers each having a different transducer spacing, like Figure 3.9 and Figure 3.11, and therefore a different ambiguous relationship between phase and angle, Figure 3.9 is used as a rough estimate and this eliminates the phase ramp ambiguity present in the more accurate Figure 3.11.

3.5.4 Accuracy

ISIS is essentially an instrument for measuring the range and angle to points on the seabed. The accuracy of this angular measurement determines the accuracy of the depth measurement which is in turn related to the depth of water under the transducers and the horizontal range.

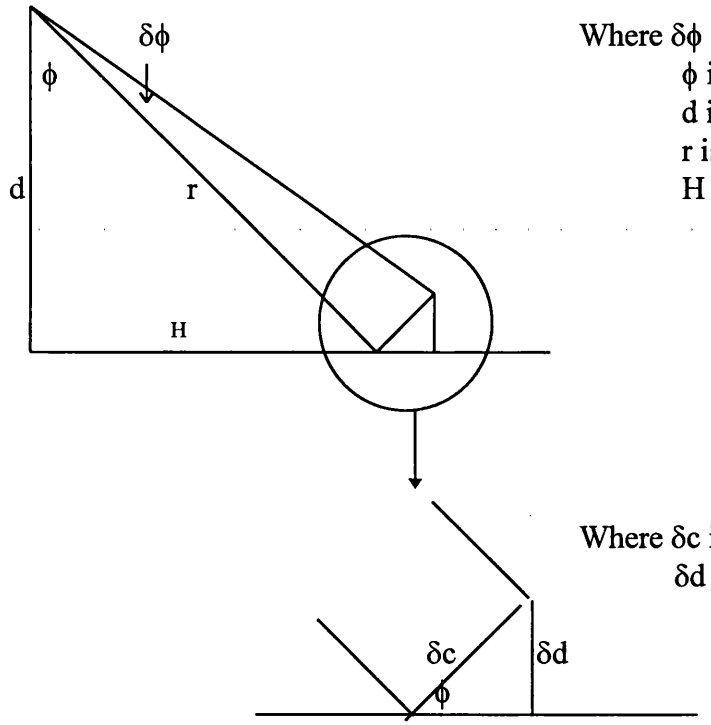

Where δϕ is the angular error in degrees
ϕ is the elevation angle in degrees
d is the water depth in metres
r is the slant range in metres
H is the horizontal range in metres

Where δc is the chord error in metres
δd depth error in metres

Figure 3.12: Geometry relating the declination angle error to depth error

If $\delta\phi$ is small, say 0.1^{o} , then,

$$\delta c \approx r \sin \delta\phi \ (\approx r \tan \delta\phi \approx r \delta\phi, \delta\phi \text{ in radians}) \quad \textbf{(3.7)}$$

From the small triangle, the depth error becomes:

$$\delta d = \delta c \sin \phi = r \sin \delta\phi \, . \sin \phi \quad \textbf{(3.8)}$$

From the large triangle

$$\sin \phi = \frac{H}{r} \quad \textbf{(3.9)}$$

If we substitute for equations 3.9 and 3.7 into 3.8 the depth error becomes:

$$\delta d = r \sin \delta\phi \, . \, \frac{H}{r} = H \sin \delta\phi \quad \textbf{(3.10)}$$

This gives the result that the depth error is independent of depth

3.6 Errors

3.6.1 Interference

An underlying assumption behind the philosophy of swath bathymetry, is that the wavefront striking the receivers is circular about the range resolution cell on the seabed which gave rise to it, and is approximately planar therefore relative to the small scale of the receiver spacing. Acoustic interference however causes this assumption to be invalid and hence there is degradation in performance.

One way to recognise this interference is to show the effect it has on the returning wavefront, consider Figure 3.13

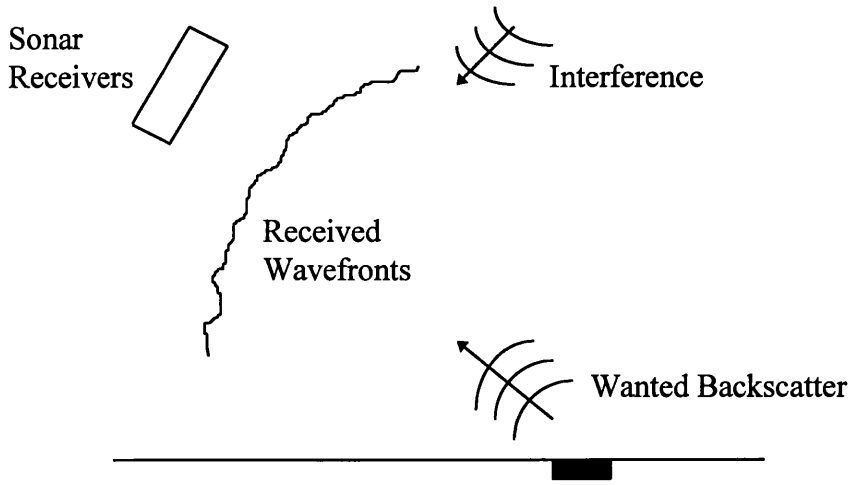

Figure 3.13: Acoustic interference will have an effect on the returning wavefront. The locus of the constant phase will no longer be a pure circle, but one with irregular corrugations.

The locus of the constant phase is no longer a pure circle but rather one with irregular corrugation.

Any estimate of the declination angle deduced from the wavefront angle at a particular point can clearly be inaccurate and ways of minimising the effects of interference are important.

Acoustic interference from the sea surface can be minimised by the following:

1. Reduce the sensitivity of the receivers in the direction of the sea surface
2. Reduce the directivity of the transmitter in the direction of the sea surface
3. Maximise seabed backscatter and minimise sea surface interference by choosing an optimal depth for the sonar and avoid operation where the seabed backscatter is weak and the likelihood of acoustic shadows arise.

It should be noted that even if sea surface interference was totally eliminated multiple scattering on the seabed might cause some acoustic interference especially in rocky areas.

3.6.2 Changes in the speed of sound

The effect of the speed of sound on a slant range is well understood but the effect it has on phase to angle decoding is less well documented.

The basic equations governing the phase decoding are given in Equations 3.5 and 3.6.

If the speed of sound (sos) changes, then the wavelength changes:

$$sos' = sos.\Delta s \tag{3.11}$$

$$\lambda' = \frac{\lambda}{\Delta s} \tag{3.12}$$

At any given elevation angle θ, a phase difference, ϕ, is measured

$$\phi = \frac{2\pi D \sin(\theta)}{\lambda'} \tag{3.13}$$

$$\phi = \frac{2\pi D \Delta s \sin(\theta)}{\lambda} \tag{3.14}$$

If sos is not accounted for, this is decoded as an angle:

$$\theta' = arcsin\left(\frac{\phi\lambda}{2\pi D}\right)$$

$$= arcsin\left(\frac{\left(\frac{2\pi D \Delta s \sin(\theta)}{\lambda}\right)\cdot\lambda}{2\pi D}\right)$$

$$= arcsin\left(\Delta s \sin(\theta)\right) \tag{3.15}$$

Equation 3.15 suggest that a linear change in sos causes a linear change to the sine of the elevation angle, and the transducer spacing is irrelevant. However, equation 3.15 was

derived without the effect of phase wrap-around being taken account of and the final equation should read:

$$\theta' = arcsin\left(\frac{\phi\lambda}{2\pi D}\right)$$

$$\theta' = \arcsin\left(\frac{\mathrm{modulus}2\pi \cdot \left(\frac{2\pi D \Delta s \sin(\theta)}{\lambda}\right) \cdot \lambda}{2\pi D}\right) \qquad \textbf{(3.16)}$$

This is not easily solved.

Consider a practical example:

Let the incident angle θ be 30°. Suppose the actual sos is 1470 m/s, but the sos of 1490 m/s is assumed inthe calculation.

Thus:

$\sin\theta = 0.5$

$\Delta s = 0.986$

The angles measured by transducer spacings d=λ/2, λ, and 4λ (at 1490 m/s) are:

λ/2: θ‘ = 29.55° so Δθ = -0.443° (Δθ =difference between 3.6 and 3.16)

λ: θ‘ = 29.55° so Δθ = -0.443°

4λ: θ‘ = 29.11° so Δθ = -0.884°

In other words, once the phase exceeds 2π, the angular error caused by the change in spped of sound does change. These phase ambiguities occurr at some elevation angle for all transducer spacings greater than λ/2.

The effect of this may be to cause the phase decode chain to fail at combinations of transducer spacing and elevation angle which cause phase angles close to 0 or 2π radians. In these cases, the decode chain 'flips' to a wrong elevation angle decode, and a filter based on comparison of angular decodes will reject the angle sample.

The actual failure will depends on the phase decode and filter algorithm used. If the sos is accurately determined at the start of processing then phase decode errors will be minimised.

Chapter 4

Sidescan Sonar Motion

4.1 Attitude system output summary

The ISIS transmitter sends out a sonar 'ping' which insonifies a long, narrow strip of the seabed. The position of this insonified strip depends on the position and attitude of the transducer at the moment of transmission. As the sonar pulse is of finite width, at any one moment, a small patch of this insonified strip backscatters sound. At some time later, determined by the speed of sound and distance; the sound arrives back at the transducers.

The receive staves of the transducer have a similar beam-shape to the transmit stave. This means that they will only receive from another long, thin footprint on the seabed. The location of this receive footprint is determined by the new position and attitude of the transducers.

The attitude systems sensors of the sidescan sonar must give information on three values, the transducer roll, pitch and yaw

Coverage of the seabed will be affected as the transducers move due to the sidescan sonar rolling, yawing and pitching. The coverage of the seabed will not be significantly affected by roll as the motion caused is within the transmit and receive beams. However, yaw (heading changes) and pitch do cause the insonified seabed footprint to move.

This has two effects; firstly, the along track coverage will be reduced as yaw and pitch cause gaps; this reduces the maximum survey speed for full seabed coverage. Secondly, as

the transducers form beams in both transmit and receive, range may be reduced if the receiver beam is moved away from the transmit beam.

Figure 4.1 shows a schematic of the geographical axis of the sidescan sonar with the direction the transducer can move.
Figure 4.2 shows how the area being scanned can be different for the transmit and the receive beam patterns.

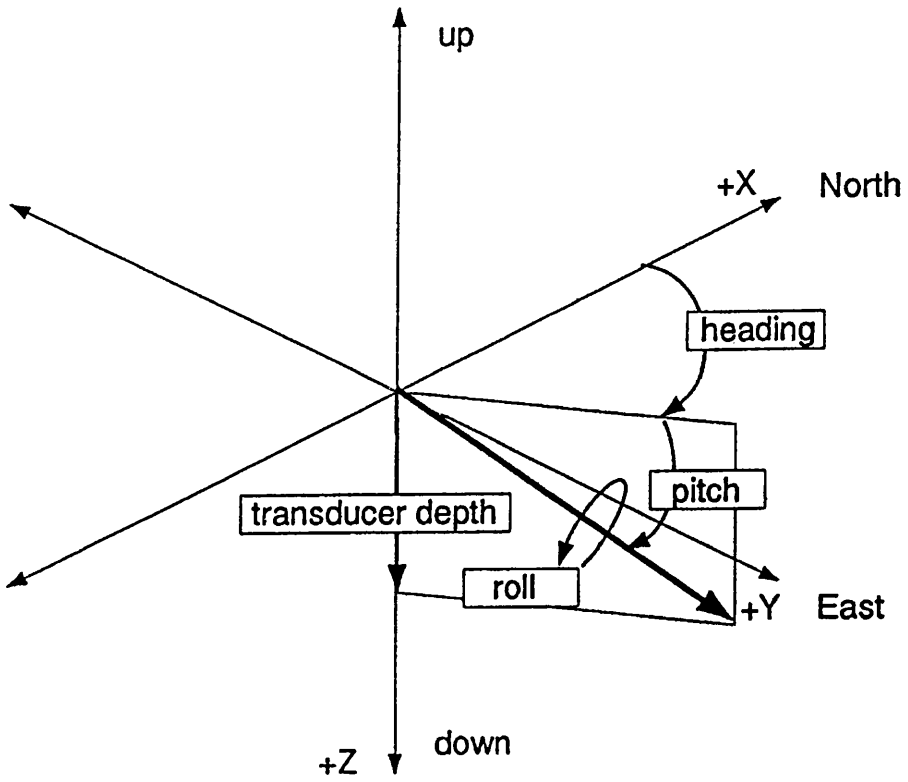

Figure 4.1: Schematic of the geographical axis of the sidescan sonar with the directions the transducers on the sidescan can move.

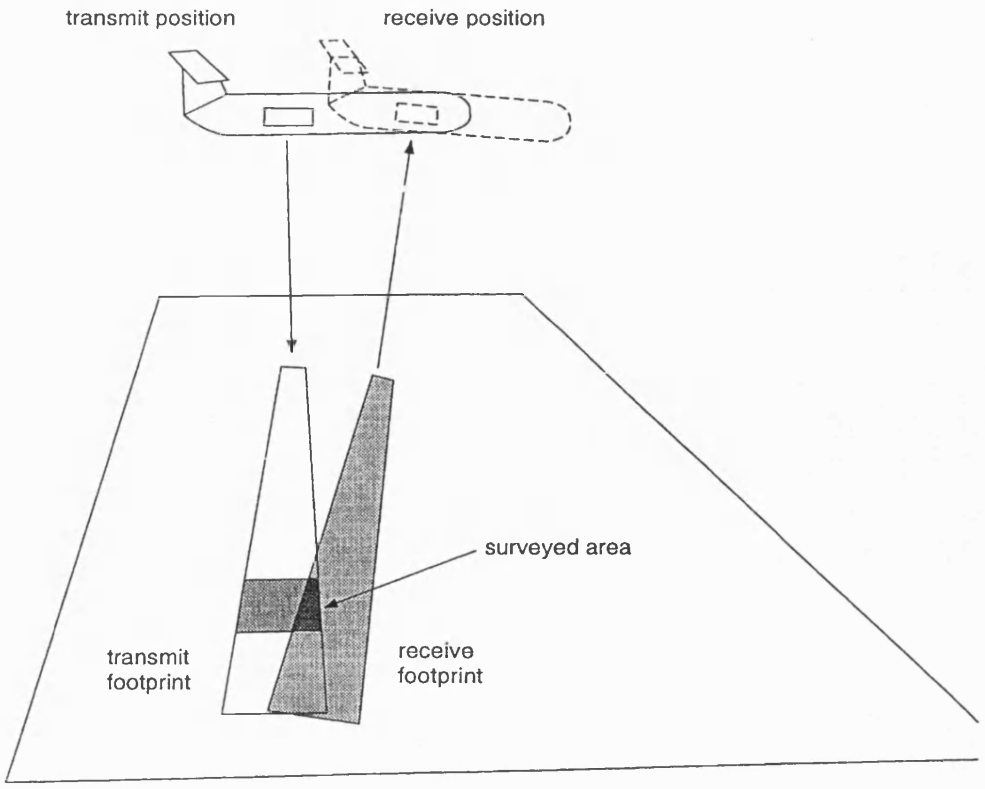

Figure 4.2: Difference in the location on the transmit footprint and the location of the received footprint.

The side scan sonar is usually towed from a vessel and it is normally connected by a cable which supplies power and a communication link to the data logger on-board the vessel.

The motion of the boat can influence the motion of the sidescan sonar. The boat can be affected by wind and sea currents. The sidescan sonar motion can be itself affected by undersea currents, changes in sea density and eddies.

These instabilities of the sidescan sonar can be separated into two classes: translational and Rotational. The translational motion describes the sidescan sonar position in 3-D space and velocity. The rotational motion relates to the orientation of the sidescan sonar and is expressed in terms of roll, pitch and yaw.

Before any corrections can be carried out to the data, these instabilities in the sidescan sonar and an understanding of what they physically mean is required.

4.2 Roll

Rolling can occur when the survey boats track runs parallel to the crest lines of prevailing swells or waves. The main effect of rolling is one of periodic compression and stretching of the sidescan image which is a result of the alteration of the orientation of the beam within the vertical plane, see Figure 4.3.

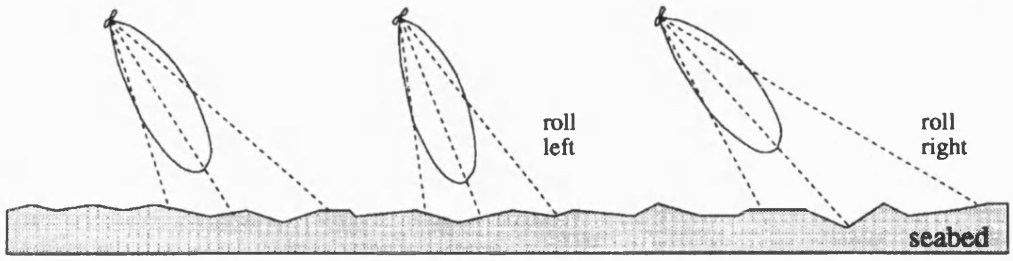

Figure 4.3: Beam coverage as the sidescan sonar rolls from left to right, the first picture is with the sidescan sonar steady, the middle picture is with the sidescan sonar rolling to the left, and the final picture is with the sidescan sonar rolling to the right. Bell, 1995.

The roll alters the depression angle at which the acoustic axis is orientated within the vertical plane and the horizontal range of the seabed insonified by the main lobe of the beam.

If the roll value is known then the data can be corrected for the beam pattern. The roll at the instant of transmission will have little effect on the resulting beam if the transmit beam is wide in the roll direction.

4.3 Pitching

Pitching occurs when the survey boat track runs directly into a heavy swell. The main effect of this is the survey boat abruptly slows down and speeds up again, this has the effect of causing the sidescan sonar to sink and rise. The subsequent rotation forwards and backwards within the vertical plane is called pitching, see Fig 4.4

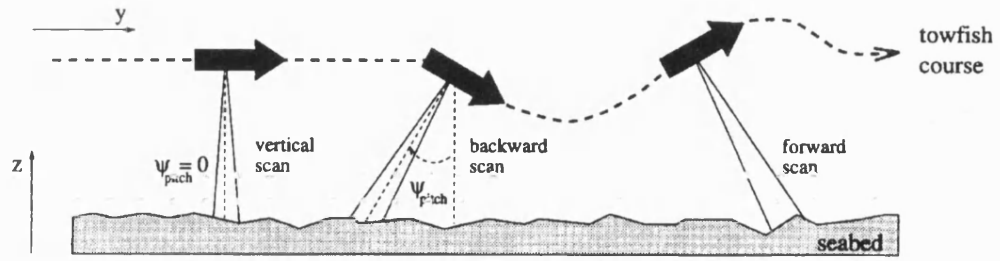

Figure 4.4: Schematic of the effects of pitch can have on the area of seabed covered. The first picture shows the sidescan sonar in a steady state, the middle picture shows the sidescan sonar pitching downwards and scanning behind itself and the final picture shows the sidescan sonar pitching upwards which causes it to scan ahead of itself. Bell, 1995.

As the sidescan sonar tilts upwards it scans forwards and as it tilts downwards it scans backwards. Although pitch has an effect in locating the transmit footprint in a fore-and-aft direction; the effect is only relatively slight

4.4 Yaw

This term is assigned to a short period off-course motion of the survey boat. The sidescan sonar will automatically follow suit, often with a short delay. The effect is that the sonar beam periodically sweeps ahead and astern along each channel.

The translational movement of the sidescan sonar in the lateral direction is depicted as the sway. The effects of this motion can be seen in Figure 4.5

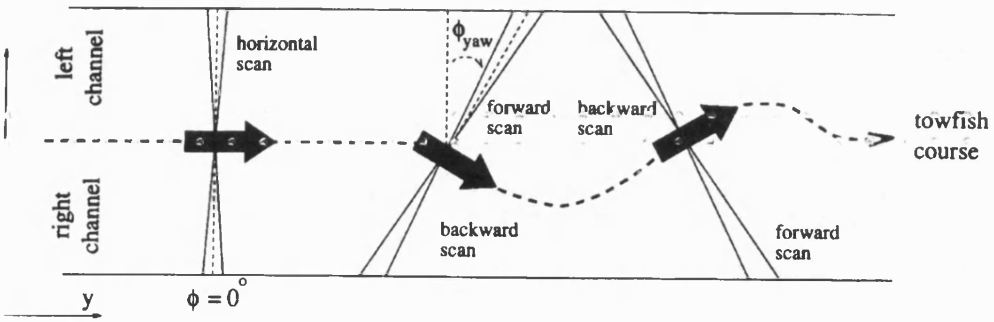

Figure 4.5: A plan view of the sidescan sonar to show the effects of yaw on the area of seabed covered. The first picture shows the sidescan sonar in a steady state, the middle picture shows the result of the sidescan sonar yawing to the right, and the final picture shows the sidescan sonar yawing to the left. Bell, 1995.

4.5 Variable ship speeds

When there is inconsistent ship speeds, then the distance covered between successive pings will vary, which can cause scale distortion, such as compression and elongation, parallel to the line of travel.

The faster the towing speed, the shorter the objects or features will appear in the along track direction. The objects will also appear on the image with less detail since fewer returns will be received for each object.

The speed variations will also distort the apparent angles of features on the seabed. This will make the determination of the targets orientation or sediment boundaries difficult.

4.6 Sidescan sonar motion

Another factor is that whilst a signal is transmitted, the sidescan sonar will be moving, so the receiving beam pattern will be moving when the return signal arrives. As the sidescan sonar motion is continuous and the receive beam pattern keeps moving ahead during the

acquisition of each line of the image. The scan lines from the maximum receive signal are bent forward as the acoustic axis of the receive beam pattern moves forward.

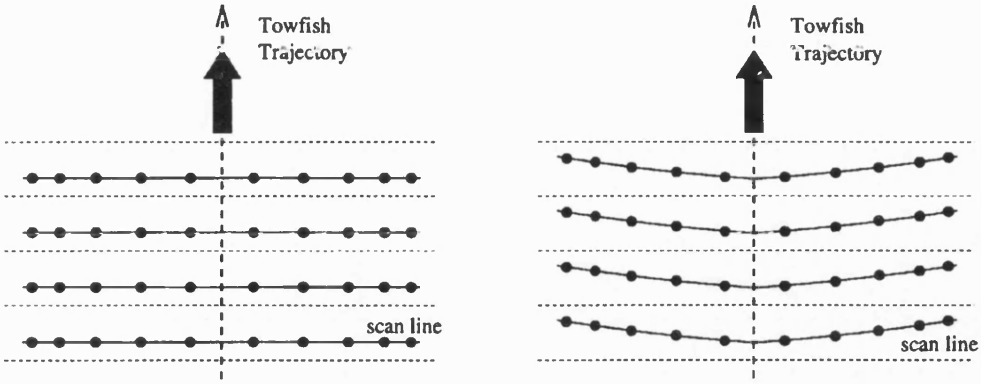

Figure 4.6: Schematic to show the effects of changes in sidescan sonar speeds. The left hand picture shows the sidescan sonar being towed at a slow speed, whilst the right hand picture shows the results of the sidescan sonar being towed at a faster speed. Bell, 1995.

Since the maximum range of the sonar is much larger then the spacing between scan lines in the along track direction, the error resulting from the approximating the scan lines as straight is minimal, but the slower the tow speed, then the smaller the error, see Figure 4.6.

4.7 Errors

Typical accuracy values for the attitude system sensors were:

Roll and Pitch = 0.1^{o}

Yaw = 0.2^{o}

The measured depth data must fall within the International Hydrographer Organisation accuracy specifications, which states that the accuracy of the depth data must be within 1% of water depth for depths greater than 30m, and 0.3m for shallower depths.

The attitude system sensors are sampled at four times the ping rate and interpolated for the whole length of the return signal, thus reducing the error due to sensor movement.

Overlapping the swath lines allows the merging of far and near range data, with benefits from the 'weighting' of the data, which allows reductions of more than 50% in depth errors.

Chapter 5

Acoustic Model

5.1 Introduction

This chapter will show how the equation used to calculate the backscatter coefficient is generated, then the terms in the final equation will be discussed in more detail and the final part of this chapter will give an overview as to how data will be analysed.

5.2 Generating the Acoustic Model

To generate an equation which relates the returned signal strength due to surface reverberation, the basic sonar equations which were introduced in Chapter 3 must be employed.

Consider figure 5.1 below and apply the basic sonar equations to get the following equation to relate the backscatter amplitudes to the backscatter coefficient.

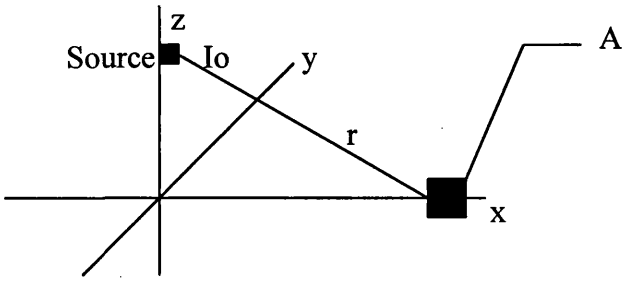

Figure 5.1: A schematic diagram to show the relation between the source and the area of seabed insonified.

5.2.1 Source Level

Let there be a sound source, which is at a slant range r from an area on the seabed A, and let I_0 be the Intensity at one metre from the source.

Energy in water is expressed by knowledge of the source level (SL) and the directivity index (DI). The source level expresses the intensity of the sound relative relative to that of a plane wave of a reference pressure, normally 1 μPa at a distance of one metre along the main acoustic axis. The directivity index of the transducer was measured during calibration.

Intensity out from the source = I_0B^2 **(5.1)**

where B is the transmit pressure beam.
The beam pattern should read $B(\theta, \beta)$ where θ is the angle from the z-axis and β is the angle from the x-axis, but for convenience it's called B.

5.2.2 Transmission Loss

As sound propagates through the water column, transmission losses will occur due to spherical spreading, scattering and refraction and have to be accounted for. The amount of loss from a signal will depend on the distance travelled and the frequency used. The return loss from the seabed will also have to be accounted for.

$$\text{Transmission Loss} = \frac{e^{-2ar}}{r^2} \qquad \textbf{(5.2)}$$

where a is the attenuation (in nepers per unit distance) of the sound over a slant range r

5.2.3 Seabed backscatter Strength

Let M be the Backscatter Coefficient to be calculated, and A be the area of seabed insonified.

5.2.4 Using the sonar equation to build the resulting linear equation

Using the sonar equation derived in Chapter 3,

Intensity out from the source = $I_0 B^2$ **(5.3)**

Intensity arriving at A, the area of seabed being insonified is calculated from the source level and the transmission loss, equation 5.1 and 5.2 respectively

Intensity arriving at A is $I_0 B^2 \frac{e^{-2ar}}{r^2}$ **(5.4)**

Intensity back from A at 1 metre is $I_0 B^2 \frac{e^{-2ar}}{r^2} M A$ **(5.5)**

Intensity back at source is $I_0 B^2 \frac{e^{-2ar}}{r^2} M A B^2 \frac{e^{-2ar}}{r^2}$

Intensity back at the source $S = I_0 B^4 \frac{e^{-4ar}}{r^4} M A$ **(5.6)**

To convert S from the intensity received at the transducer face, to received root mean square pressure the following relationship is used:

$$I_0 = \frac{P_o^{\,2}}{\rho c} \quad \text{and} \quad S = \frac{P^2}{\rho c}$$

Pressure back at the source $P^2 = P_o^{\,2} B^4 \frac{e^{-4ar}}{r^4} M A$ **(5.7)**

P is now the received pressure.

This equation now needs to be re-arranged to give us the Backscatter coefficient, M

$$M = \frac{P^2 r^4}{P_o^{\,2} B^4 A \exp^{-4ar}} \quad \textbf{(5.8)}$$

To relate the above equation to the side scan sonar datasets, a time function must be incorporated, see equation 5.9

$$M(t) = \frac{P^2(t)r^4(t)}{P_o{}^2 B^4(t)A(t)\exp^{-4ar(t)}} \qquad (5.9)$$

where t = time from transmission

This time related equation means that we can now locate the area of seabed involved relative to transmission, and from that a relationship between time, the backscatter coefficient and the grazing angle.

5.3 Parameters which make up the acoustic model

The parameters which make up equation 5.9 need to be calculated before they can be used.

5.3.1 Area of seabed insonified - A(t)

The area of seabed insonified, or the beam pattern's footprint, will grow with increasing slant range r. For each bathymetric point and backscatter amplitude value the area of seabed it relates to has to be calculated. Figure 5.2 shows a schematic of a sonar pulse as it interacts with the seabed, a more detailed picture of the geometry of the ensonification can be seen in Figure 3.5:

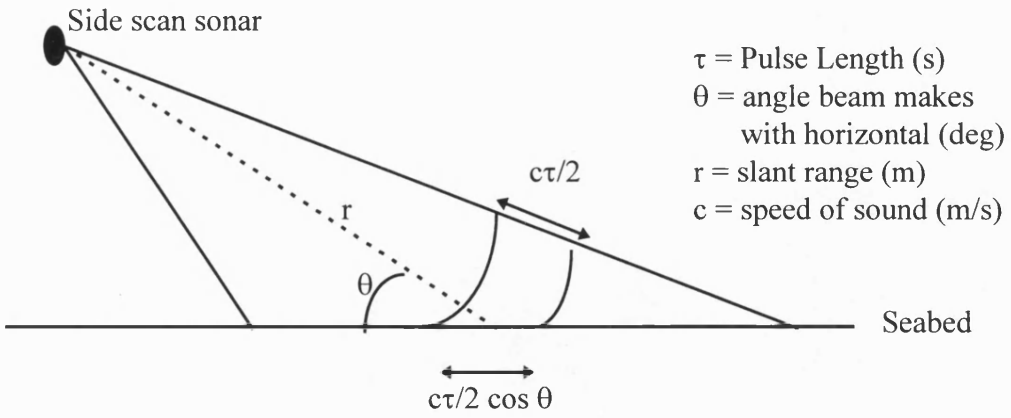

Figure 5.2: Schematic to show the geometry of the pulse.

The area of the seabed insonified is approximately:

$$A(t) = \frac{c\tau r(t)\phi}{2\cos\theta(t)} \qquad \phi = \text{horizontal beam width} \qquad \textbf{(5.10)}$$

5.3.2 Axial Pressure - P_o

This data was supplied when the system was calibrated. Knowing the sensitivity of the transmitter and the root mean square voltage applied to the back of the transmitter a value for P_o could be generated using the following relationships:

volts_to_db = 20 $\log_{10}$(volts_rms)
T = transmit_sensitivity + volts_to_db dB re 1 μPa at 1m

This value of T is then converted to Pascal's using the following:

$T = 20 \log_{10} (Po/P_{ref})$
$Po = 10^{(T/20)}$ μPa = $10^{(T/20)}$ 10^{-6} Pa

5.3.3 Sidescan data - P(t)

The data supplied were the received signal values collected from the back of the receive transducer. The data needed to be converted from the voltages supplied to the amount of Pascal's in the water on the face of the receive transducer. Knowing the receive sensitivity of the transducer we can relate the voltages to Pascal's using the following:

If the receive sensitivity is rx_sens dB re 1 Volt per μPa,
rx_ss (Volts) is the sidescan value received at the back of the transducer and the incident pressure is P(t), then equation 5.11 shows the relationship between these terms,

$$rx\_sens = 20 \log_{10}(rx\_ss/P(t)) \qquad \textbf{(5.11)}$$

Equation 5.11 can be re-arranged to give the sidescan value in Pascals

$$P(t) = \frac{rx\_ss}{10^{\frac{(rx\_sens)}{20}}} \ \mu Pa \qquad \textbf{(5.12)}$$

5.3.4 Beam Pattern - B

The value of the beam pattern will change as the slant range increases. A typical beam pattern for the system used is shown in Figure 5.3. These values for the different beam angles have to be changed from dB to linear values, this is done by using the following equation

$Beam\_value\_db = 20\log_{10}(beam\_value\_linear)$

This equation is re-arranged to give beam_value_linear.
The linear beam value is then normalised.

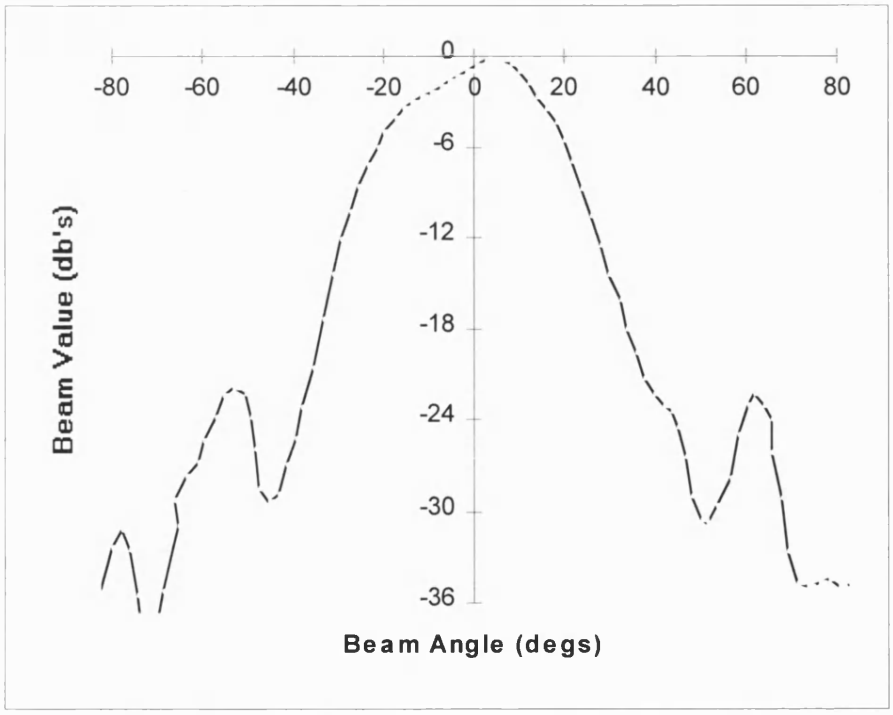

Figure 5.3: Typical beam pattern for sidescan system used

5.4 Overview of data processing

Although this subject will be covered in more detail in Chapter 6, a brief summary of the process follows.

To calculate the backscatter coefficient as a function of grazing angle a discrete number of steps is required:

1) As the data supplied is real data, it can be said to be irregular in space or time, and before any processing can be carried out on the data, a regular dataset must be generated by interpolating the datapoints to give an even distribution in time or space, this generates what is called a regular dataset.
2) Once the regular dataset for both the bathymetric and backscatter amplitude data has been generated the local seabed normals from the bathymetric data are calculated to give information on the seabed topography.
3) When a normalised vector is generated from the origin of the local seabed normal to the side scan sonar then the dot product from the two vectors and hence the grazing angle can be calculated.
4) Using the relationship developed in Equation 5.9, and applying this to the regular dataset, the backscatter coefficients for each grazing angle can be generated.
5) The topographical effects are removed from the backscatter coefficient values.

Chapter 6

Datafiles and processing

6.1 Introduction

This chapter will give an overview of the computer hardware and software used in the project followed by an introduction to the datafiles supplied by Submetrix and a brief introduction to the contents of each datafile. The problems encountered with the data supplied by Submetrix will be discussed before going on to show the method used to process the data.

6.2 Overview of the computer hardware and software used

6.2.1 Computer hardware

All data processing was carried out on a Sun Workstation, model SUN SPARC 10/51, with a ZX graphics accelerator, 1.05 Gbyte harddisk and 32 Mbytes of RAM. The data was loaded onto the system via an external exabyte drive. Storage and backup was to a SUN 4 Gbyte external harddisk.

6.2.2 Software

The system ran on the Sun Openwindows 3.3 under the operating system of Solaris 5.3. The suite of 'C' routines were written to process the data used the Sun C-compiler and the data was displayed graphically using IDL, Interactive Data Language, version 4.0.

6.3 Overview of data supplied by Submetrix

There are two main datasets: one consisting of the bathymetric and the sidescan sonars environmental information and the other containing the backscatter amplitude data.

6.3.1 Bathymetric datafile

The bathymetric dataset has the ping number, sidescan sonar position, the position on the seabed which relates to the seabed depth recorded, the environment data is the roll, pitch, yaw, heading, tide, and the depth that the sidescan sonar is beneath the sea surface. The ping number is a counter, which is used as a tag for all the data collected for each acoustic pulse, or acoustic ping, put into the water.

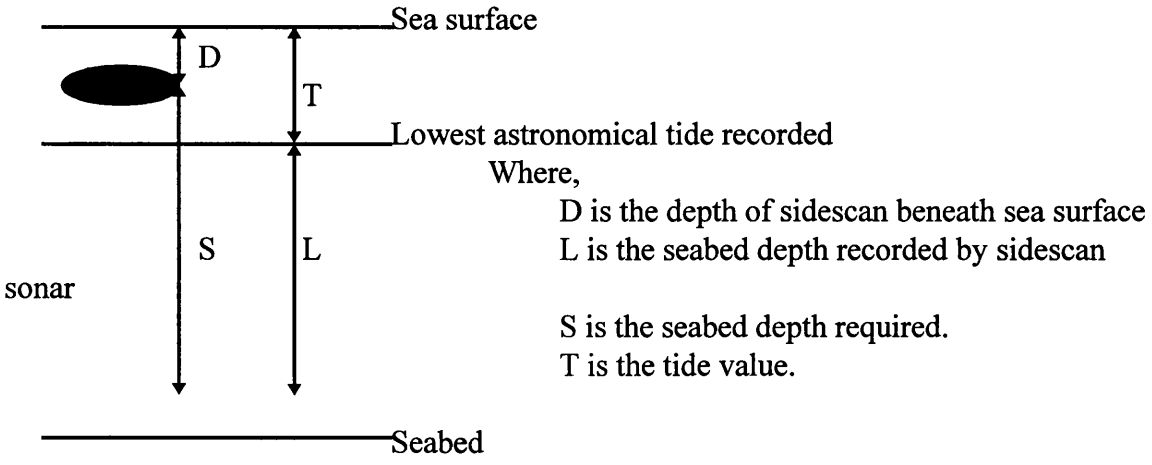

Figure 6.1: A schematic diagram illustrating the conversion required to seabed depth recorded to seabed depth relative to the lowest tide recorded.

Figure 6.1 shows the relationship between the seabed depth recorded corrected to the lowest tide recorded, L, and how this can be converted using equation 6.1 to the seabed depth beneath the sidescan sonar, S, which is required for the acoustic model.

$$S = L + T - D \qquad \textbf{(6.1)}$$

The sidescan positions and the positions for the seabed depth recorded are all in Eastings and Northings. These positions relate to the British National Grid (BNG), which can be seen on the Ordnance Survey (OS) maps. The BNG system was chosen by Submetrix as it has a regular, even sized grid system, unlike the Latitude and Longitude grid system. The BNG system has a true origin at 49° North and 2° West, and the false origin as used in OS maps is 100 km North and 400 km West of the true origins.

6.3.2 Backscatter amplitude datafile

The backscatter amplitude datafile consists of ping number, slant range in metres and 12 bit backscatter amplitude values, collected directly from the A/D chip. The backscatter amplitude values have to be converted from 'bits' to volts using the calibration data supplied by Submetrix, then from volts to Pascals.

6.4 Problems encountered with the datafiles supplied by Submetrix

6.4.1 Overview of data supplied by Submetrix

December 1994 - First co-registered 117 kHz dataset was supplied. Data was uncalibrated. Backscatter amplitude data was found to be noisy.

September 1995 - Calibration data was supplied for December 1994 dataset.

November 1995 - New 117 kHz dataset was supplied.

March 1996 - 234 kHz dataset supplied, uncalibrated.

March 1996 - Digitisation of backscatter amplitude data was found to be incorrect.

Current date - As yet no calibration data has been supplied for the 234 kHz dataset. Calibration data from a similar 234 kHz system has been supplied.

6.4.2 117kHz datasets

Many of the problems encountered with the first dataset was thought to be due to lack of calibration data, but after the calibration data had been supplied the backscatter amplitude data was still found to be poor. Submetrix eventually traced the noise in the data to the sidescan sonar itself interfering with the received backscatter amplitude signal. The 117 kHz dataset used came from the next generation sidescan sonar. This had been improved to try and generate more underfish bathymetric data, by having a fixed gain amplifier instead of a variable gain amplifier. The result of this on the bathymetric datafile is that the bathymetric data at the start and the end of the swath was unreliable. Noise was apparent in the seabed depths, see Section 6.6. Filtering routines were written which were used in the pre-processing stage of data processing to remove the bad seabed depth data, see Figure 6.5 and 6.6.

Upon processing of the data through the acoustic model it was discovered that the calculated backscatter coefficients at the end of the swath were found to be higher than those at the start of the swath, an example of this can be seen in Figure 6.2. No solution was found until the first 234 kHz dataset was supplied.

6.4.3 234kHz datasets

The first 234 kHz dataset, uncalibrated, also gave rise to higher backscatter coefficients at the end of the swath rather than at the start. The problem was traced to poor backscatter amplitude data. Submetrix take a 12-bit backscatter amplitude signal and convert it to a pseudo-16-bit backscatter amplitude signal. This meant that the resolution of the backscatter amplitude signal should be approximately 72 dB, but looking at Figure 6.3, the dynamic range of data is only 25 dB, which is around 4-bits of signal. Problems which arise from this is that due to the 'loss' of data there is little backscatter amplitude data at low grazing angles, and to try and get a sufficiently strong signal, Submetrix applied a 75 dB gain which caused the stronger backscatter amplitude signals to be clipped, an example of this problem can be seen in Figure 6.4.

Due to the lack of resolution in the backscatter amplitude signal, the seabed data had to be truncated to coincide with the end of the good backscatter amplitude data.

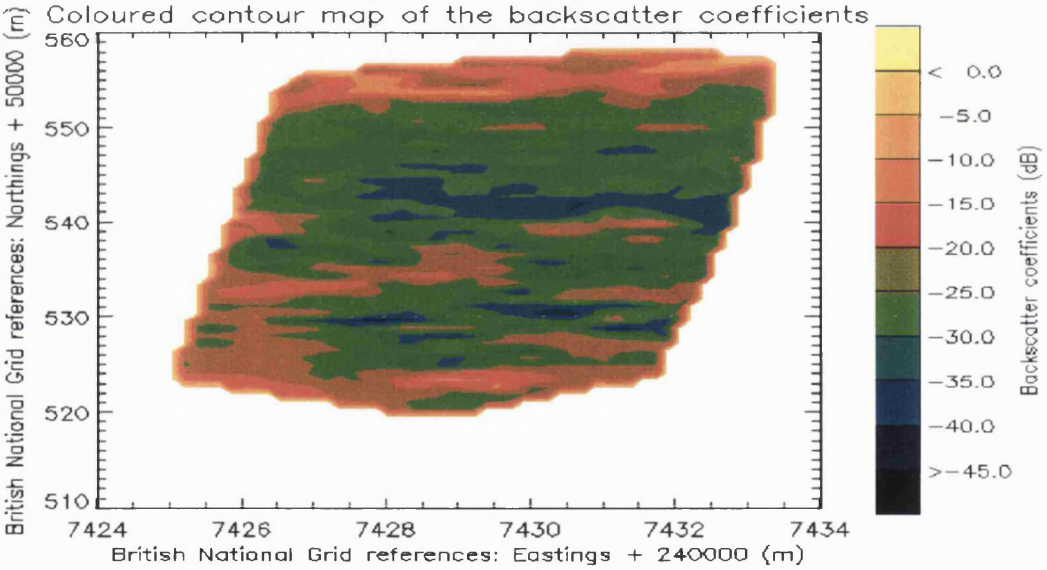

Figure 6.2: Contoured plot of backscatter coefficients to show high backscatter coefficients at the end of the swaths.

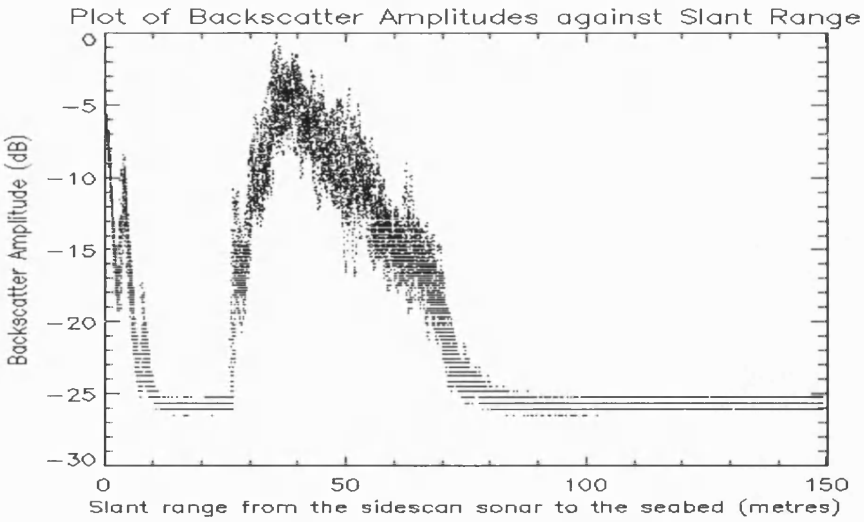

Figure 6.3: The plot shows how the backscatter amplitude values recorded on the sidescan sonar has a dynamic range of 25dB. The seabed bathymetry had to be clipped in range window to correspond to the end of the good backscatter amplitude data.

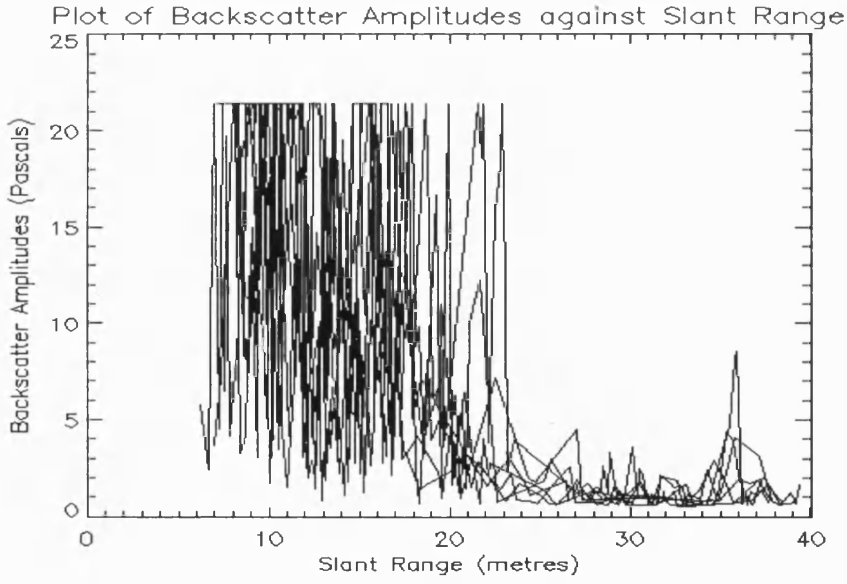

Figure 6.4: Plot of the backscatter amplitudes against slant range to show how the returned signal has been clipped when the 75dB gain was applied to the signal.

6.5 Overview of the processing software.

The data was supplied in a binary format and before any of the ISIS data could be processed, it had to be converted from binary format to an ASCII format.
The ASCII dataset contained both Port and Starboard information. This dataset was split into individual Port and Starboard datafiles, this allowed easier access to either side of the towfish datasets.
IDL was then used to graphically display the dataset.

6.6 Pre-processing routines.

All pre-processing routines were written in 'C' to aid speed of processing of the datasets. The pre-processing routines converted the dataset from binary to ASCII, split the data into Port and Starboard datasets, selected subsets of the dataset, filtered the seabed data to remove any spikes in the seabed depth points and finally linked all the good seabed depth data points to the relevant backscatter amplitude data points, which is effectively another filtering routine as there is more Bathymetric than Backscatter amplitude data.

A filtering routine is required to check the integrity of the seabed depth data. This is necessary for three reasons:

1) The ISIS system has a fixed gain amplifier. This means the ISIS system will detect any backscatter from the water column and log it to the relevant datafile, rather than just logging the first return from the seabed.
2) Interference effects can also result in spikes in seabed depth data, see Figure 6.5.
3) Poor signal to noise ratio at the far range of the signal gives rise to unreliable depth data.

The pre-processing filters detected noisy depth data and remove these datapoints.

To check the depth data at the start of each ping a sliding mean system is employed. The mean and the standard deviation for the middle section of the ping is calculated. The mean and standard deviation is then calculated for the start of the ping on a

sliding window system. When the mean and the standard deviation is within certain limits of the mean of the whole ping, then this is taken to be the start of the good data. The rest of the depth points are then compared with each other and if they change by 0.5 m, then they are rejected as bad datapoints.

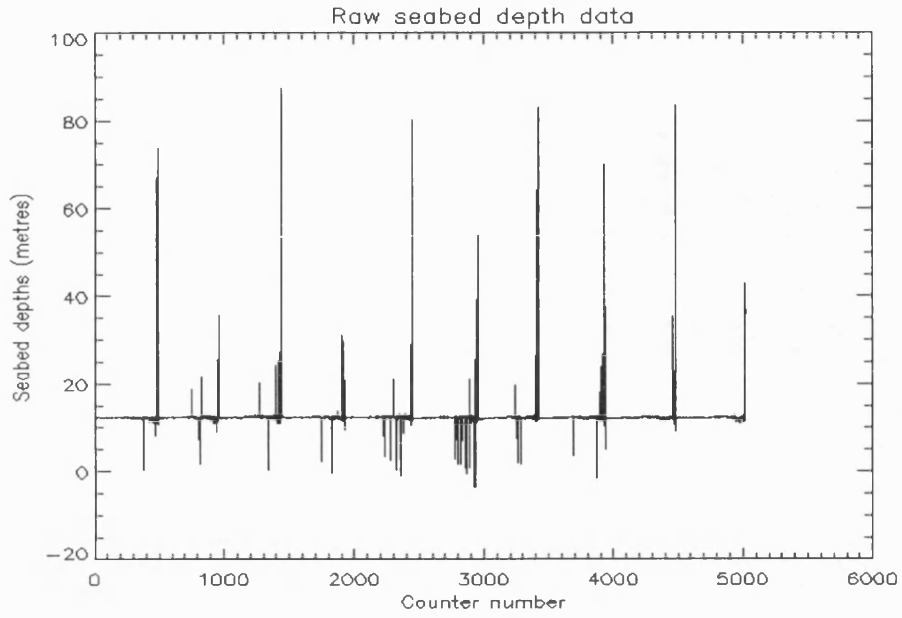

Figure 6.5: Plot of the raw seabed depth data for area of seabed under investigation.

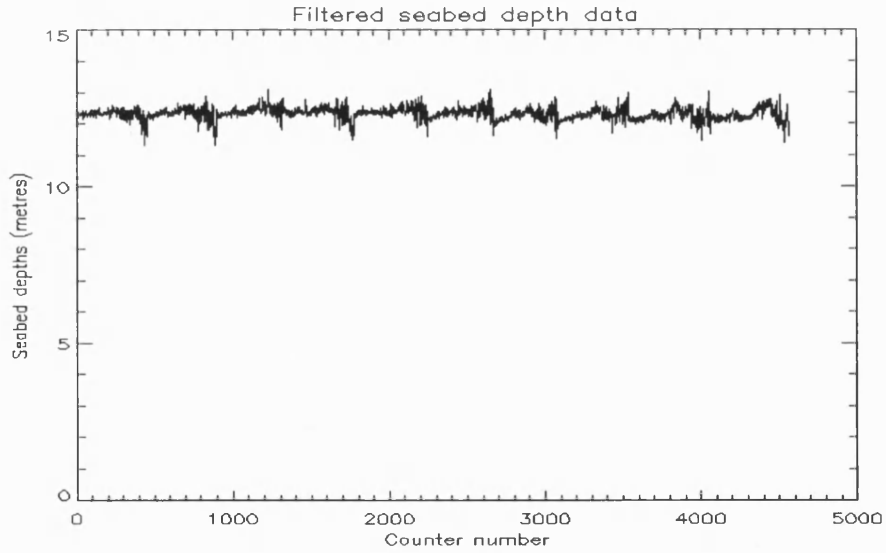

Figure 6.6: Plot of the seabed depth data after being filtered.

As the backscatter amplitude points are logged at regular time intervals regardless as to whether the signal has encountered the seabed, this results in a very regular dataset for the backscatter amplitude. The bathymetric dataset is governed by the signal-to-noise ratio and the bathymetry of the seabed which results in an irregular dataset. This routine

only allows bathymetric datapoints which can be related to a backscatter amplitude datapoint to be used.

A flow chart of this can be seen in Figure 6.7.

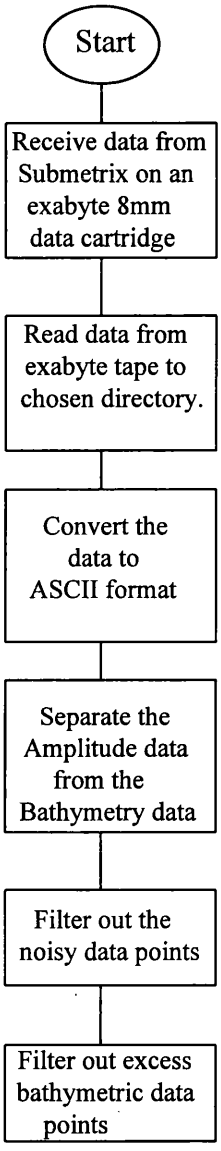

Figure 6.7: Flow chart of the pre-processing software.

6.7 Implementation of the acoustic model

There are three basic blocks which have to be calculated before the backscatter coefficient can be calculated with respect the grazing angle. These blocks all utilise the ability of ISIS to generate co-registered bathymetric and backscatter amplitude data. Firstly, the unit normal to the local seabed has to be calculated, secondly, the angle the towfish makes with the local seabed normal (the dot product) was calculated and then the backscatter coefficient with respect to the grazing angle could be calculated and the topographical effects removed.

The dataset used has the sidescan sonar travelling from West to East along Plymouth Sound, and all the figures relating to the results are from the Port dataset. This means that the lowest Northing value will be nearest to the sidescan sonar and the highest Northing value will be the furthest away from the sidescan sonar. Figure 6.14 shows a schematic of the orientation of the sidescan sonar with respect to the gridded data.

Before any of the above calculations can be carried out the selected dataset needs to be changed from an irregular dataset to a regular dataset, as this makes it feasible to relate the grazing angles to the backscatter amplitude values. The method chosen was the Delaunay Triangulation method for planar sets of points, Renka, 1984. One advantage of this method was that only areas in the dataset were linearly interpolated, this was important so as to avoid any artificial features being incorporated into the dataset, which would reduce the effectiveness of the acoustic model. The Delaunay triangulation's have the property that the circumcircle of any triangle in the triangulation contains no other vertices in its interior, interpolated values are only computed for nearby points using linear polynomial interpolation. Figure 6.8 shows 10 irregular survey data lines in brown and Figure 6.9 shows the resultant, 50 by 50, regular dataset.

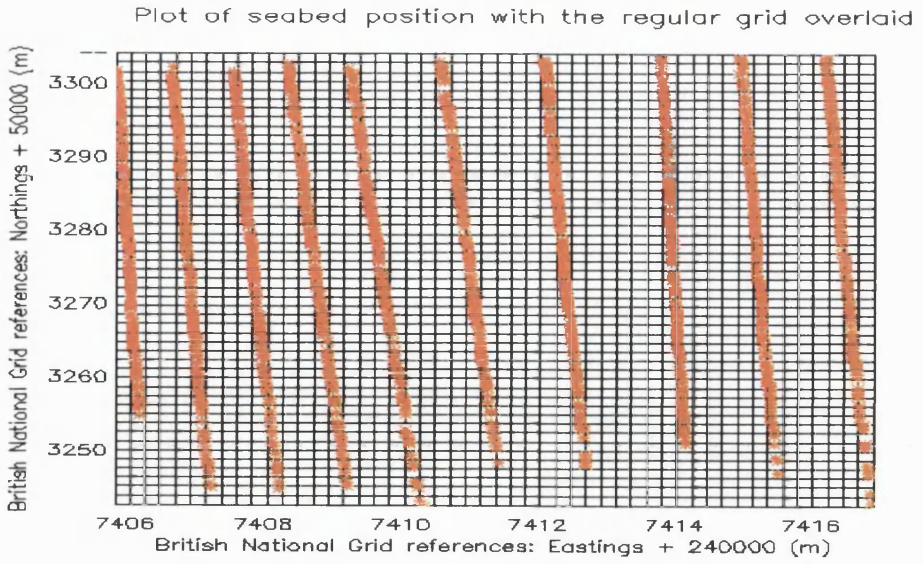

Figure 6.8: A plot showing the seabed positions with a regular grid overlaid.

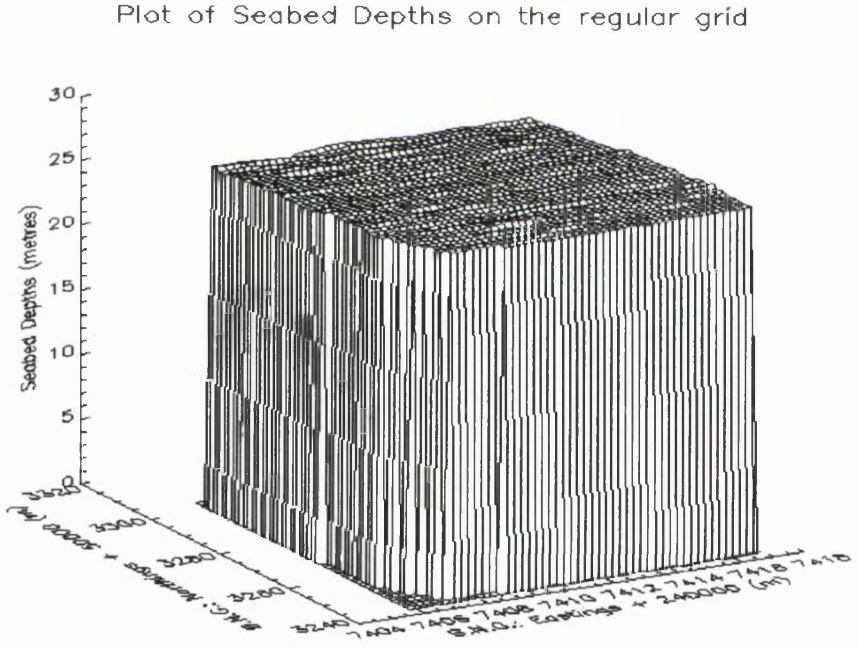

Figure 6.9: Plot of the seabed data after it has been triangulated and trigridded to generate a regular dataset.

Once a regular grid, consisting of three variables, i, j, k, which relate to latitude, longitude and depth data, has been generated around the irregular data,. For each node on the regular grid, an example of which can be seen in Figure 6.9, the local seabed unit normals can be calculated using equation 6.6.

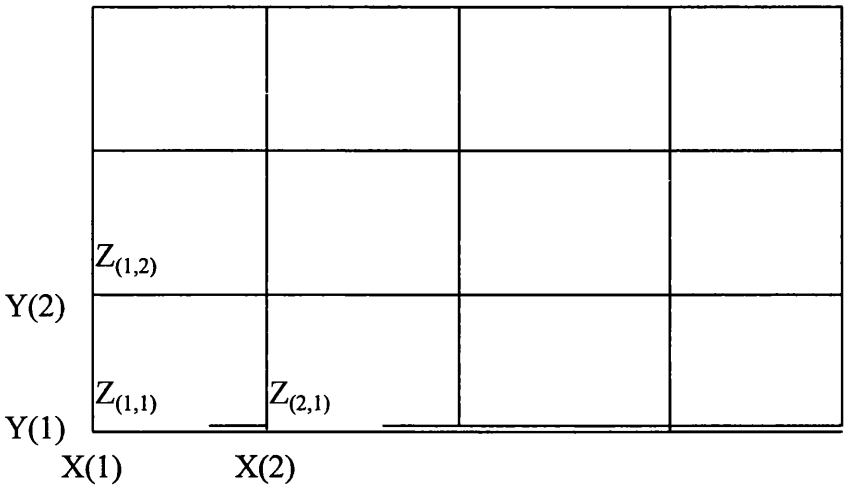

Figure 6.10: A schematic representation of the regular grid and the latitude, longitude and depth data points.

6.8 Theory for calculating local seabed normal

The vectors $\delta r/\delta x$ and $\delta r/\delta y$ need to be calculated, where $\delta r/\delta x$ represents the i, j, k components of the vector from X(1) to X(2) and $\delta r/\delta y$ represents the i, j, k components of the vector from Y(1) to Y(2).

$$\delta r/\delta x = \Delta x\, i + 0\, j + (Z_{(2,1)} - Z_{(1,1)})k = \Delta x\, i + (Z_{(2,1)} - Z_{(1,1)})k \qquad \textbf{(6.2)}$$

$$\delta r/\delta y = 0\,i + \Delta y\,j + (Z_{(1,2)} - Z_{(1,1)})k = \Delta y\,j + (Z_{(1,2)} - Z_{(1,1)})k \quad \textbf{(6.3)}$$

Taking the cross product of result from equations 6.2 and 6.3, the unit normal is calculated using the cross product technique shown in equation 6.4, which has a resultant equation shown in equation 6.5

$$\text{Normal} = \delta r/\delta x \wedge \delta r/\delta y = \begin{vmatrix} i & j & k \\ \Delta x & 0 & (Z_{(2,1)} - Z_{(1,1)}) \\ 0 & \Delta y & (Z_{(1,2)} - Z_{(1,1)}) \end{vmatrix} \quad \textbf{(6.4)}$$

$$\text{Normal} = -(Z_{(2,1)} - Z_{(1,1)})\,\Delta y\,i - (Z_{(1,2)} - Z_{(1,1)})\,\Delta x\,j + \Delta x\,\Delta y\,k \quad \textbf{(6.5)}$$

The unit normals of the resultant vector calculated by equation 6.5 is found using equation 6.6

$$\text{unit normal} = \frac{\frac{\delta r}{\delta x} \wedge \frac{\delta r}{\delta y}}{\left|\frac{\delta r}{\delta x} \wedge \frac{\delta r}{\delta y}\right|} = \frac{-\left(Z_{(2,1)} - Z_{(1,1)}\right)\Delta y i - \left(Z_{(1,2)} - Z_{(1,1)}\right)\Delta x j + \Delta x \Delta y k}{\sqrt{\left(\left(Z_{(2,1)} - Z_{(1,1)}\right)\Delta y\right)^2 + \left(\left(Z_{(1,2)} - Z_{(1,1)}\right)\Delta x\right)^2 + (\Delta x \Delta y)^2}} \quad \textbf{(6.6)}$$

From equation 6.6, the resulting unit normal vector for each node can be seen in Figure 6.10.

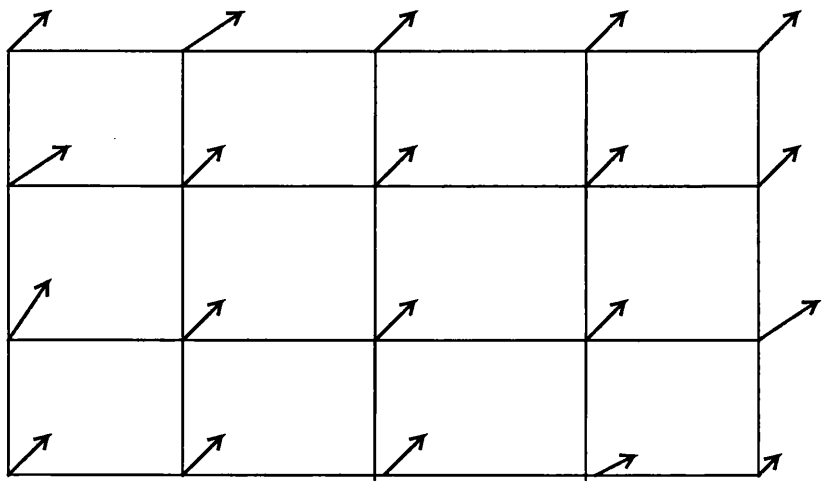

Figure 6.11: A schematic diagram showing the positions of the local seabed normals on the regular grid.

6.8.1 Resulting plots from equation 6.6

Equation 6.6 results in three arrays being formed, the unit normals for the x-axis, the unit normal for the y-axis and the unit normal for the z-axis. These results combined make up the local seabed unit normals for the regular grid. Figures 6.11, 6.12 and 6.13 show the results for each array.

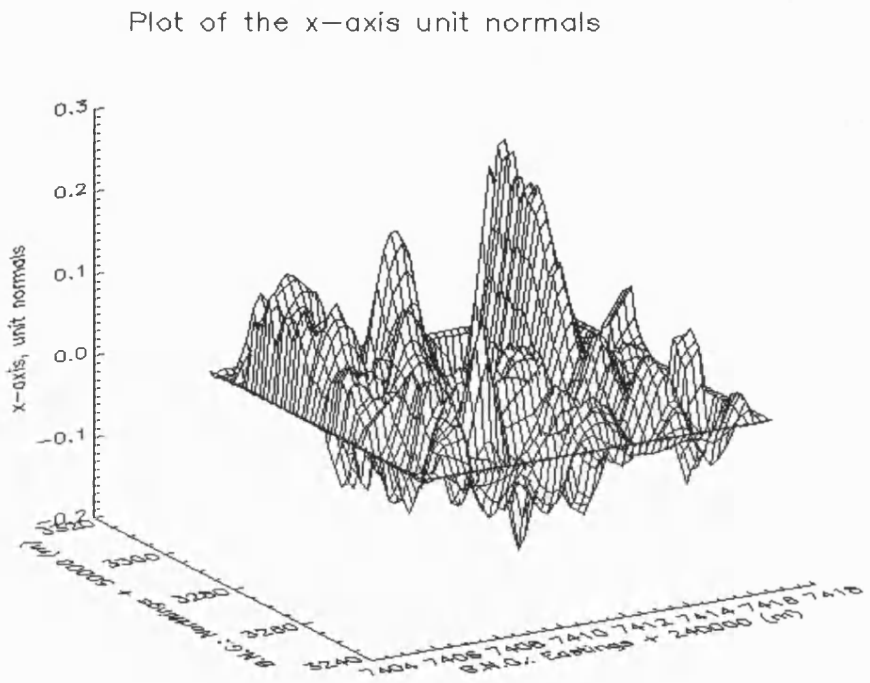

Figure 6.12: The local seabed normals for the x-axis calculated from equation 6.6.

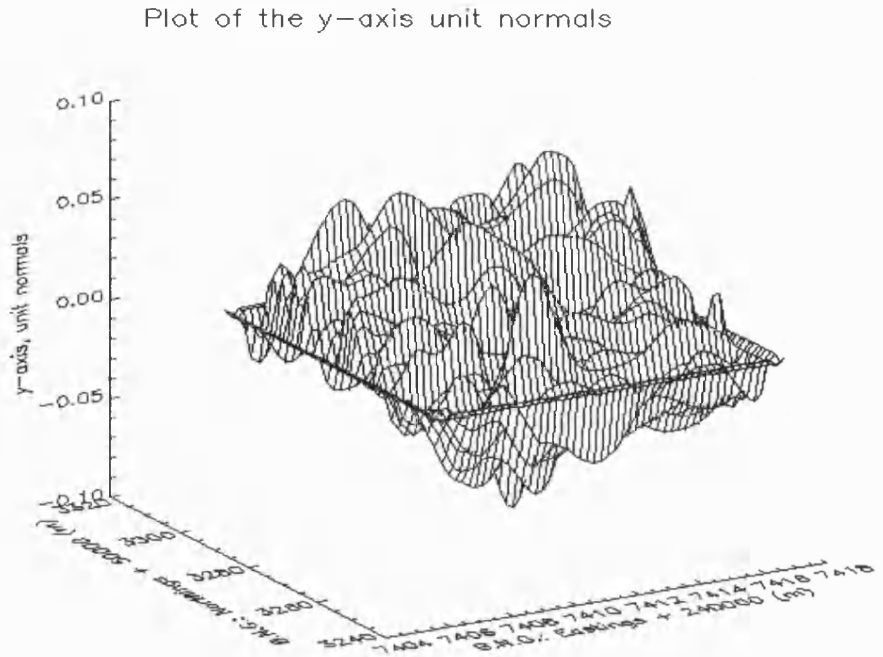

Figure 6.13: The local seabed normals for the y-axis calculated from equation 6.6.

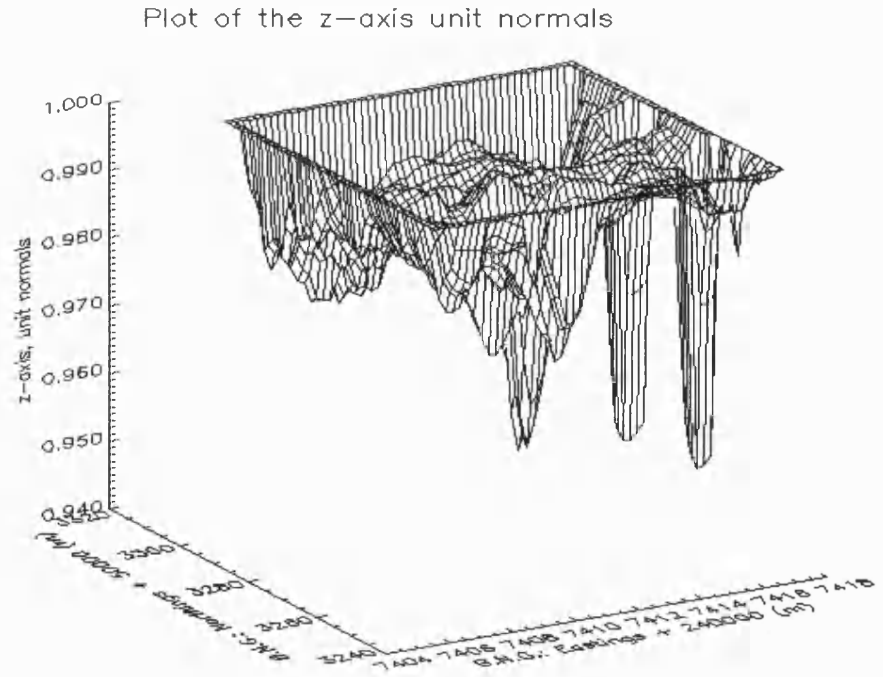

Figure 6.14: The local seabed normals for the z-axis calculated from equation 6.6.

6.9 Theory for angle fish makes to local seabed normal.

6.9.1 Calculating vector from seabed to the sidescan sonar using above nomenclature

The x, y, z component of the vector from the regular grid on the seabed to the sidescan sonar x_F, y_F, z_F positions was calculated by simply taking the difference in co-ordinate values from each other, a schematic of this can be seen in Figure 6.14.

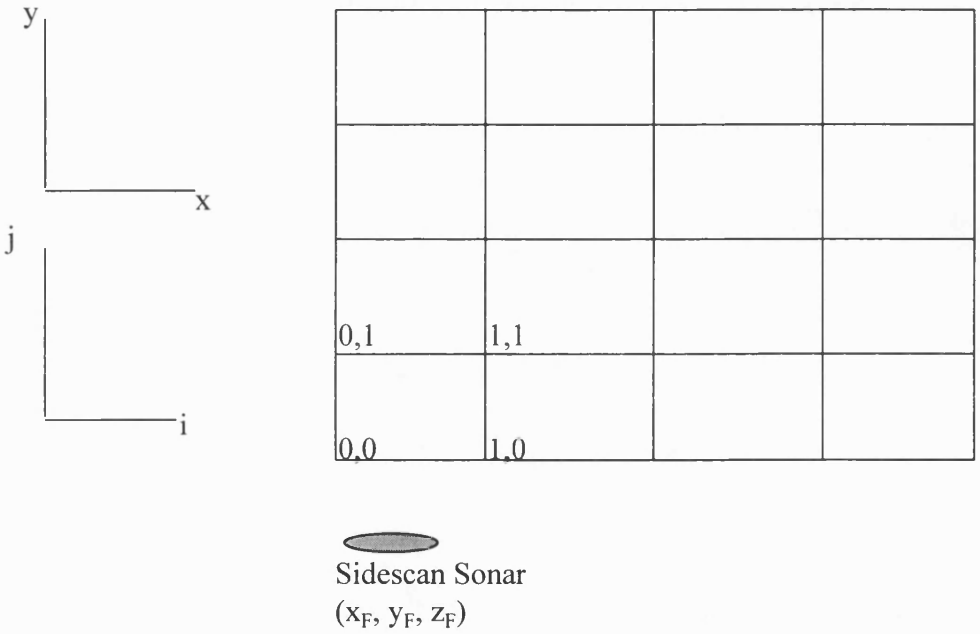

Figure 6.15: A schematic showing the orientation of the sidescan sonar with respect to the regular grid on the seabed.

Let q, denote the name of the vector array from the seabed to the sidescan sonar. Equation 6.7 is used to generate the array of x, y, and z values which represent the vector from the seabed to the sidescan sonar:

$$q(i,j) = (x(i,j) - x_F(j)), (y(i,j) - y_F(j)), (z(i,j) - z_F(j)) \quad \textbf{(6.7)}$$

The vector values are then normalised using the method described in section 6.9.2.

6.9.2 Normalising the x, y, z components of the vector from the seabed to the sidescan sonar

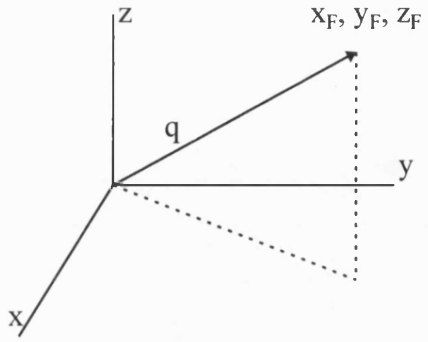

Figure 6.16: A schematic diagram showing the vector, q, from the seabed to the sidescan sonar.

Equation 6.8 is the calculation of the value with which the vector values have to be divided by to be unit normalised.

$$norm\_q = \sqrt{norm\_qx^2 + norm\_qy^2 + norm\_qz^2} \quad \textbf{(6.8)}$$

Equations 6.9, 6.10 and 6.11 show how the x, y, and z values of the vector from the seabed to the sidescan sonar are unit normalised

$$norm\_qx = \frac{x}{norm\_q} \quad \textbf{(6.9)}$$

$$norm\_qy = \frac{y}{norm\_q} \quad \textbf{(6.10)}$$

$$norm\_qz = \frac{z}{norm\_q} \quad \textbf{(6.11)}$$

As the same gridding system was used to generate the local seabed normals and the fish normals, the dot product of the two will give the angle between the local seabed normal and the fish normal, that is

$$\underline{q} \cdot \underline{n} = \cos\theta \qquad \textbf{(6.12)}$$

or,

$$\text{norm\_qx norm\_nx} + \text{norm\_qy norm\_ny} + \text{norm\_qz norm\_nz} = \cos\theta \qquad \textbf{(6.13)}$$

Figure 6.16 shows the regular seabed grid with the local seabed normal vectors and the vectors from the seabed to the sidescan sonar added. The angle, θ, shown in-between the two vectors can be calculated using equation 6.13. To calculate the grazing angle, it is simply a case of subtracting the angle, θ, from 90 degrees.

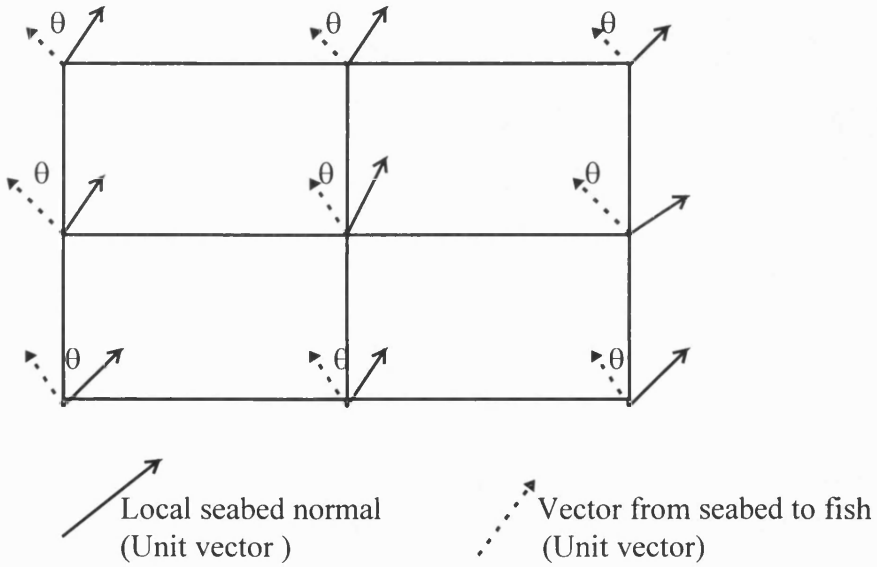

Figure 6.17: A schematic diagram of the result of both the local seabed normals and the normalised vector from the seabed to the sidescan sonar

6.9.3 Results for the calculation of the normalised vector from the seabed to the sidescan sonar.

The results from equation 6.9, 6.10 and 6.11 can be seen in Figures 6.17, 6.18 and 6.19. These figures show how the x, y and z components vary with distance away from the sidescan sonar.

Figure 6.20 is a plot of the grazing angle, calculated using equation 6.13. The grazing angle will be at its greatest near the sidescan sonar.

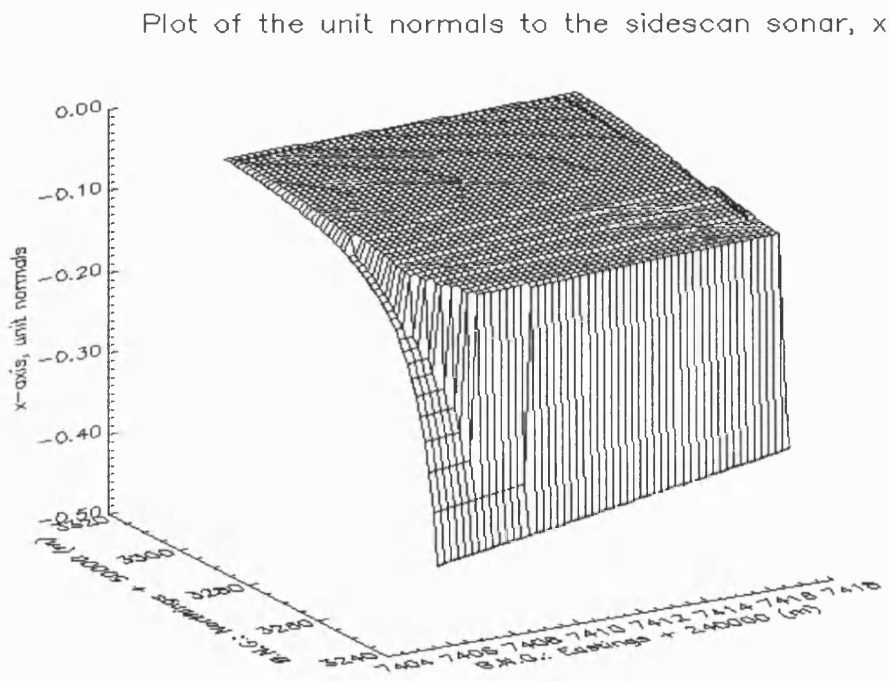

Figure 6.18: A plot of the vector from the seabed to the sidescan sonar for the x-axis

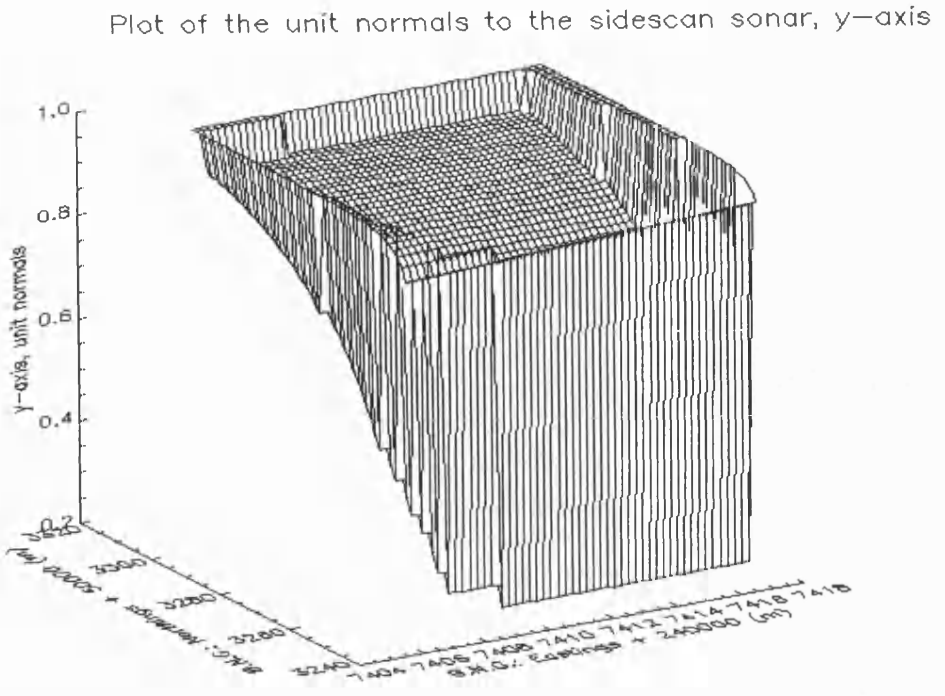

Figure 6.19: A plot of the vector from the seabed to the sidescan sonar for the y-axis

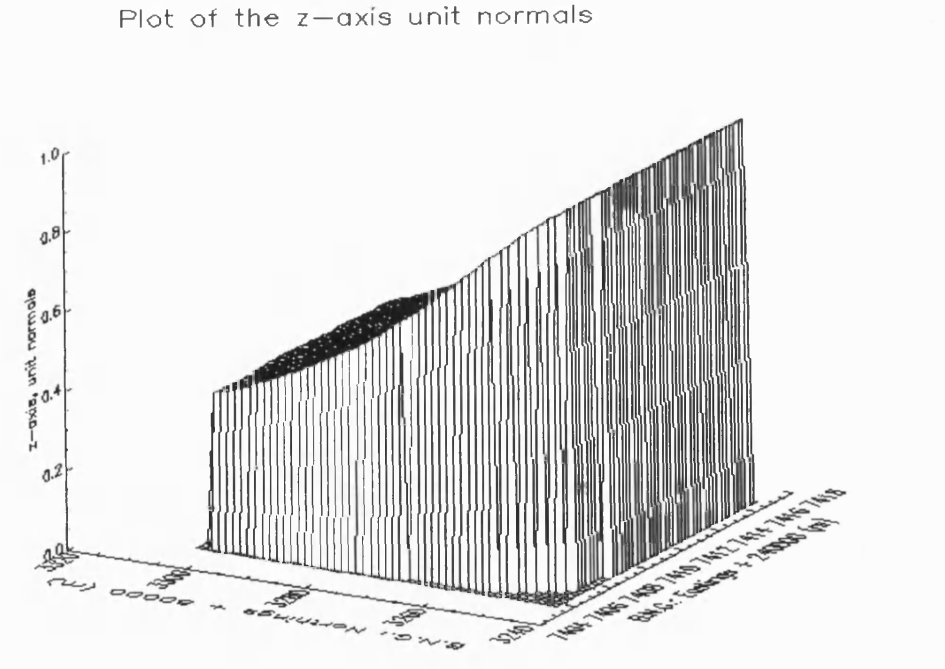

Figure 6.20: A plot of the vectors of the seabed to the sidescan sonar for the z-axis

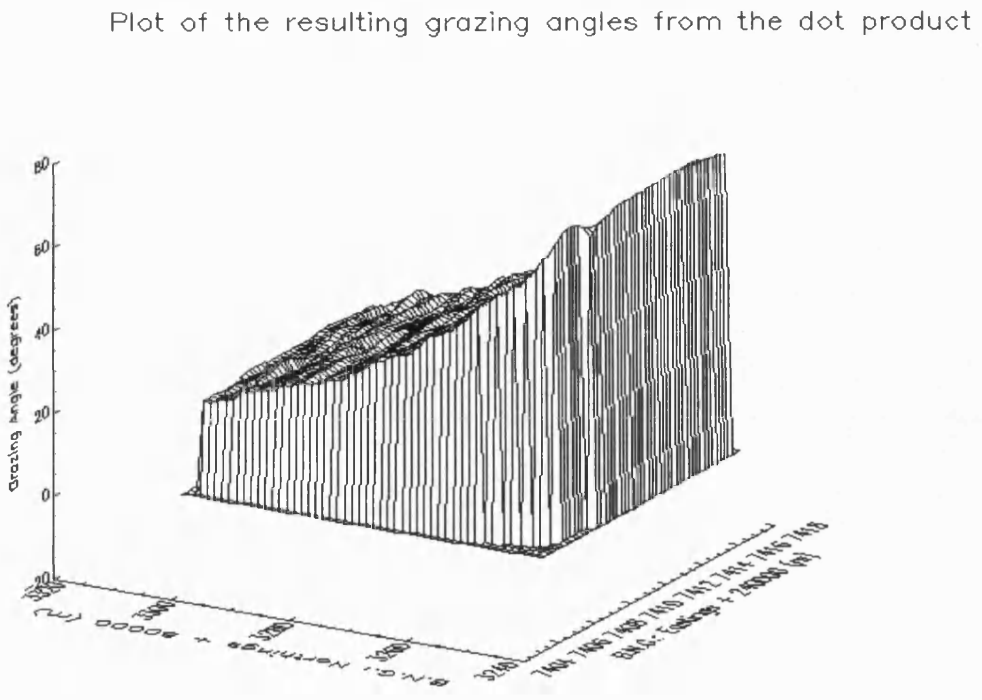

Figure 6.21:A plot of the resulting grazing angles calculated using the dot product shown in equation 6.13, and then subtracting this angle from 90 degrees.

6.10 Calculating the Backscatter coefficient

Before the backscatter coefficient can be calculated using equation 5.9 generated in Section 5.2.4, a dataset needs to be generated which accounts for beam patterns, calibration values of the side scan sonar, the sidescans environmental data, the size of the area insonified on the seabed, the area of seabed used which relates to the range of the good backscatter amplitude data, see sections 6.4.2 and 6.4.3, and the distance of the fish from the bathymetric data point. Once these have been calculated then they can be substituted into the equation to calculate the backscatter coefficient. Figures 6.21, to 6.24 are used to generate the final backscatter coefficient plot. The final backscatter plot, Figure 6.25, will have the backscatter values relative to the grazing angles, a method has been used to remove the grazing angle dependency of the backscatter values. In theory this method will be able to show areas of higher, or lower, backscatter values which may indicate different seabed types.

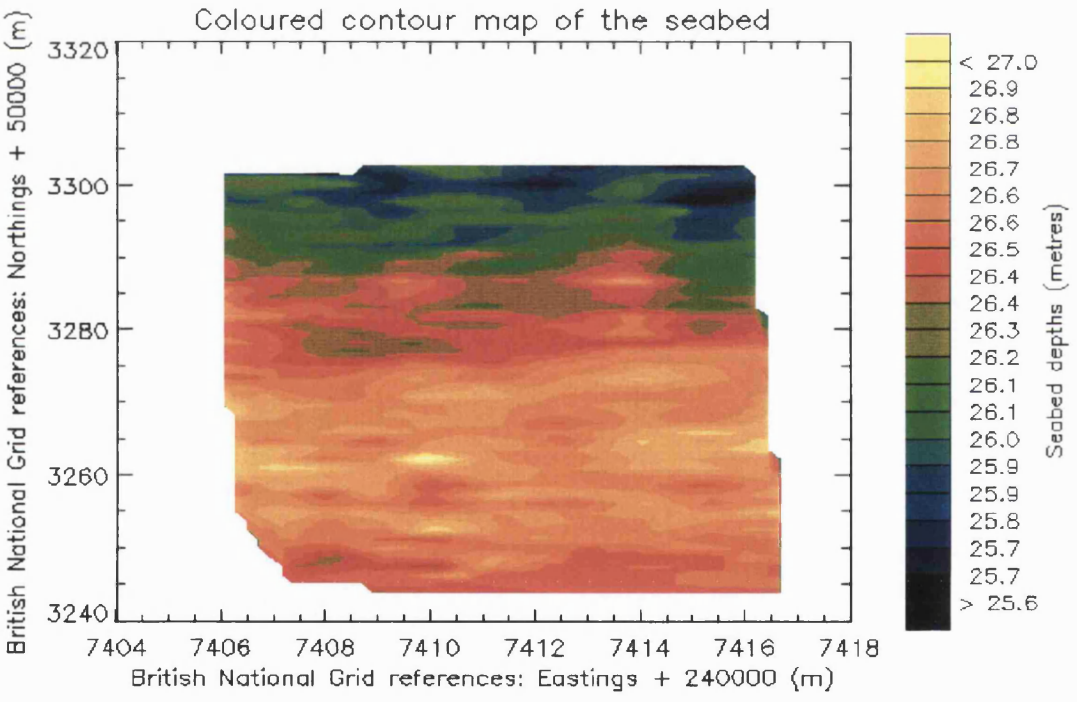

Figure 6.22: A coloured contour plot of the seabed under investigation.

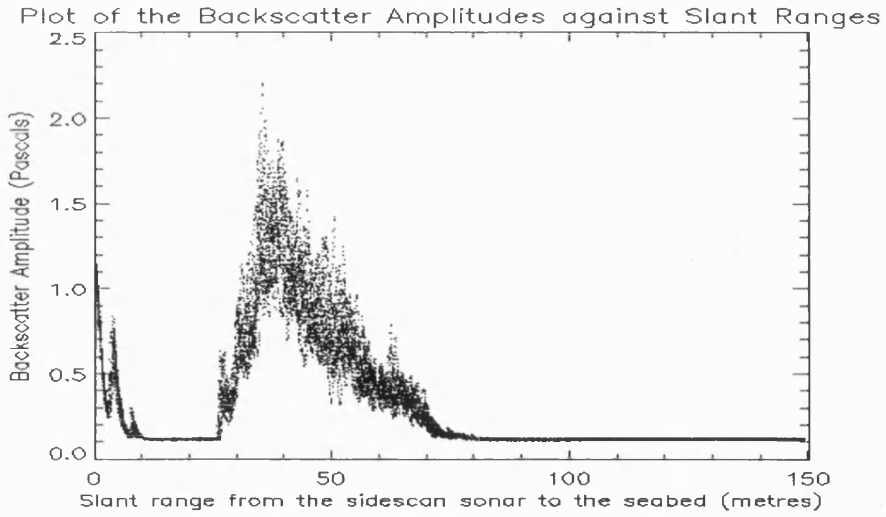

Figure 6.23: A plot of the backscatter amplitude against slant range. This shows all the backscatter amplitude data associated with one acoustic ping. The data between about 25 metres and 78 metres would be used in the acoustic model.

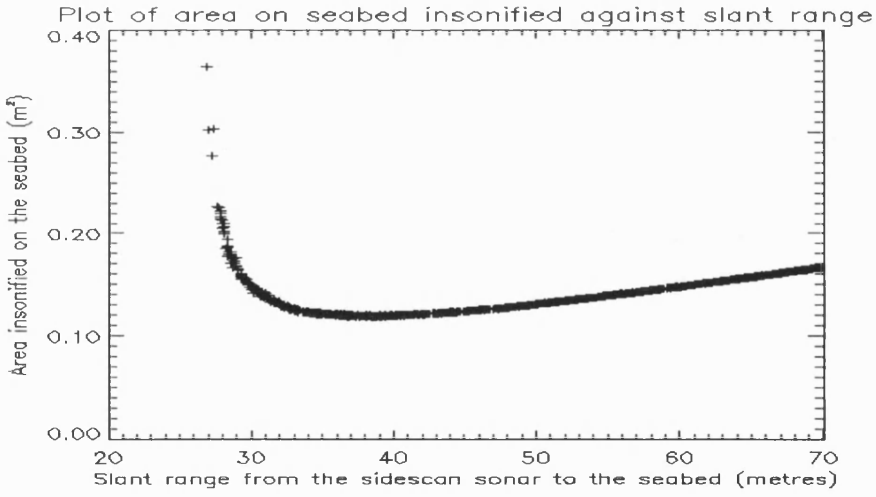

Figure 6.24: A plot of the size of the area on the seabed insonified by the beam. This is calculated using equation 5.10 in Section 5.3.1.

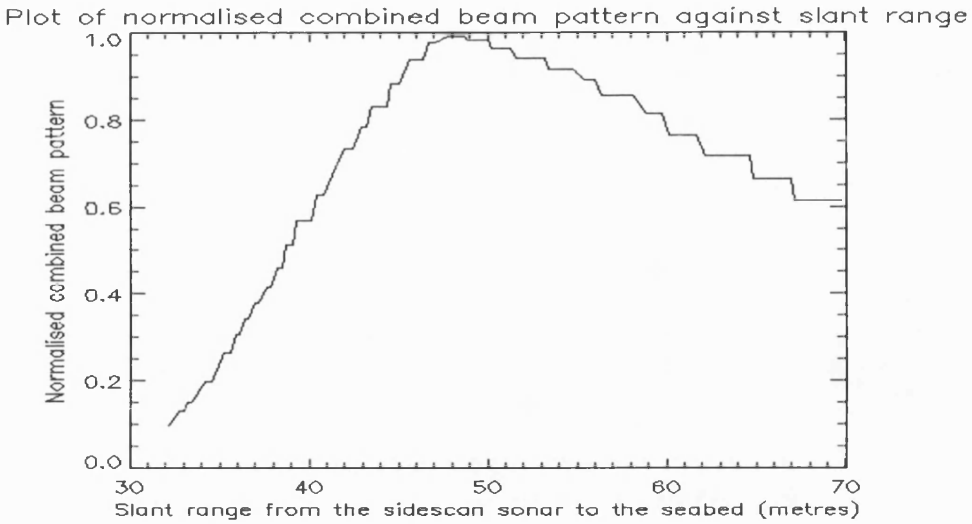

Figure 6.25 A plot of the combined beam pattern used to account for the directivity of the transducers.

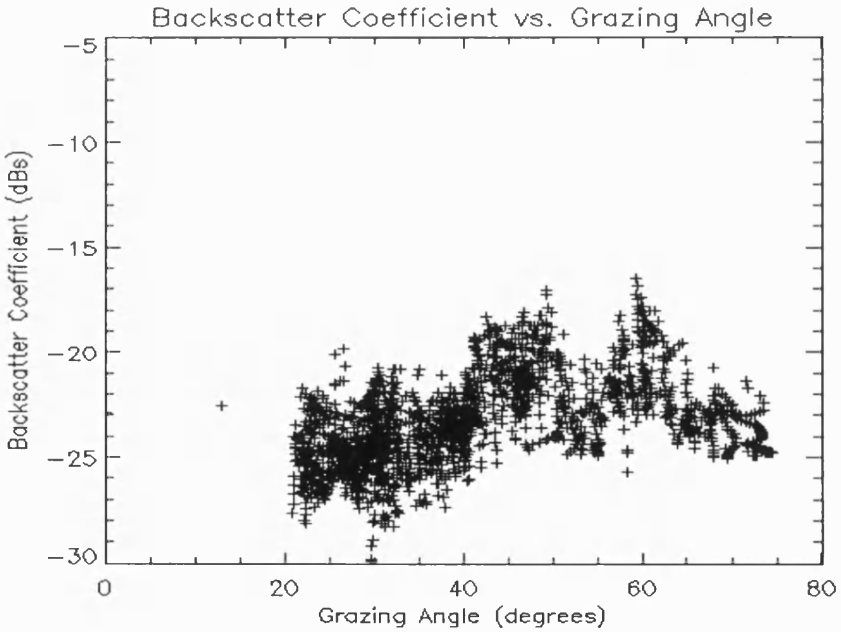

Figure 6.26: A plot of the backscatter coefficient values against grazing angle calculated using the acoustic model developed in section 5.2.4.

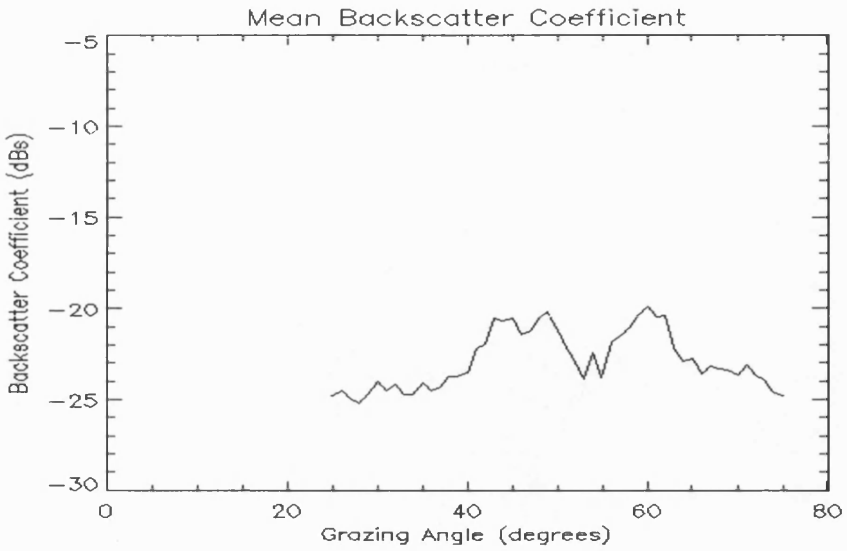

Figure 6.27: A plot of the mean backscatter coefficients against grazing angle. This was calculated by summing all the backscatter coefficient values in a 1 degree window and then dividing the result by the number of points used.

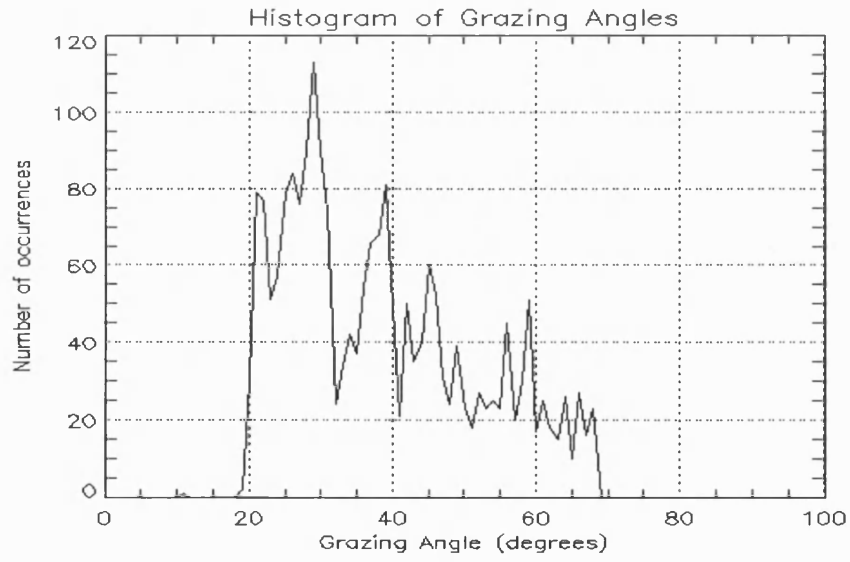

Figure 6.28: A histogram of the range of grazing angles used. The number of low grazing angles will be limited by the problems discussed in section 6.4.3.

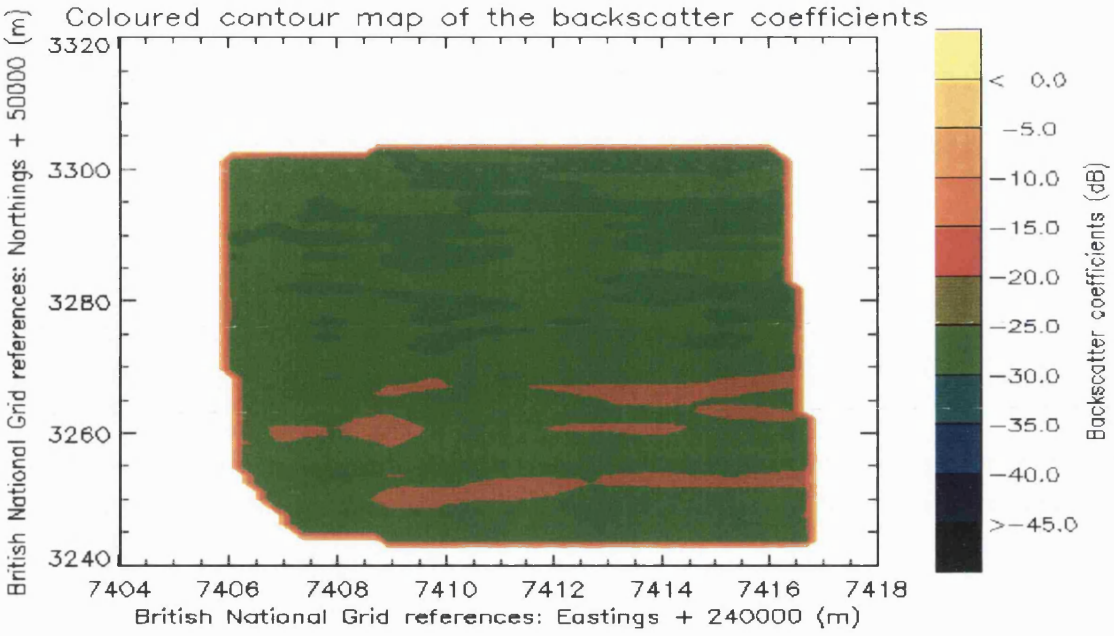

Figure 6.29: Contoured plot of the backscatter coefficient values from Figure 6.26. As a regular grid is employed the Easting and Northings can be used to generate a contour plot of the resulting backscatter coefficients over the area of seabed covered..

6.11 Removal of the grazing angle dependency

Figure 6.25 shows how each backscatter coefficient value can be related to a specific grazing angle, and Figure 6.28 shows a contour plot of these grazing angle dependent backscatter coefficients.
Both Figures 6.25 and 6.28 are plots which are dependant upon the grazing angle, low backscatter coefficients occur at low grazing angles and high backscatter coefficients occur at higher grazing angles. For Figure 6.28, this will result in high backscatter coefficients near the sidescan sonar and lower backscatter coefficients away from the sidescan sonar. If the seabed under investigation is of uniform seabed type, then Figure 6.28 would still have a relatively large range of backscatter coefficients instead of just small range of backscatter coefficient values relating to the one seabed type present, this results in a mis-leading picture.
If this grazing angle dependency could be removed by making the contour plot relative to just one backscatter coefficient value at one grazing angle, then the resultant contour plot should only have a small range of backscatter values representing the one seabed type present.

The method used to remove the grazing angle dependency has to be suitable for a wide range of cases, from shallow water which results in only a small range of grazing angle to a mixed seabed which results in a wider scatter of backscatter coefficients. Two methods were tried, the first had a pre-determined grazing angle and the backscatter coefficient found for this angle, the second chose the middle grazing angle and found the backscatter coefficient relative to this. Both methods were compared with little discernible difference between the results, but the first method proved difficult to implement as it relied upon data always occurring at the pre-determined angle.

The area of seabed under investigation, Figure 6.21 has been trimmed to the limits of good backscatter amplitude data. The area of seabed under investigation was selected as ground truthing for that area was available and a small area of seabed was chosen to ensure that only one known seabed type was present. Figures 6.25 and 6.28 show the resultant backscatter coefficient for this area of seabed, but both these results have a grazing angle

dependency. If the backscatter coefficient values could be related to one backscatter coefficient value at one grazing angle, then the grazing angle dependency could be removed, this was achieved by the following method.

Taking the results from Figure 6.25, and using the fact that every backscatter coefficient value has a grazing angle associated with it, the average backscatter coefficient value can be calculated by stepping through the range of grazing angles using a one degree window, and averaging the values, the result can be seen in Figure 6.26.

Using the dataset in Figure 6.26, the minimum and maximum grazing angle was calculated and the middle grazing angle was found, in Figure 6.26 the middle grazing angle was 50 degrees. As each grazing angle has a backscatter value associated with it, once the middle grazing angle was calculated the relevant mean backscatter coefficient value was recorded. The mean backscatter coefficients were then compared to the middle mean backscatter coefficient value using the following equation:

$$offset\_values = m\_m\_b\_c - m\_b\_c \quad \textbf{(6.14)}$$

where m_m_b_c is the middle mean backscatter coefficient
m_b_c is the mean backscatter coefficient

The offset_values generated by equation 6.14 are the mean backscatter coefficient values relative to the middle mean backscatter coefficient at specific grazing angles, and this result can be seen in Figure 6.29. A check to ensure that this method has worked would be that at the middle grazing angle the offset_value should be zero.
If this array of offset_values is added to the mean backscatter coefficient values, this would result in a straight line, with the line at the middle mean backscatter coefficient value, which would effectively mean that the grazing angle dependency has been removed.

If these offset_values are now applied to the original backscatter coefficient values, then the grazing angle dependency would be removed and the results would depend upon the scatter in the original results, equation 6.15 shows how this was achieved:

new_backscatter_coefficients = backscatter_coefficients + offset_values **(6.15)**

The results from equation 6.15 on the original dataset seen in Figure 6.25 can be seen in Figure 6.30 and Figure 6.31. Figure 6.31 has an even distribution of results with the high to low tendency in the backscatter coefficient values removed.

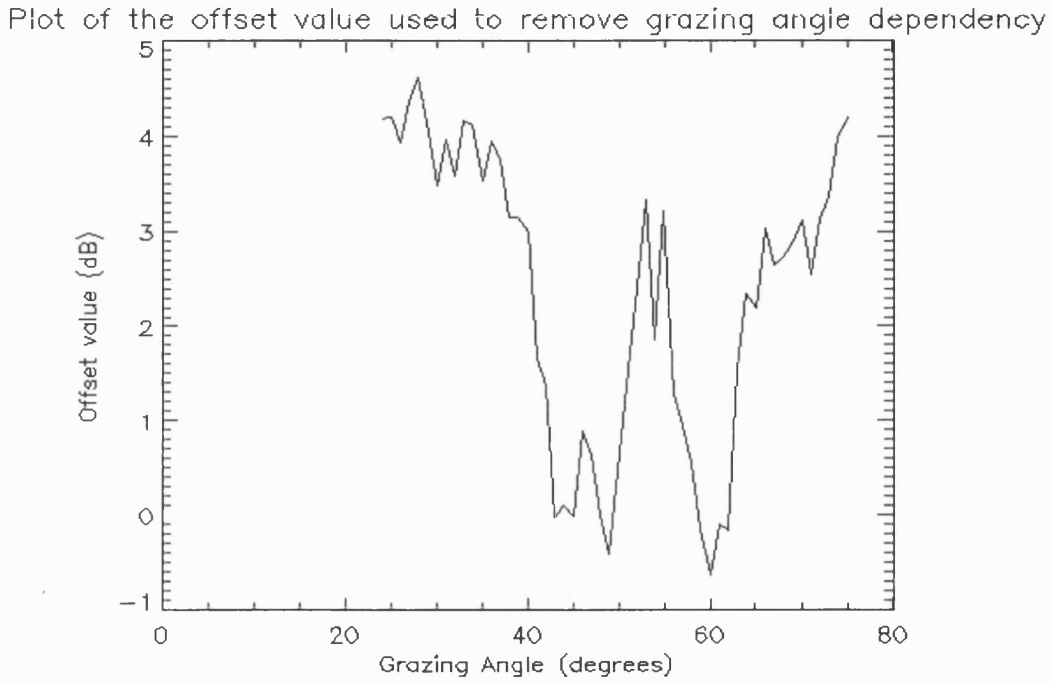

Figure 6.30: Plot of the range of offset values used to relate the original backscatter coefficients to the selected mean backscatter coefficient value.

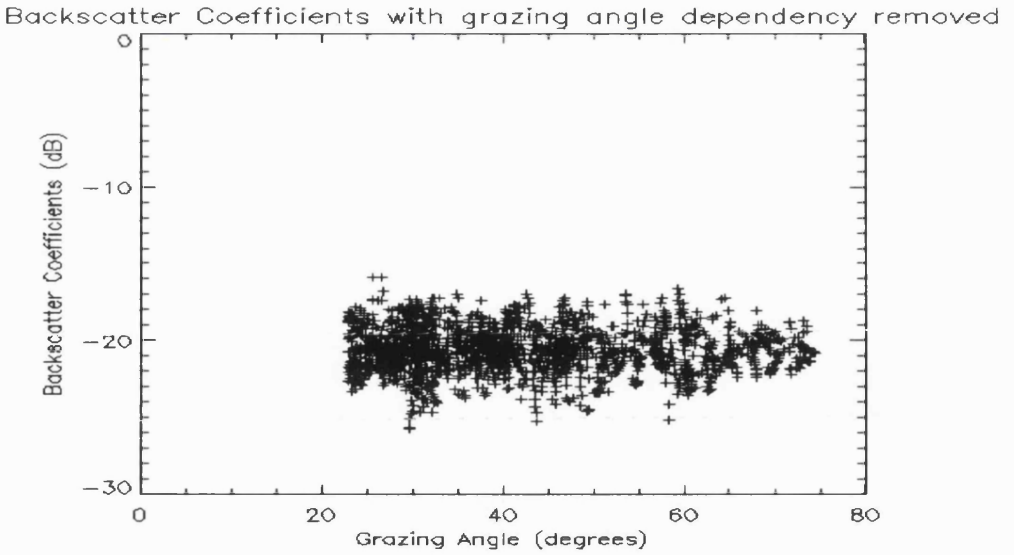

Figure 6.31: A plot of the Backscatter Coefficients corrected to the mean backscatter coefficient value at a grazing angle of 50 degrees.

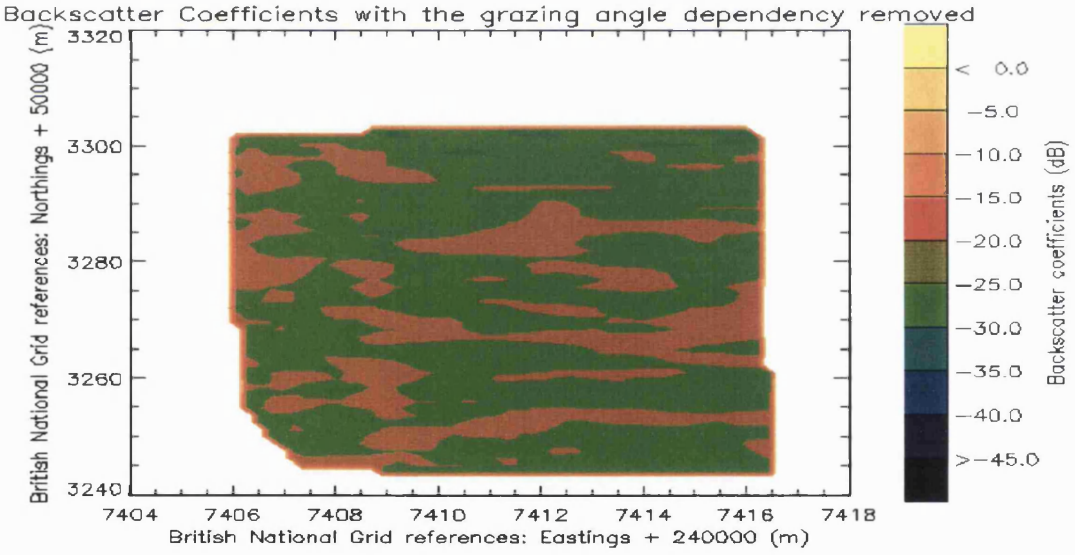

Figure 6.32: Contoured plot of the Backscatter values relative to the mean backscatter coefficient value at 50 degrees, thus removing the grazing angle dependency.

Chapter 7

Results

7.1 Introduction

This chapter will show the backscatter coefficients from different seabed types, calculated using equation 5.9. The results will be from the 117 kHz and 234 kHz datasets.
Due to the size of the datasets, they have been split into a more workable size. These smaller datasets are called Track1 and Track2 for the 117 kHz dataset, and Track 3, Track4 and Track 5 for the 234 kHz dataset.
At the start of each dataset two figures will be presented as an overview. The first figure shows a schematic of Plymouth Sound, with the seabed types and sidescan sonar track overlaid. The other figure shows the seabed depths and the sidescan sonar track.

If the track passes over an area of seabed which has ground truthing gained from Fitzpatrick, 1991 and Admiralty Chart Number 1967, 1995, then this area of seabed is isolated from the track, the backscatter coefficients calculated and five figures are then displayed. The five figures will consist of:

1) Contoured plot of the seabed.
2) Plot of the Backscatter Coefficients against Grazing Angle.
3) Plot of the Mean backscatter Coefficients against Grazing Angle.
4) Contour plot of the Backscatter Coefficients.
5) Contour plot of the Backscatter Coefficients with the grazing angle dependency removed.

Finally four plots for each dataset, if relevant, are presented, these plots cover the entire length of the dataset. To calculate the backscatter coefficients for the entire dataset a sliding window technique was employed. The window size had to be big enough to make the processing feasible but small enough so that a uniform seabed type was analysed. The compromise size of the sliding window was 10 pings and the four plots consisted of:

1) Colour coded track plot showing the average backscatter coefficients over all grazing angles for each sliding window.
2) Contoured plot of the seabed.
3) Contoured plot of the Backscatter Coefficients.
4) Contoured plot of the Backscatter coefficients with the grazing angle dependency removed.

A summary of the resulting backscatter coefficients against grazing angle for different seabed types can be seen at the end of this chapter.

7.2 Plot of Plymouth Sound with key to symbols

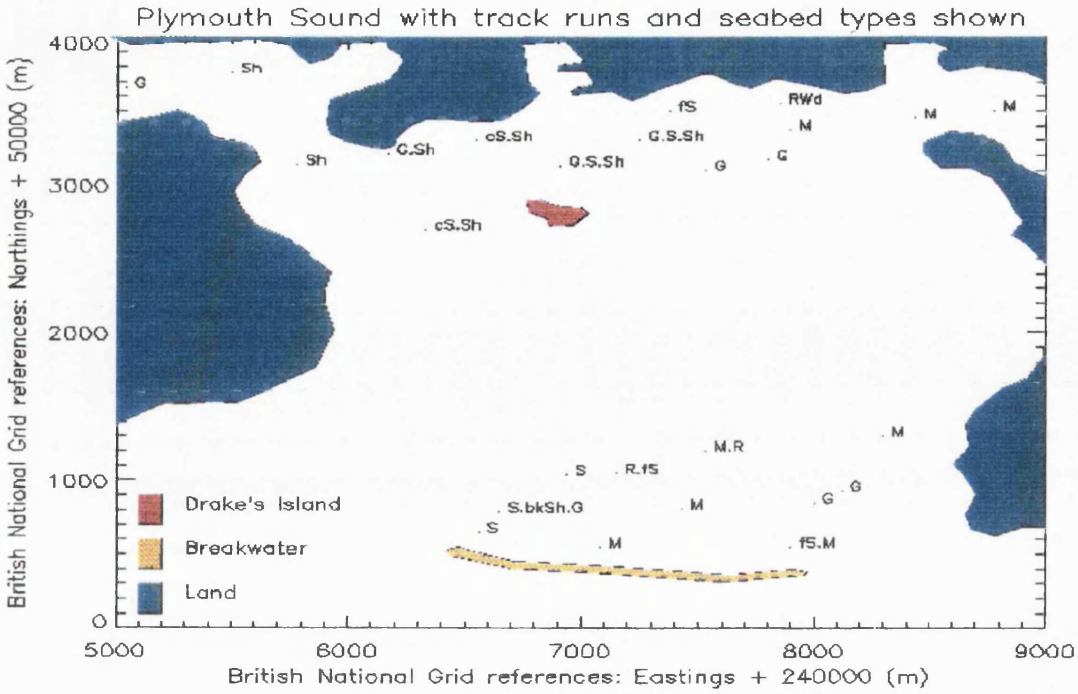

Figure 7.1: A plot of Plymouth Sound with the ground truthing overlaid.

7.2.1 Key to the symbols representing seabed types

The following provides a key to the symbols used in Figure 7.1, for further details on these symbols, see Admiralty Charts, 1973.

G	Gravel
Sh	Shells
S	Sand
R	Rock
Wd	Weed
M	Mud
bk	Broken
f	fine
c	coarse

These individual symbols can be combined to give a description of the seabed, the following is an example:

R.Wd	Rock and Weed
fS	fine Sand
S.bkSh.G	Sand, broken Shells and Gravel

7.3 117kHz dataset - Overview of Track 1

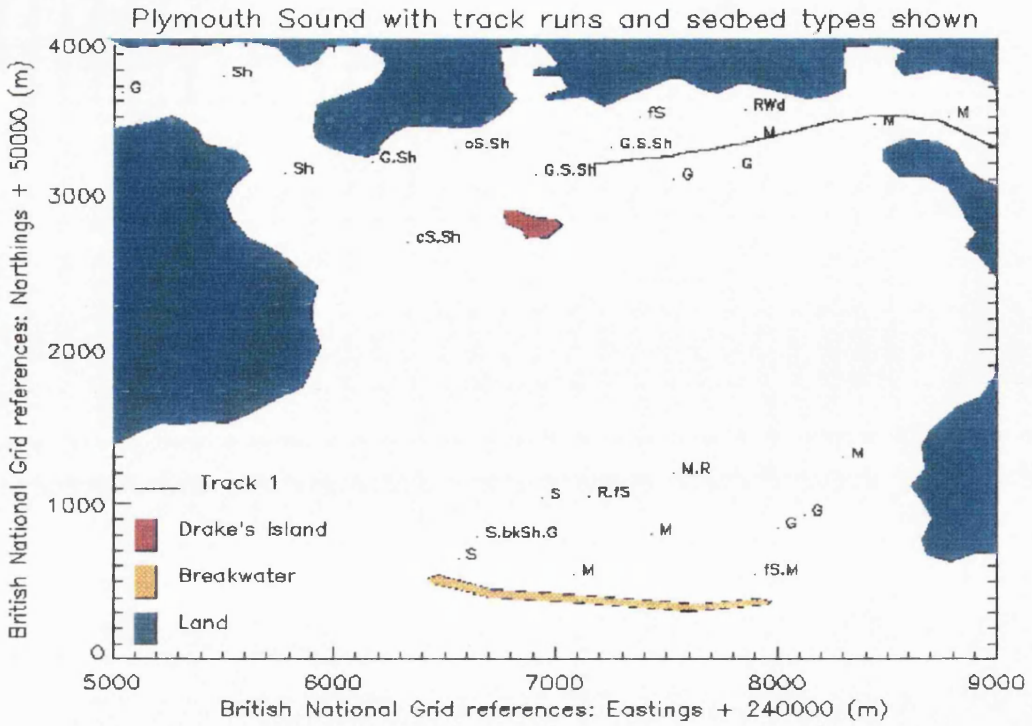

Figure 7.2: Schematic of Plymouth Sound, with seabed types and Track 1 overlaid. For key to seabed symbols see section 7.2.1.

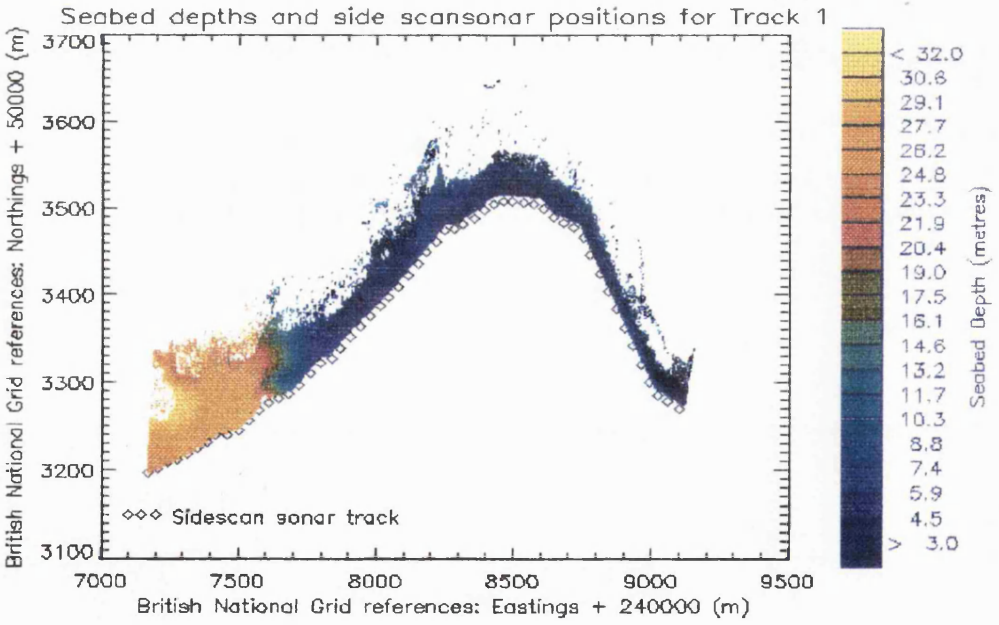

Figure 7.3: A plot of seabed depths with sidescan sonar positions overlaid.

7.3.1 Results for seabed type: Mud

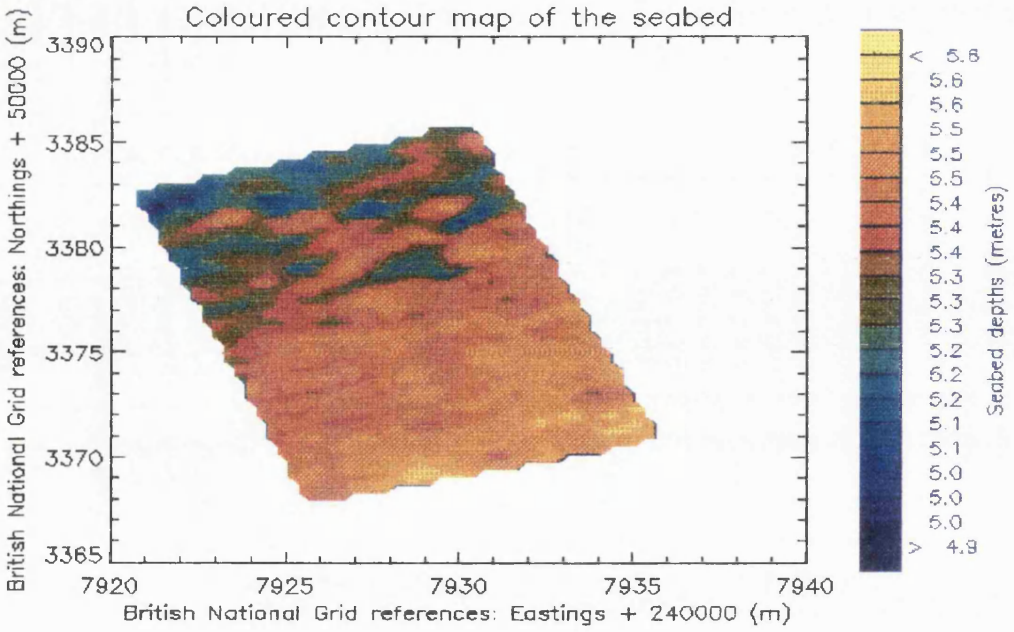

Figure 7.4: Contour plot of seabed under investigation. Seabed type: Mud.

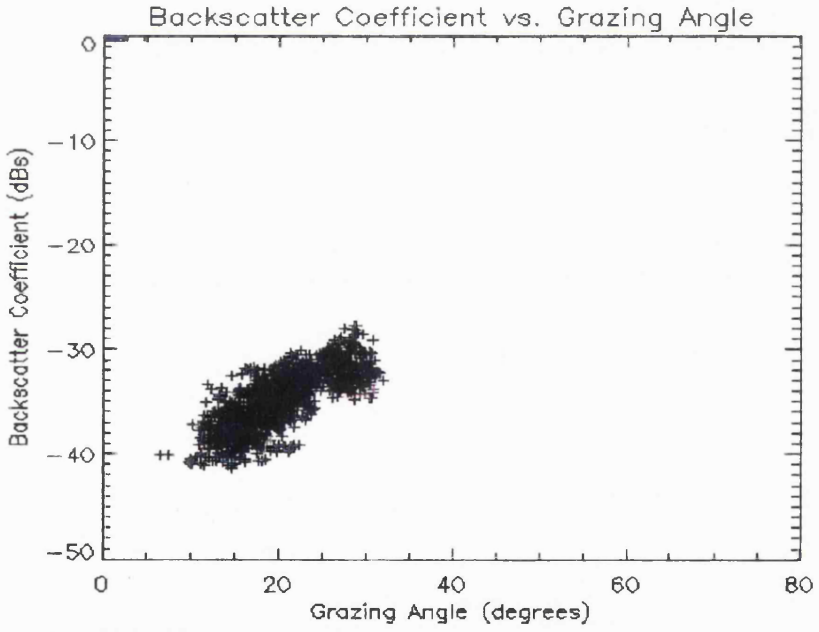

Figure 7.5: A plot of Backscatter Coefficient against Grazing Angle. Seabed type: Mud.

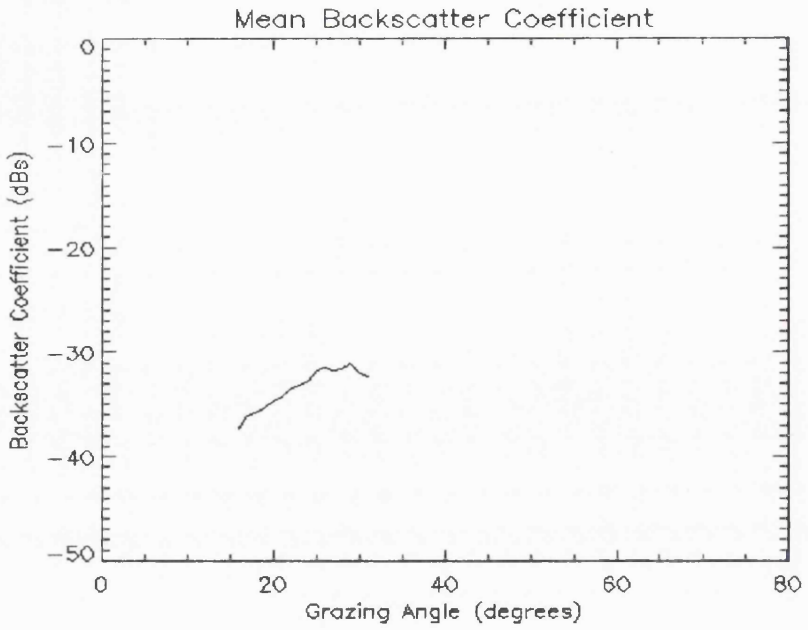

Figure 7.6: A plot of Mean Backscatter Coefficient against Grazing Angle. Seabed type: Mud.

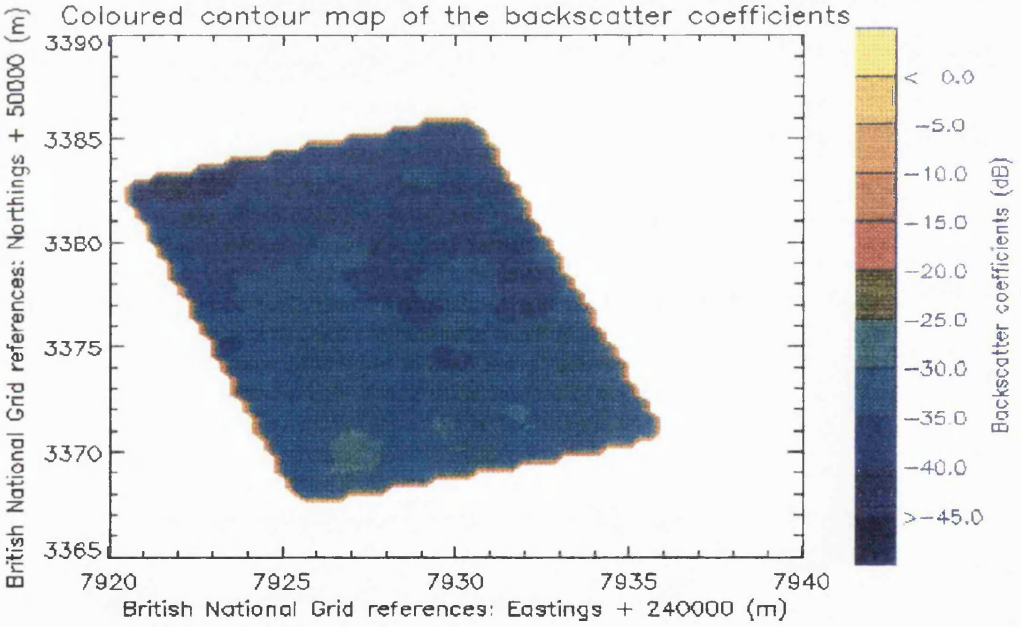

Figure 7.7: Contoured plot of Backscatter Coefficients. Seabed type: Mud.

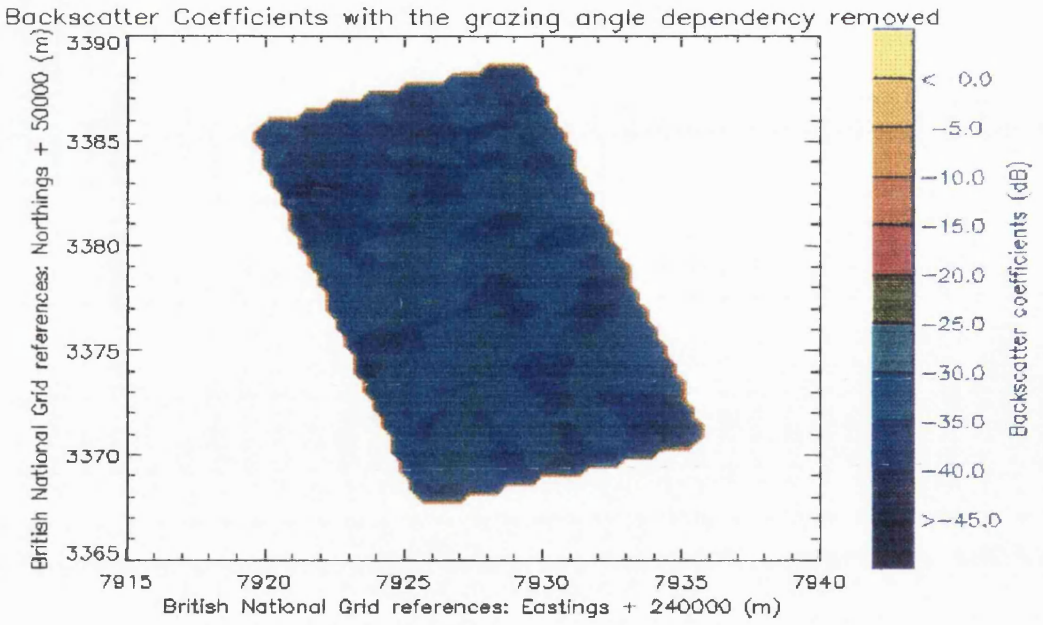

Figure 7.8: Contour plot of Backscatter Coefficients with the grazing angle dependency removed. The backscatter values are relative to a grazing angle of 25 degrees. Seabed type: Mud.

7.3.2 Plots covering all of Track 1 data

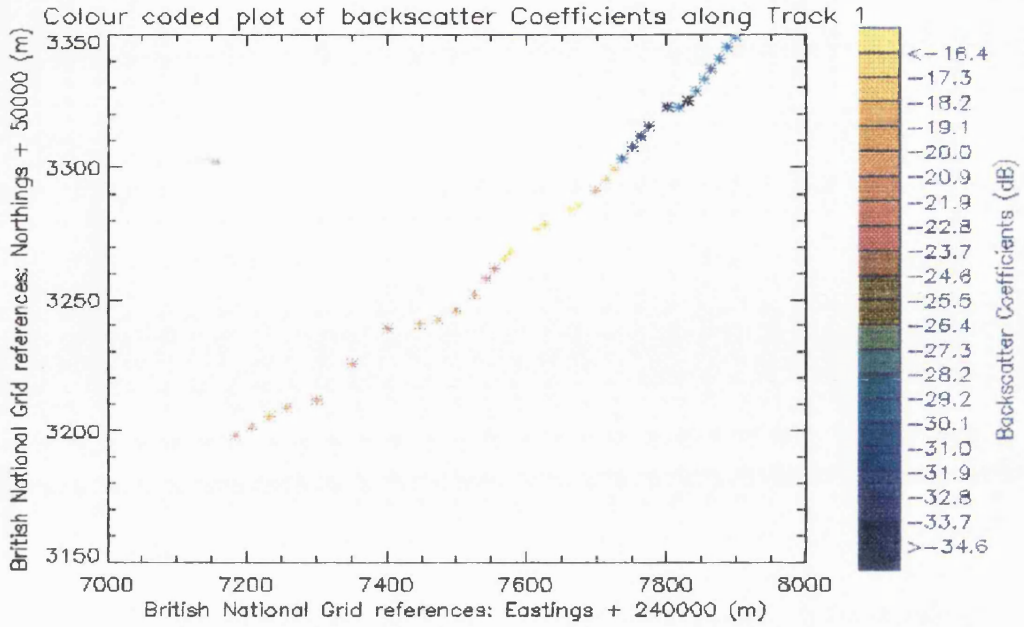

Figure 7.9: Colour coded plot of the backscatter coefficients along Track 1. Each point represents the average backscatter value over all grazing angles for 10 pings.

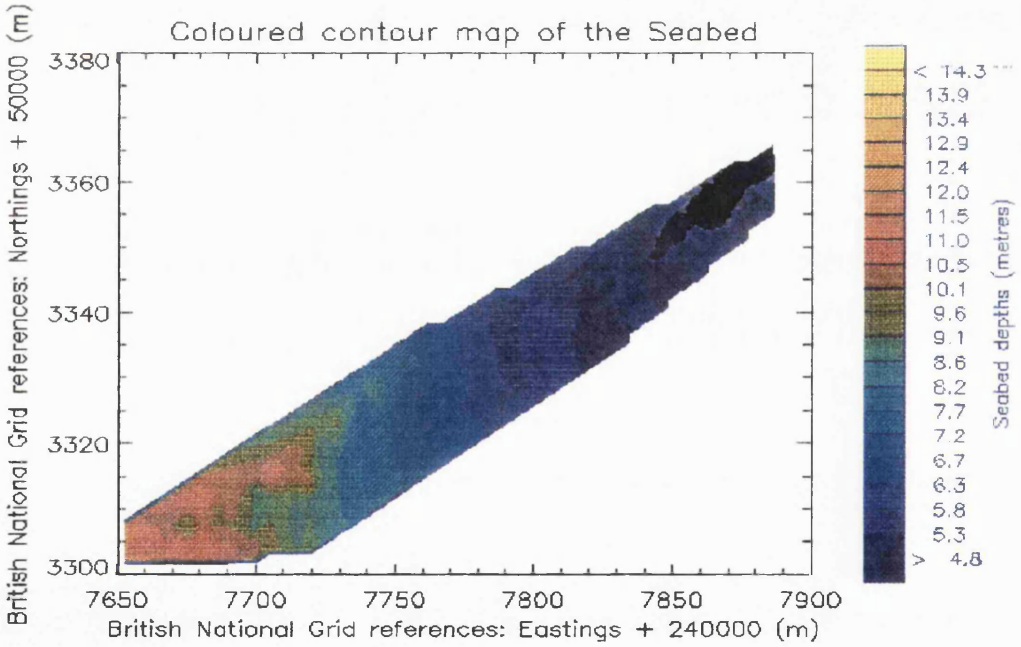

Figure 7.10: Contour plot of the seabed bathymetry for Track 1.

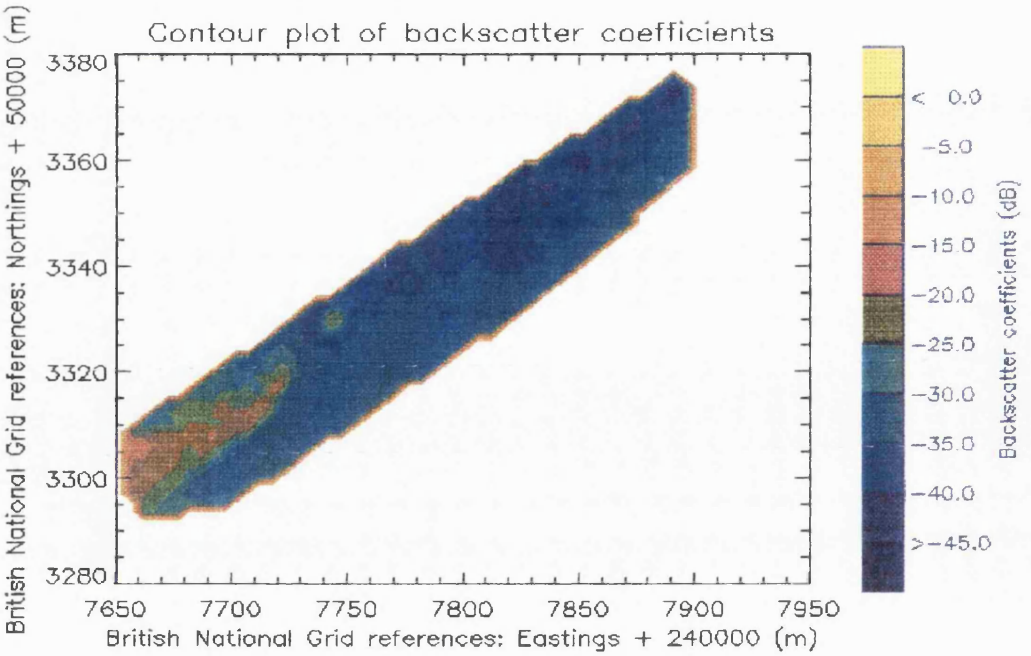

Figure 7.11: Contour plot of the backscatter coefficients along Track 1, this was achieved by using a sliding window technique.

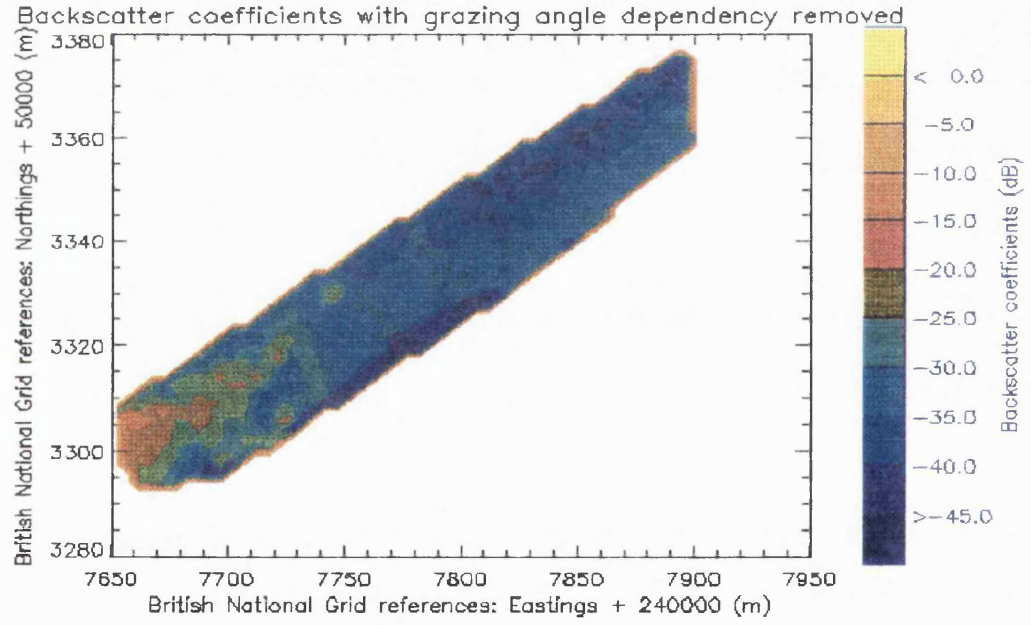

Figure 7.12: Contour plot of the backscatter coefficients with the grazing angle dependency removed. These backscatter coefficient values are relative to the backscatter coefficient value at the middle grazing angle.

7.4 117kHz dataset - Overview of Track 2

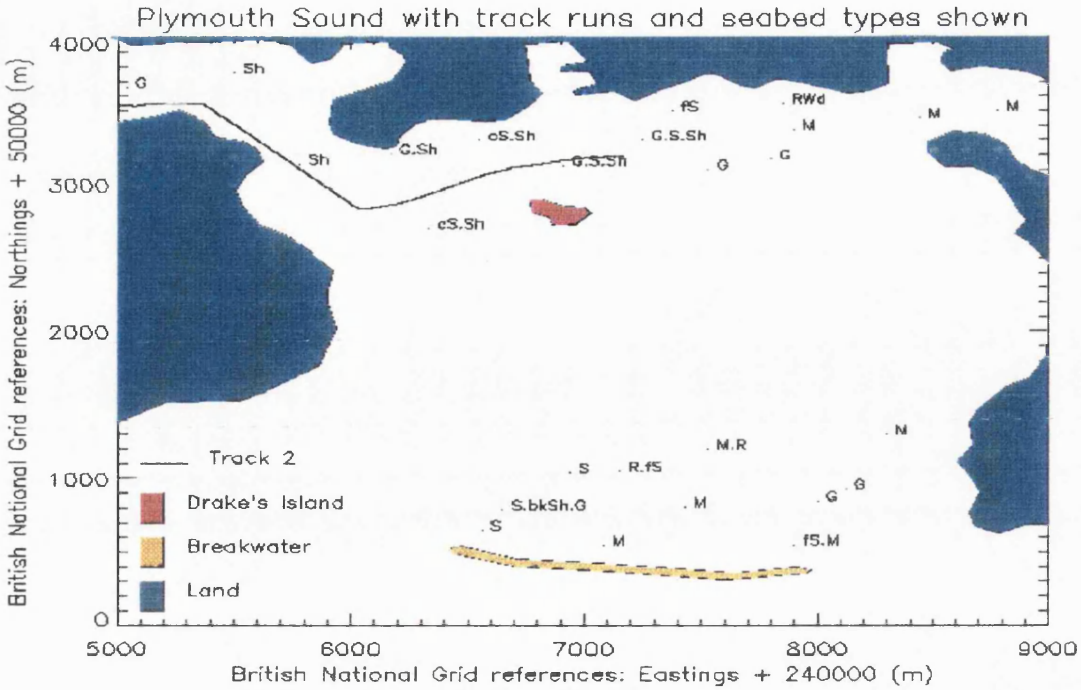

Figure 7.13: Schematic of Plymouth Sound, with the seabed types and Track 2 overlaid. For key to symbols , see section 7.2.1.

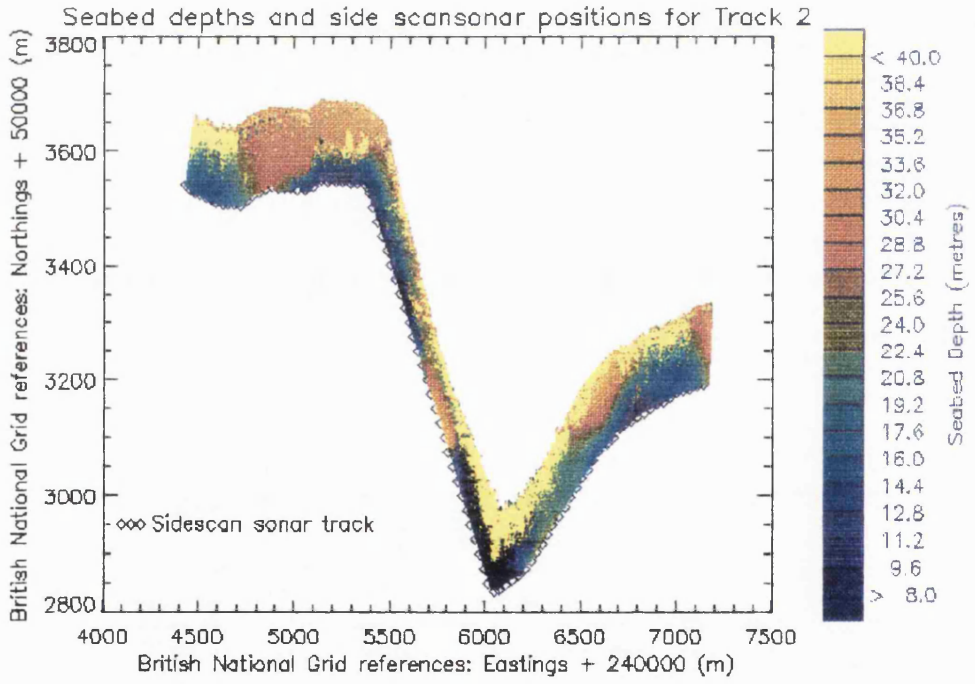

Figure 7.14: A plot of the seabed depths with the sidescan sonar positions overlaid

7.4.1 Results for seabed type: Gravel

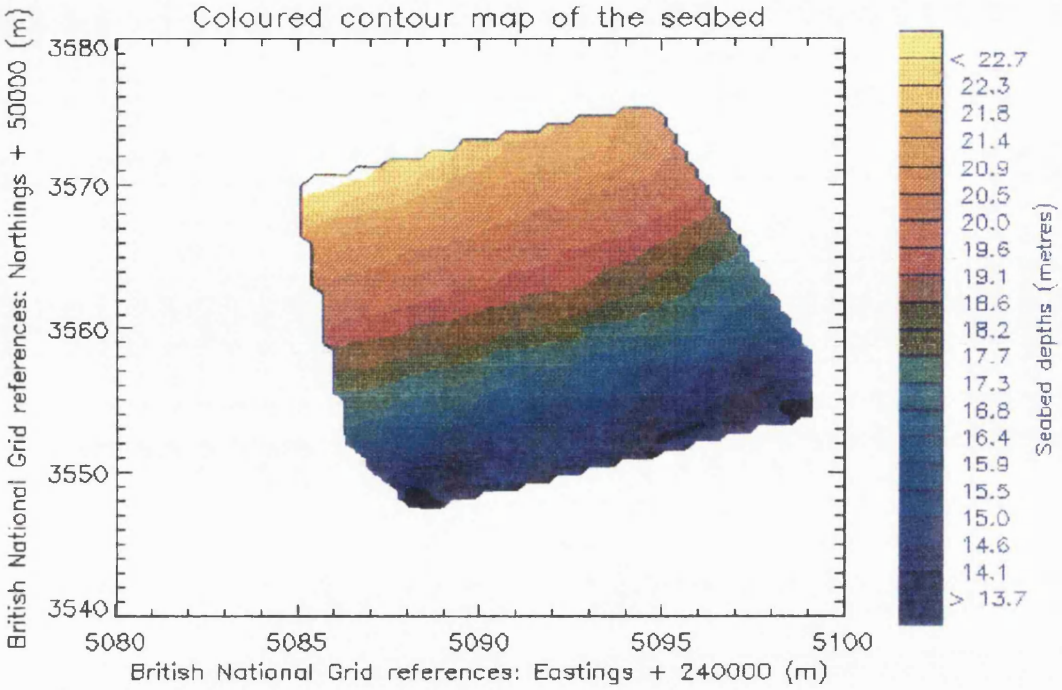

Figure 7.15: Contoured plot of seabed under investigation. Seabed type: Gravel.

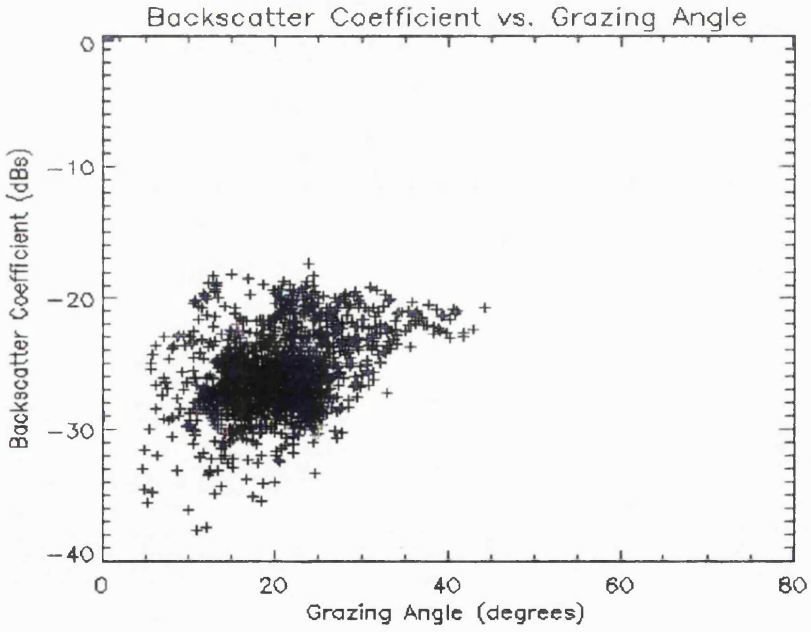

Figure 7.16: A plot of Backscatter Coefficients against Grazing Angle. Seabed type: Gravel.

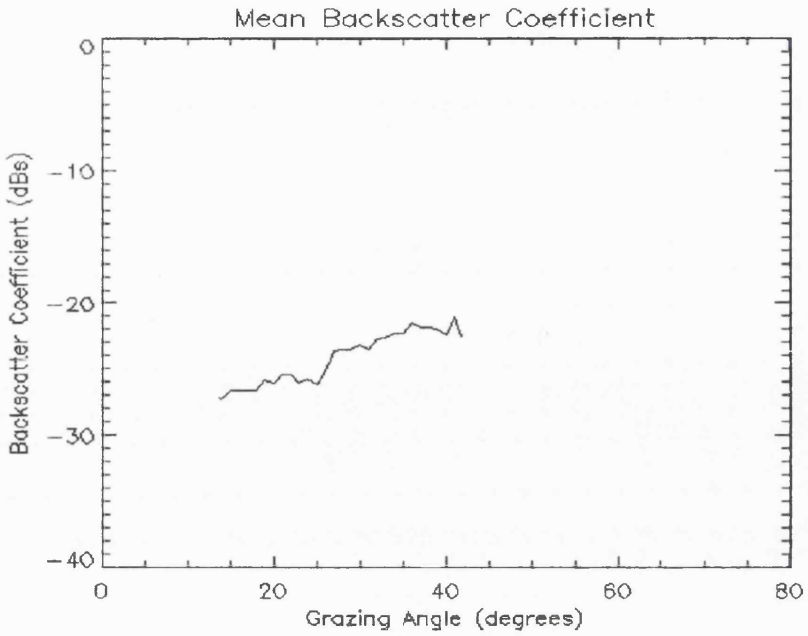

Figure 7.17: A plot of Mean Backscatter Coefficients against Grazing Angle. Seabed type: Gravel.

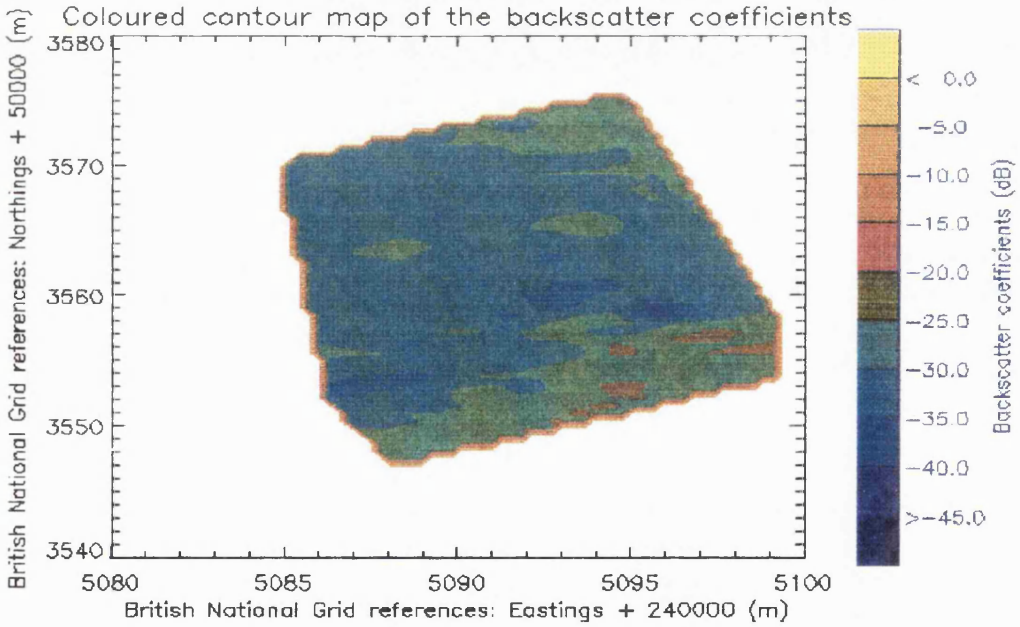

Figure 7.18: Contoured plot of Backscatter Coefficients. Seabed type: Gravel

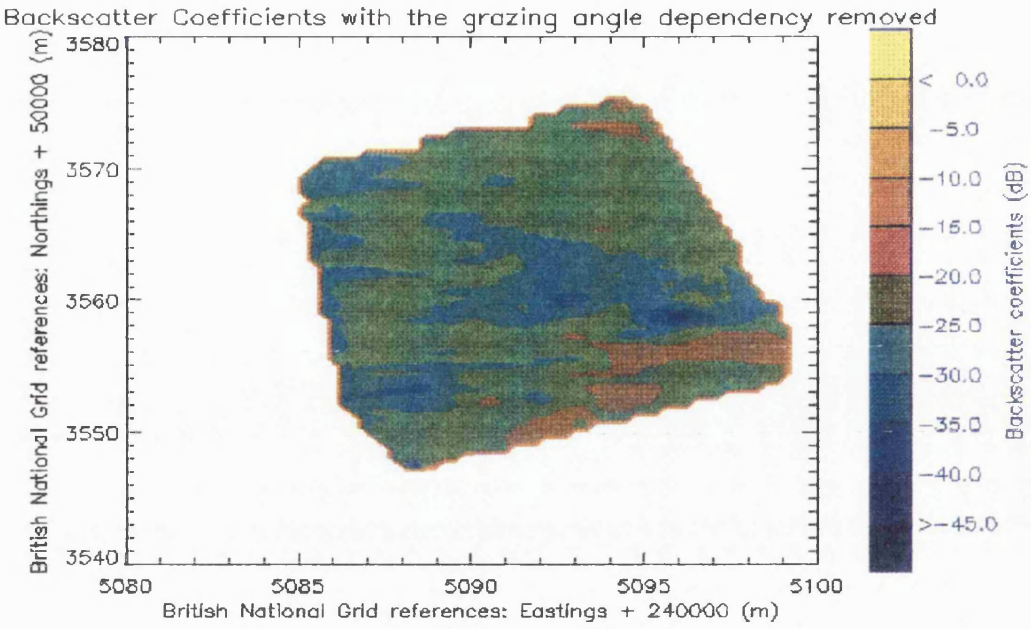

Figure 7.19: Contoured plot of Backscatter Coefficients with the grazing angle dependency removed. The backscatter values are relative to a grazing angle of 28 degrees. Seabed type: Gravel.

7.4.2 Results for seabed type: Shells

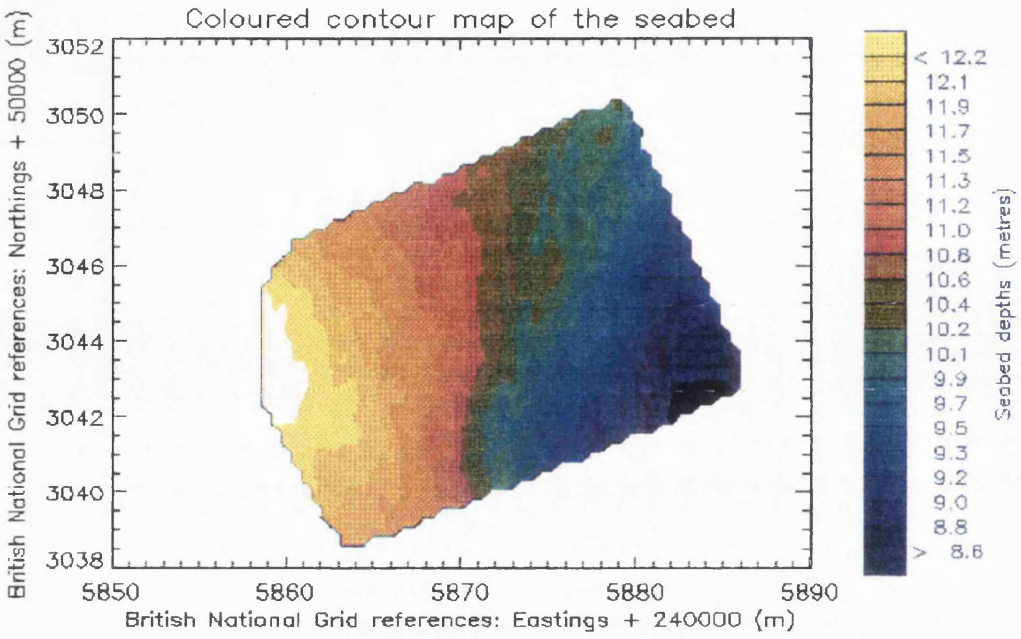

Figure 7.20: Contoured plot of seabed under investigation. Seabed type: Shells

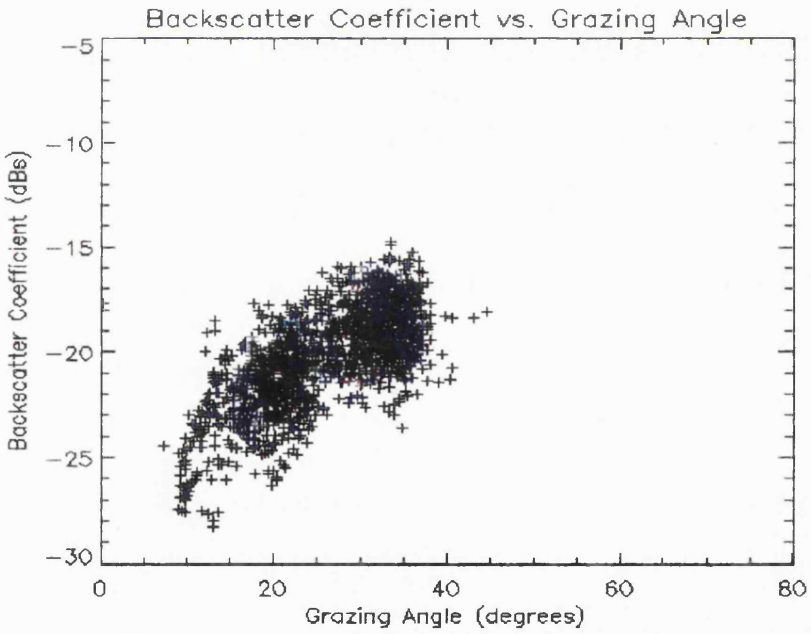

Figure 7.21: A plot of Backscatter Coefficients against Grazing Angle. Seabed type: Shells

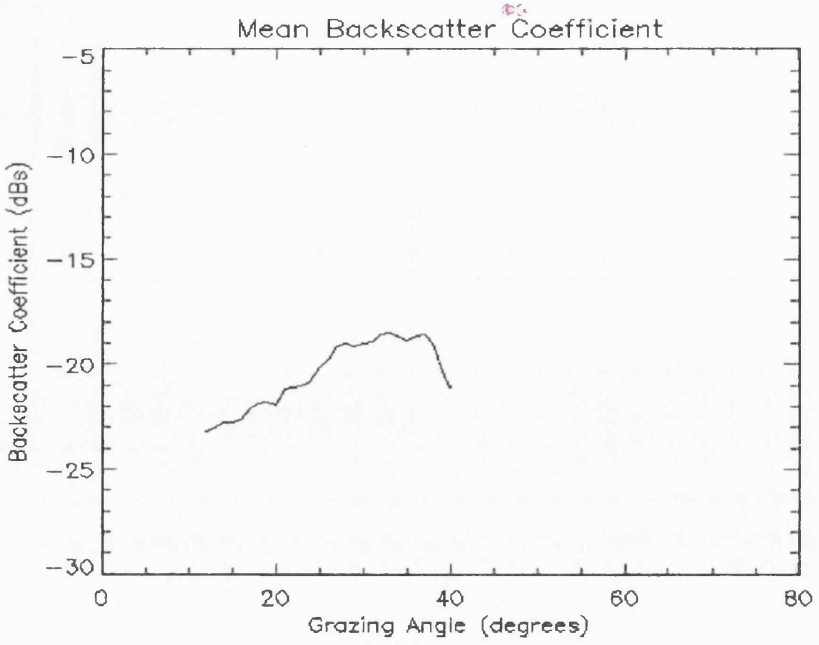

Figure 7.22: A plot of Mean Backscatter Coefficients against Grazing Angle. Seabed type: Shells

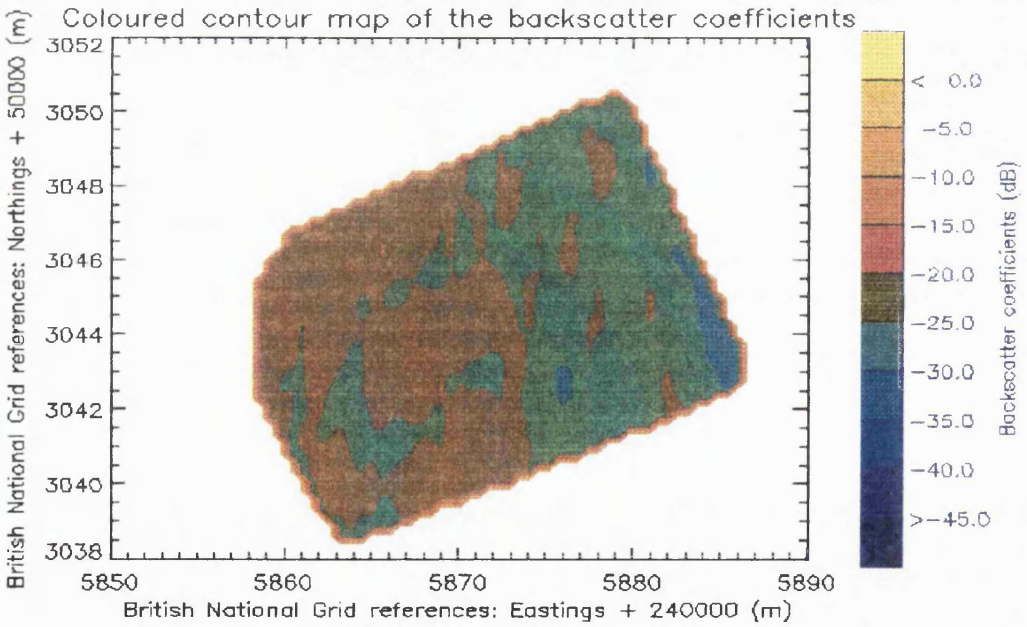

Figure 7.23: Contoured plot of the backscatter Coefficients. Seabed type: Shells

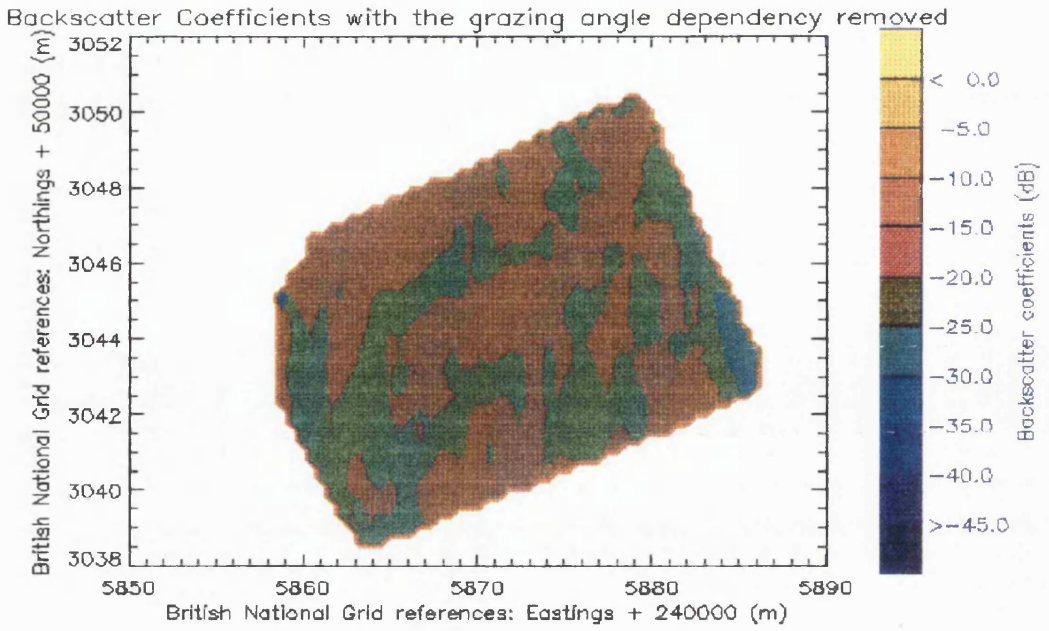

Figure 7.24: Contoured plot of the Backscatter Coefficients with the grazing angle dependency removed. The backscatter values are relative to a grazng angle of 26 degrees. Seabed type: Shells.

7.4.3 Results for seabed type: Gravel/Shells/Sand

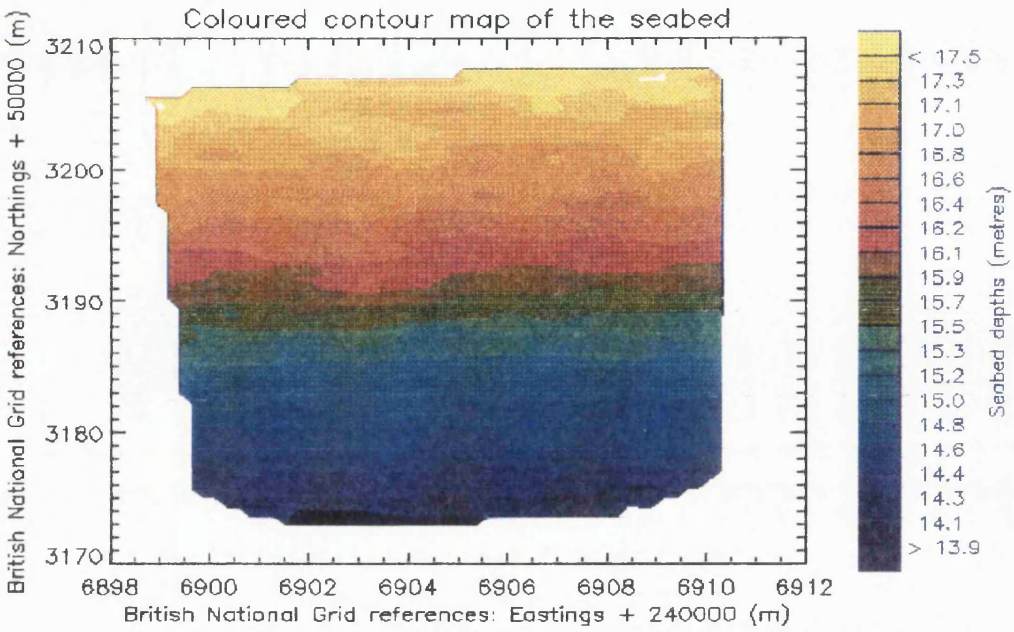

Figure 7.25: Contoured plot of the seabed under investigation. Seabed type: Gravel/Shells/Sand

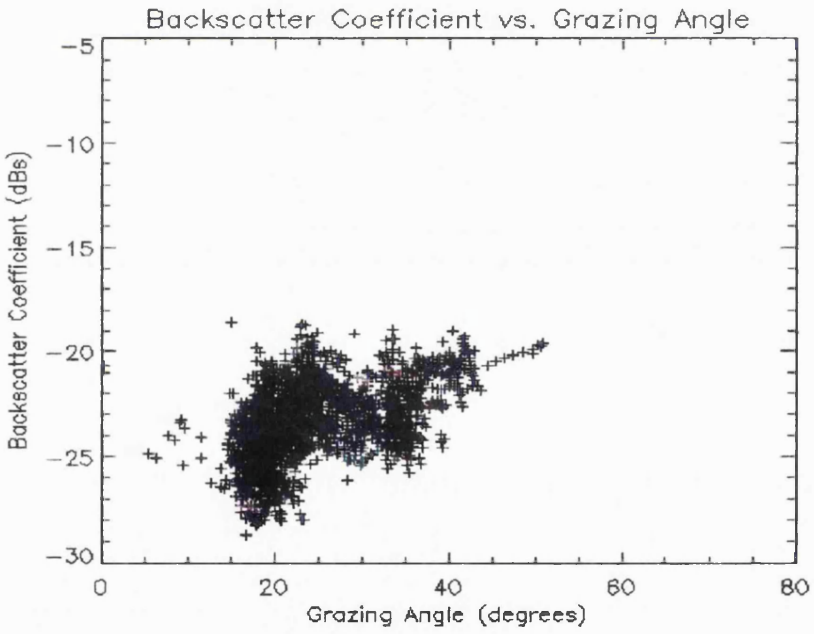

Figure 7.26: A plot of Backscatter Coefficients against Grazing Angle. Seabed type: Gravel/Shells/Sand

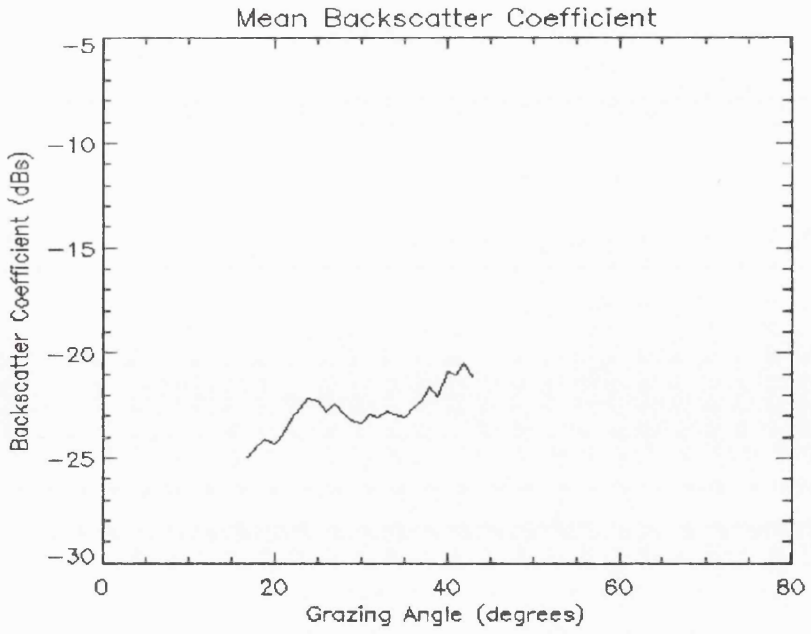

Figure 7.27: A plot of Mean Backscatter Coefficients against Grazing Angle. Seabed type: Gravel/Shells/Sand

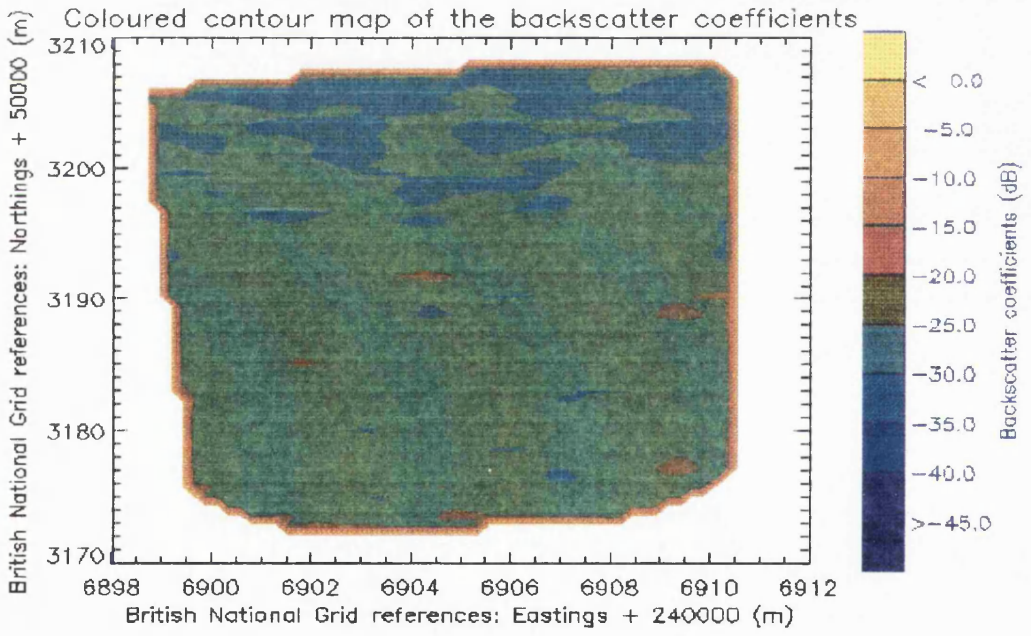

Figure 7.28: Contoured plot of the Backscatter Coefficients. Seabed type: Gravel/Shells/Sand

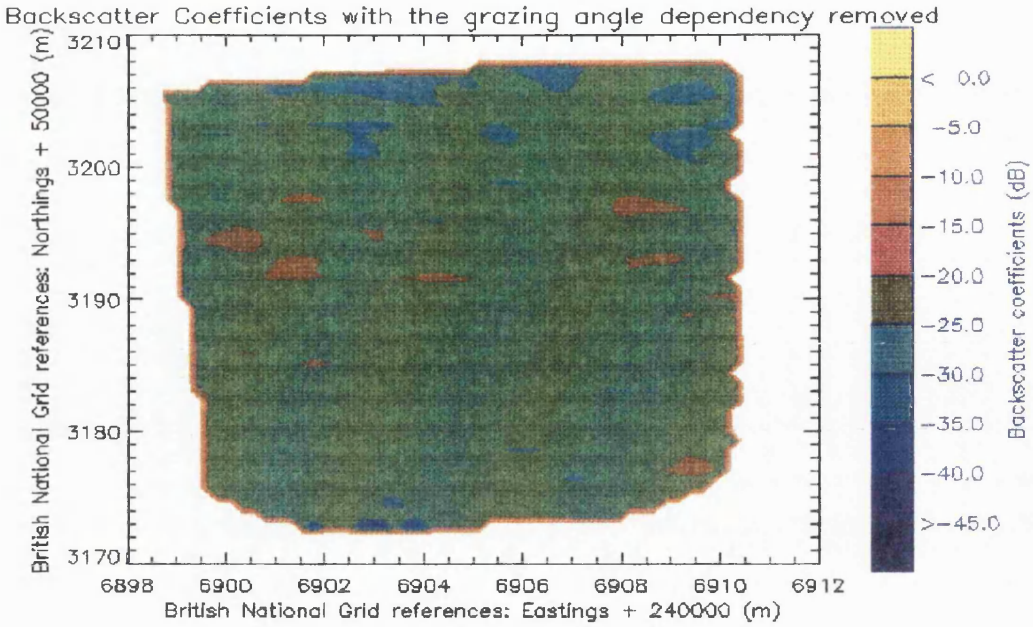

Figure 7.29: Contoured plot of the Backscatter Coefficients with the grazing angle dependency removed. The backscatter values are relative to a grazing angle of 30 degrees. Seabed type: Gravel/Shells/Sand.

7.5 234 kHz dataset - Overview of Track 3

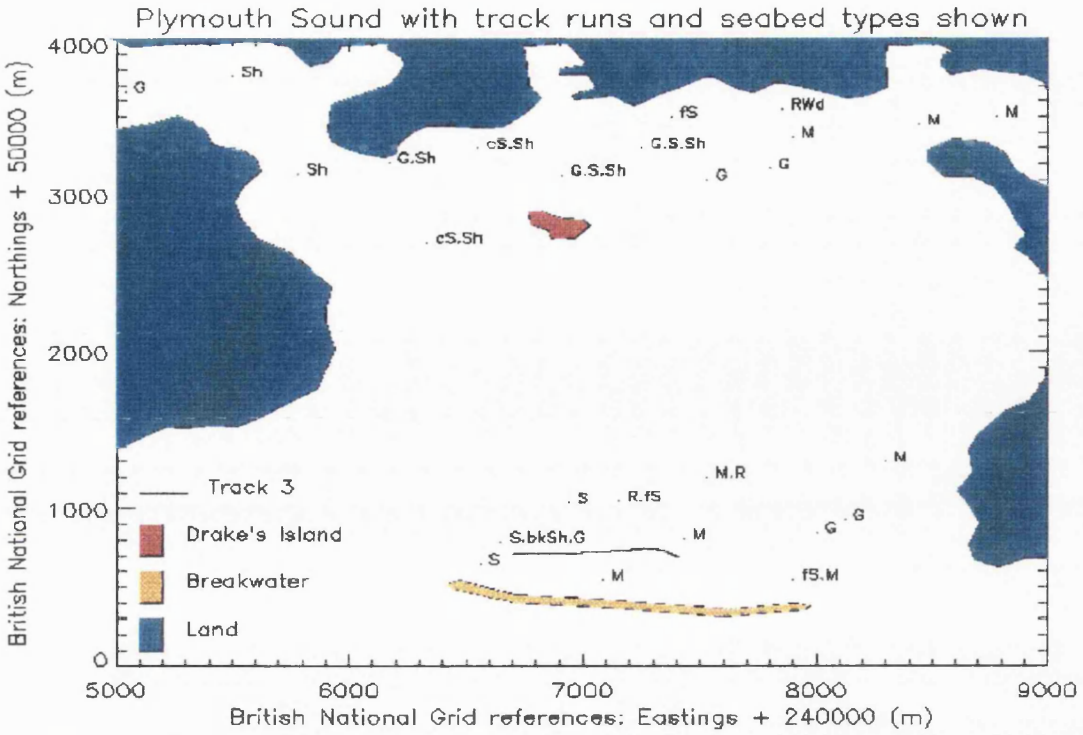

Figure 7.30: Schematic of Plymouth Sound, with seabed types and Track 3 overlaid. For key to symbols see section 7.2.1.

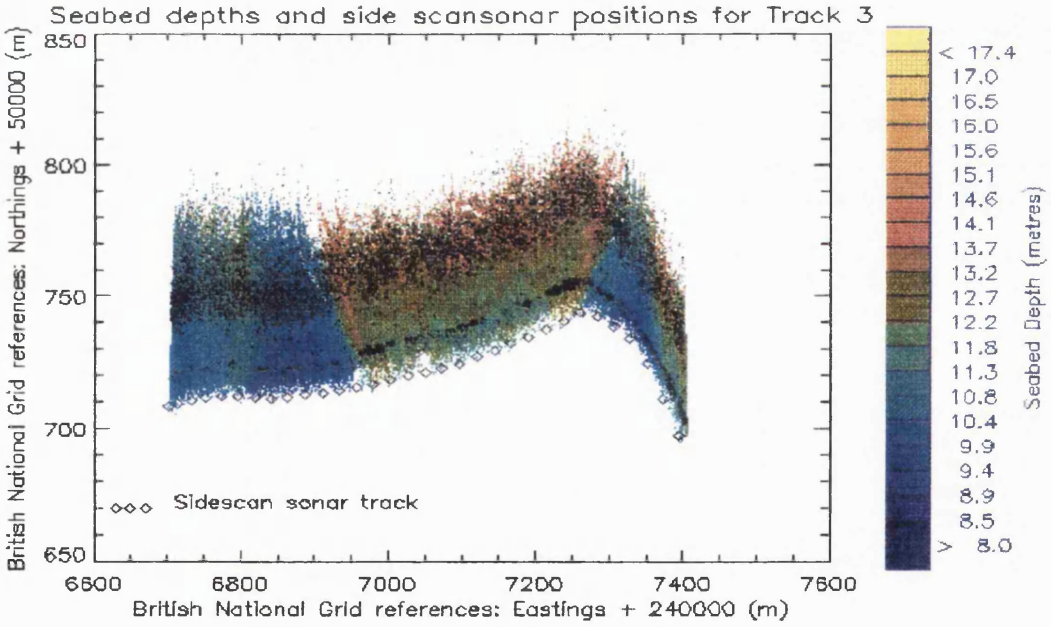

Figure 7.31: A plot of seabed depths with sidescan sonar positions overlaid.

7.5.1 Plots covering all of Track 3 data

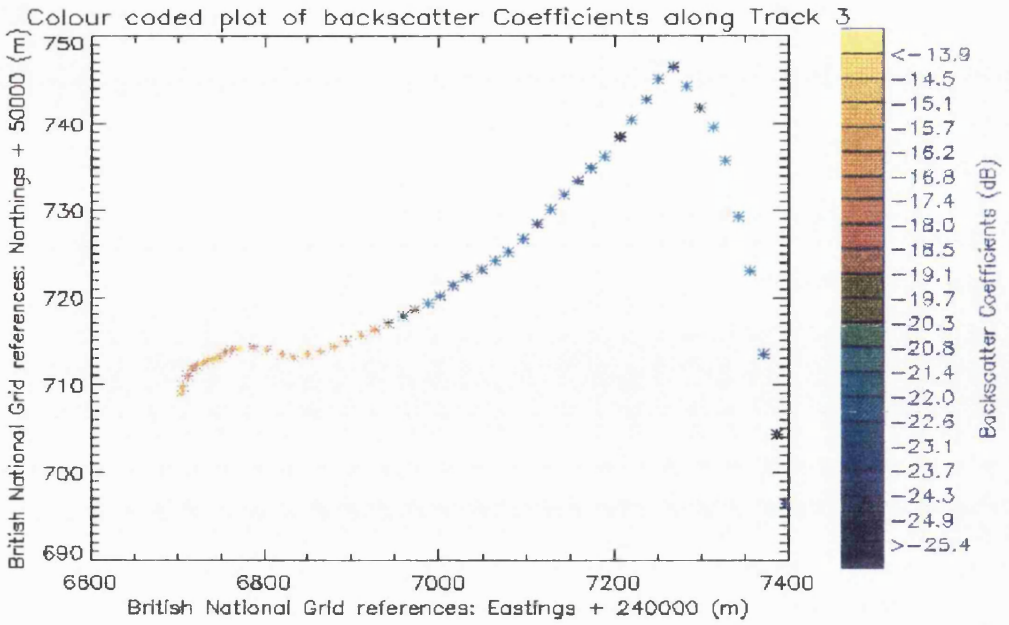

Figure 7.32: Colour coded plot of Backscatter coefficient values along Track 3. Each point represents the average backscatter value over all grazing angles for 10 pings.

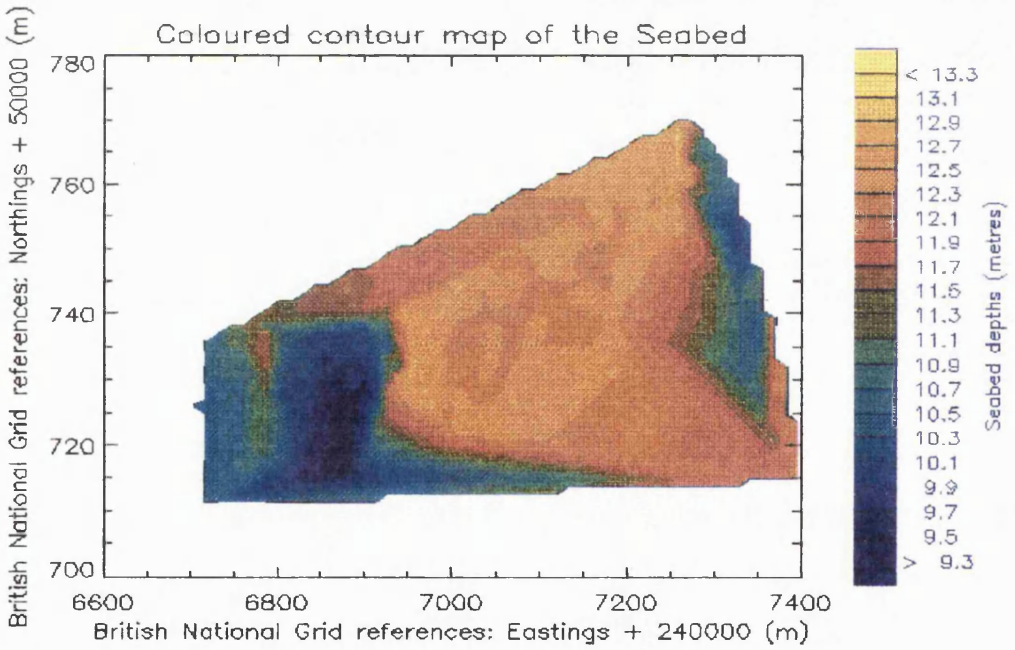

Figure 7.33: Contoured plot of the seabed bathymetry for all of Track 3.

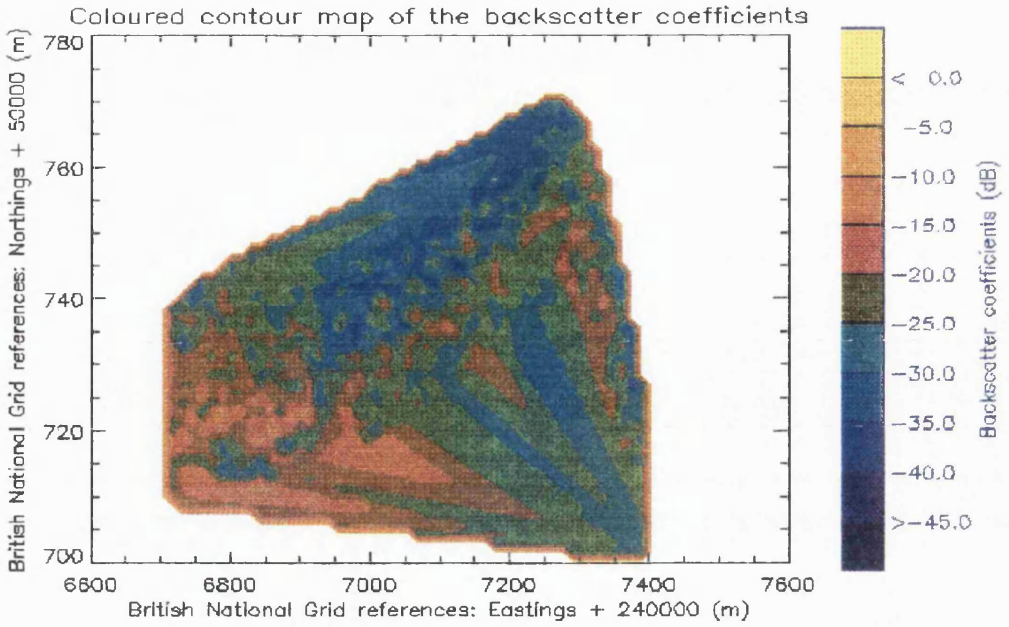

Figure 7.34: Contoured plot of Backscatter Coefficients along Track 3, this was achieved by using a sliding window technique.

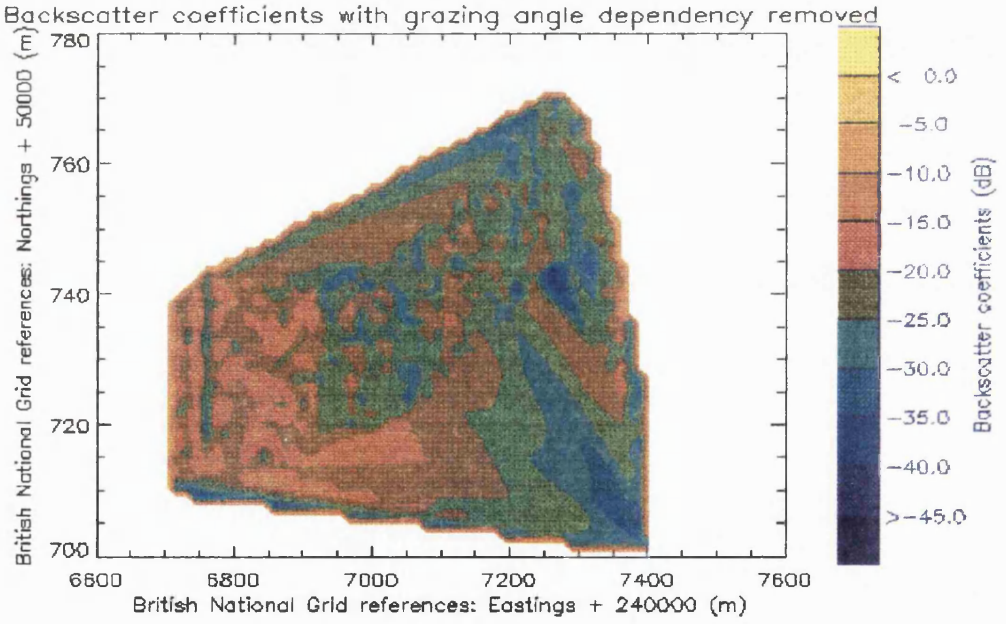

Figure 7.35: Contour plot of the backscatter coefficients with the angle dependency removed. These backscatter coefficient values are relative to the backscatter coefficient value at the middle grazing angle.

7.6 234 kHz dataset - Overview of Track 4

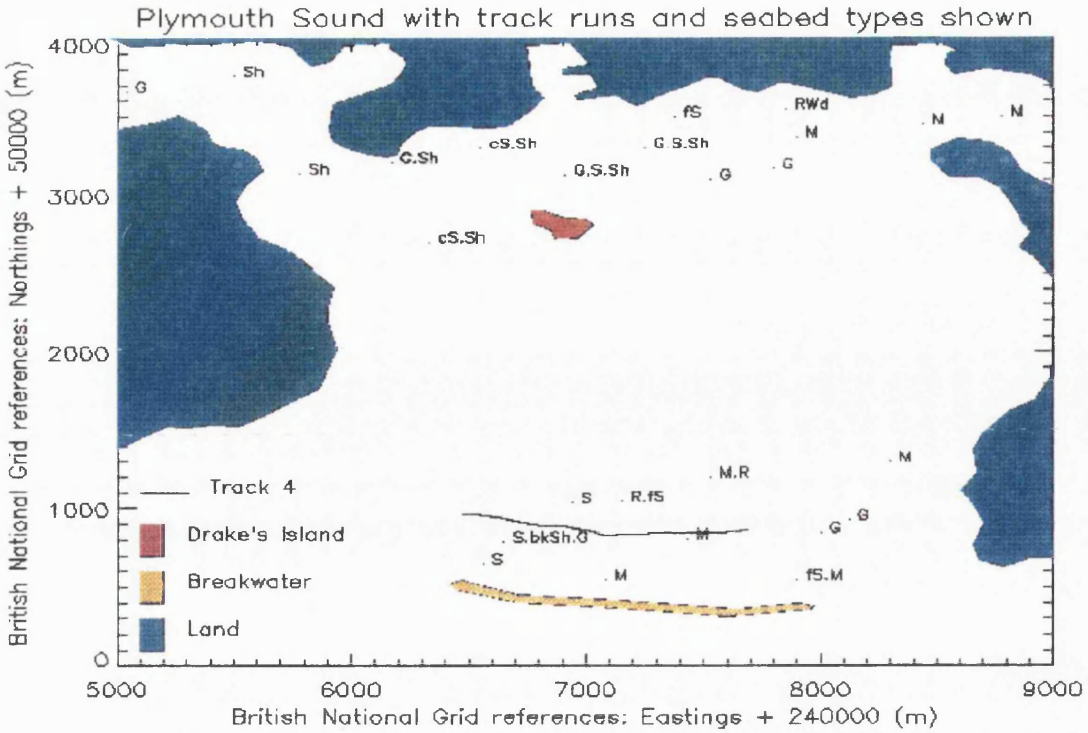

Figure 7.36: Schematic of Plymouth Sound, with seabed types and track 4 overlaid. For key to seabed symbols see section 7.2.1.

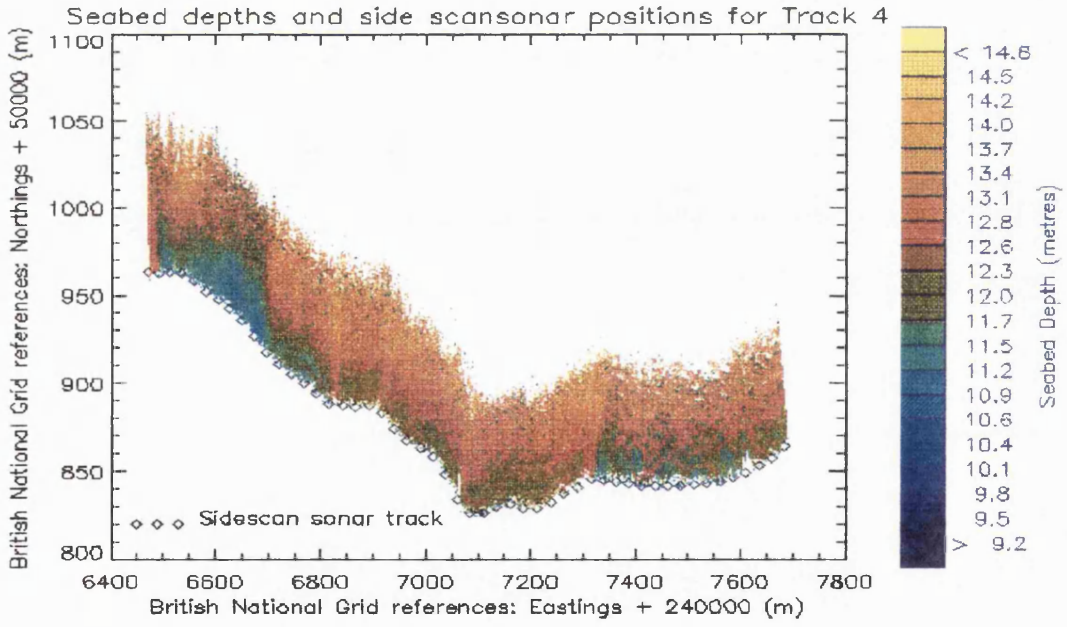

Figure 7.37: A plot of seabed depths with sidescan sonar positions overlaid.

7.6.1 Results for seabed type: Sand/broken Shells/Gravel

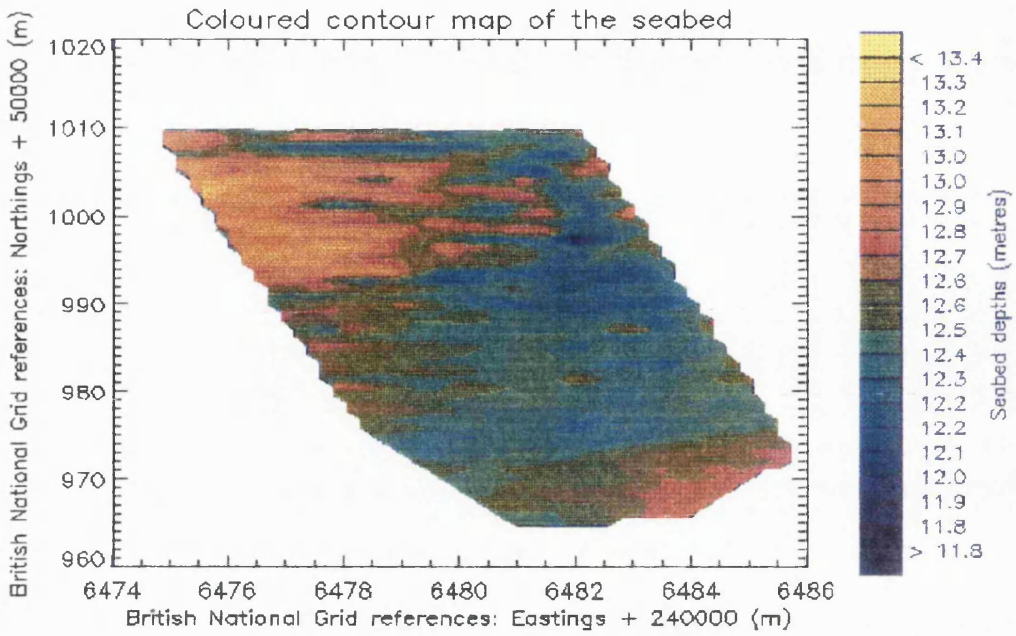

Figure 7.38: Contour plot of seabed under investigation. Seabed type: Sand/Broken Shell/Gravel.

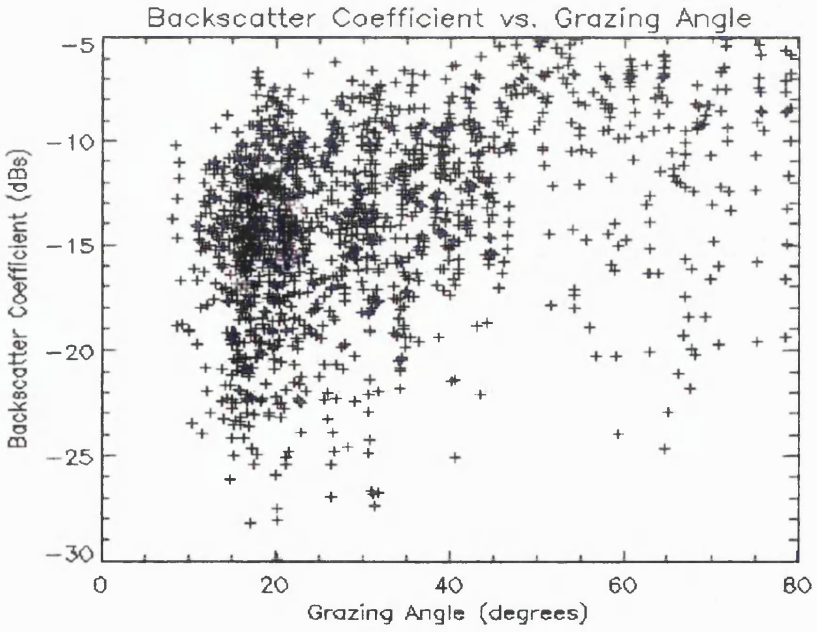

Figure 7.39: A plot of Backscatter Coefficients against Grazing Angle. Seabed type: Sand/broken Shells/Gravel.

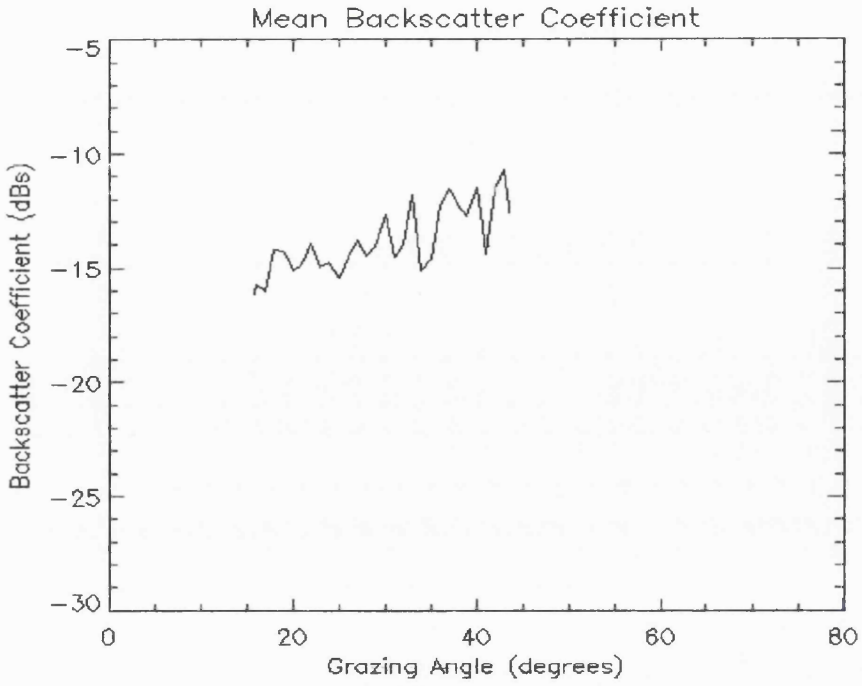

Figure 7.40: A plot of Mean Backscatter Coefficient against Grazing Angle. Seabed type: Sang/broken Shells/Gravel.

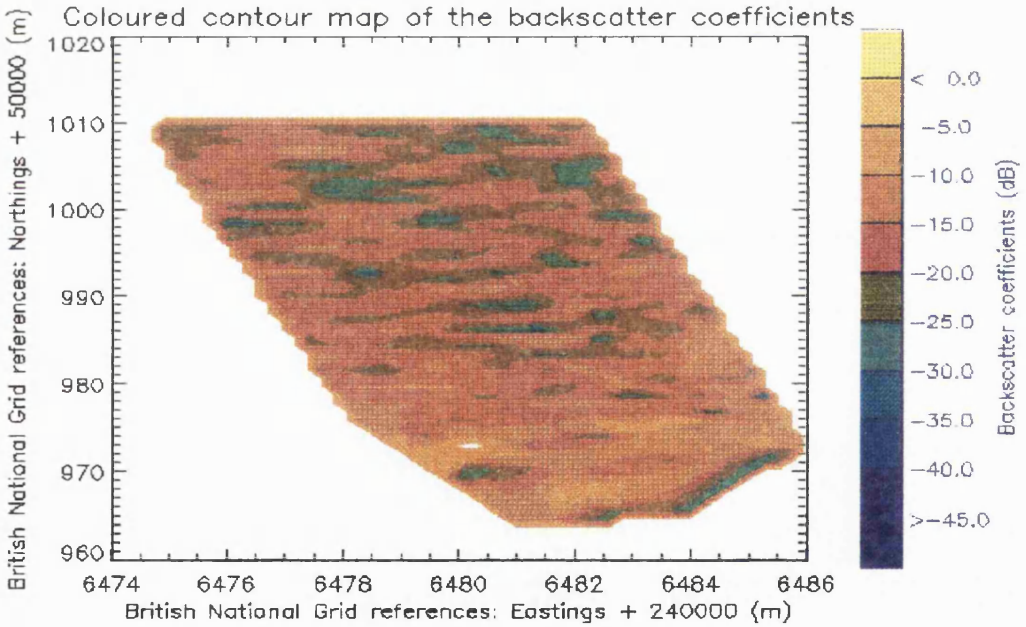

Figure 7.41: Contoured plot of Backscatter Coefficients. Seabed type: Sand/broken Shells/Gravel.

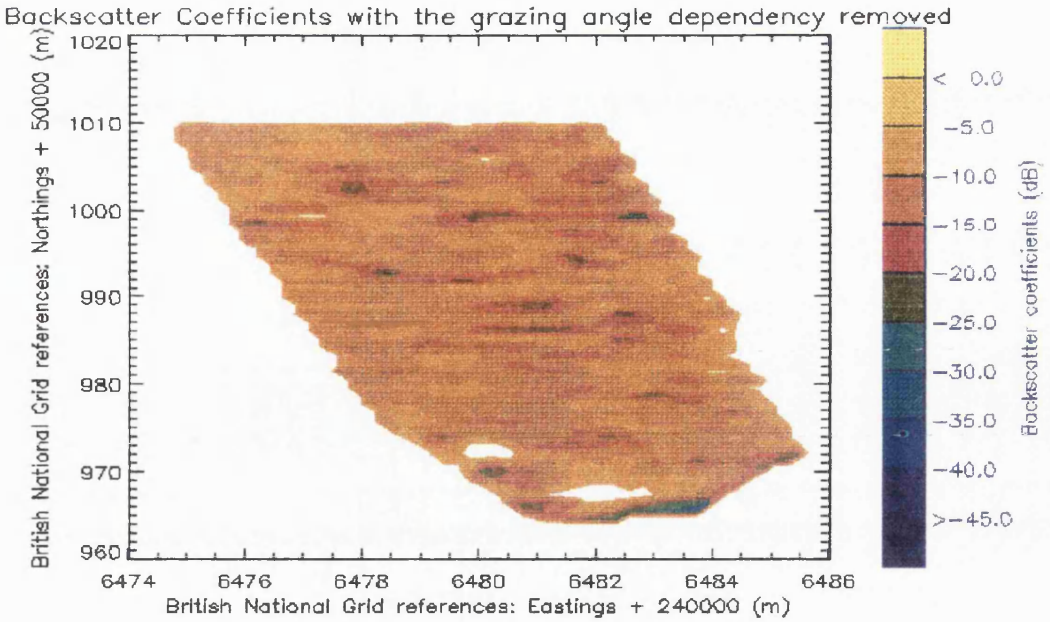

Figure 7.42: Contoured plot of the Backscatter Coefficients with the grazing angle dependency removed. The backscatter values are relative to a grazing angle of 29 degrees. Seabed type: Sand/broken Shells/Gravel.

7.6.2 Results for seabed type: Mud

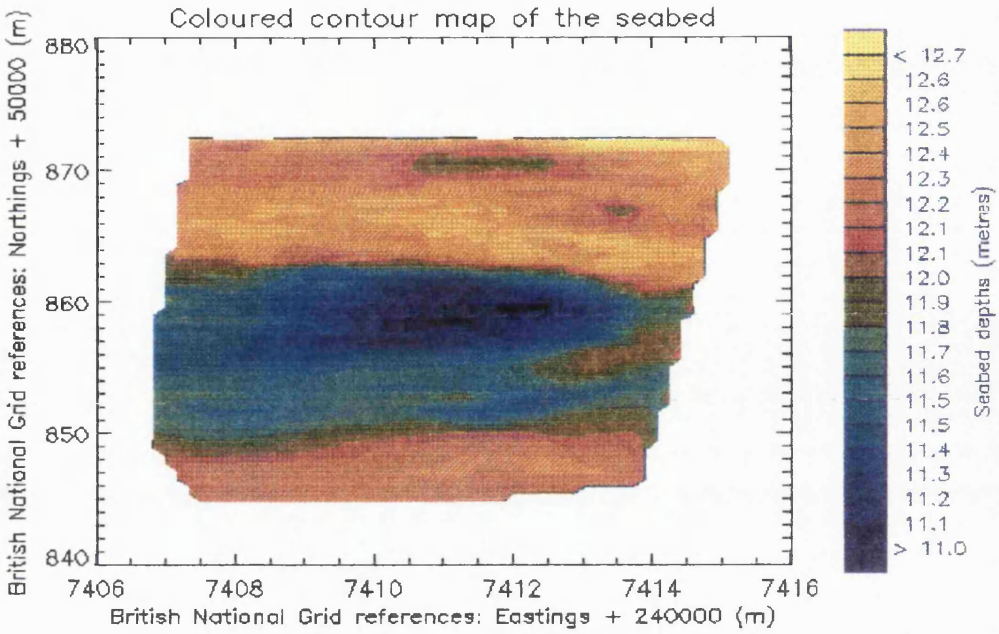

Figure 7.43: Contour plot of seabed under investigation. Seabed type: Mud.

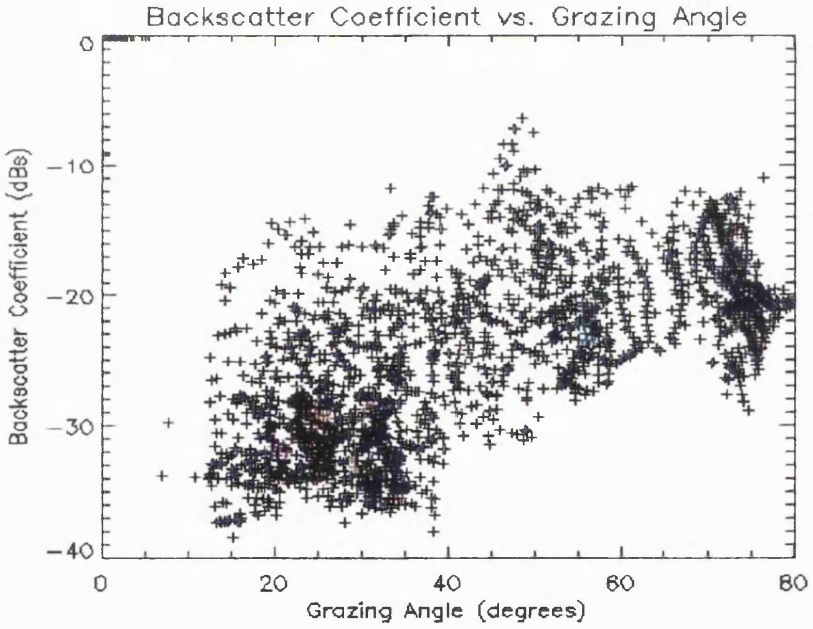

Figure 7.44: A plot of Backscatter Coefficients against Grazing Angle. Seabed type: Mud.

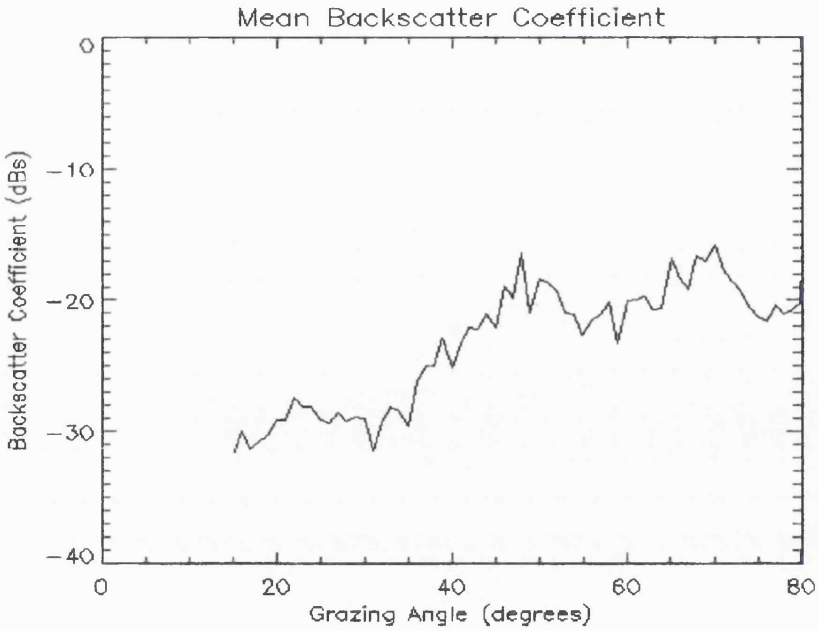

Figure 7.45: A plot of Mean Backscatter Coefficients against Grazing Angle. Seabed type: Mud.

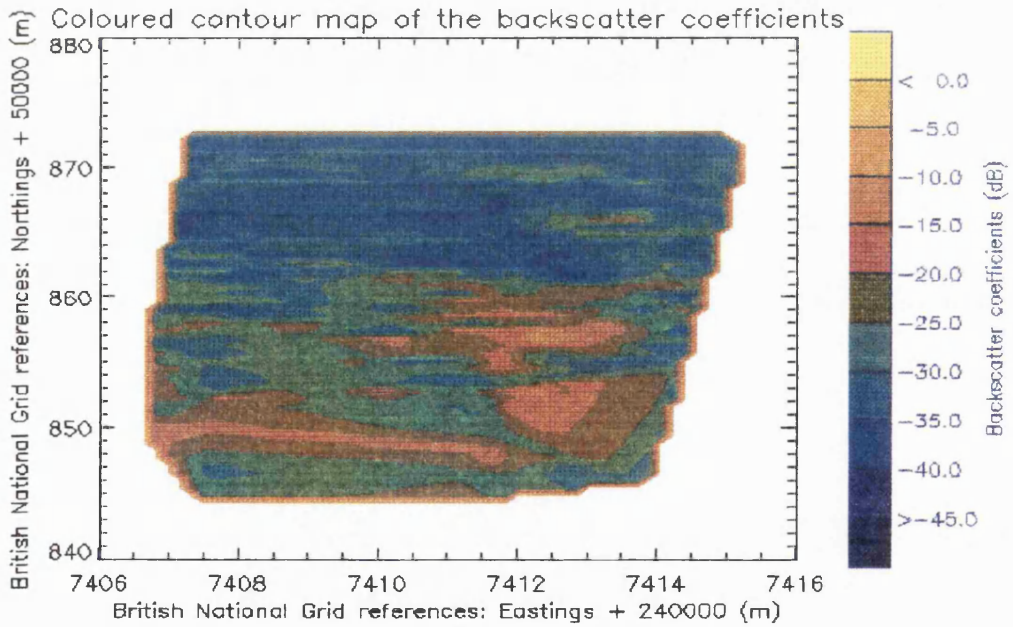

Figure 7.46: Contoured plot of Backscatter Coefficients. Seabed type: Mud.

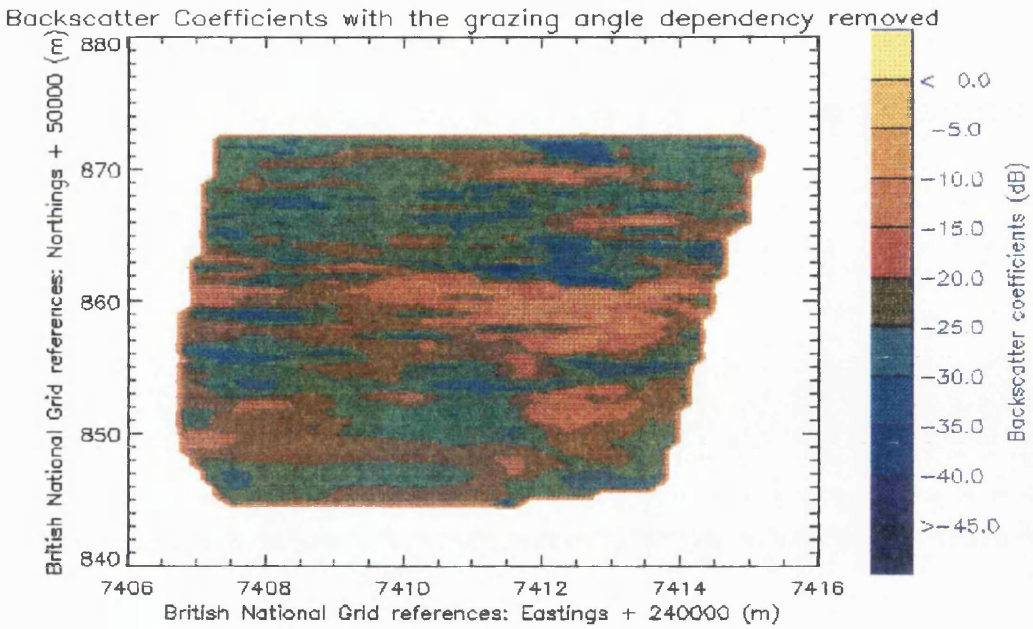

Figure 7.47: Contoured plot of the Backscatter Coefficients with the grazing angle dependency removed. The backscatter values are relative to a grazing angle of 47 degrees. Seabed type: Mud.

7.6.3 Plots covering all of Track 4 data.

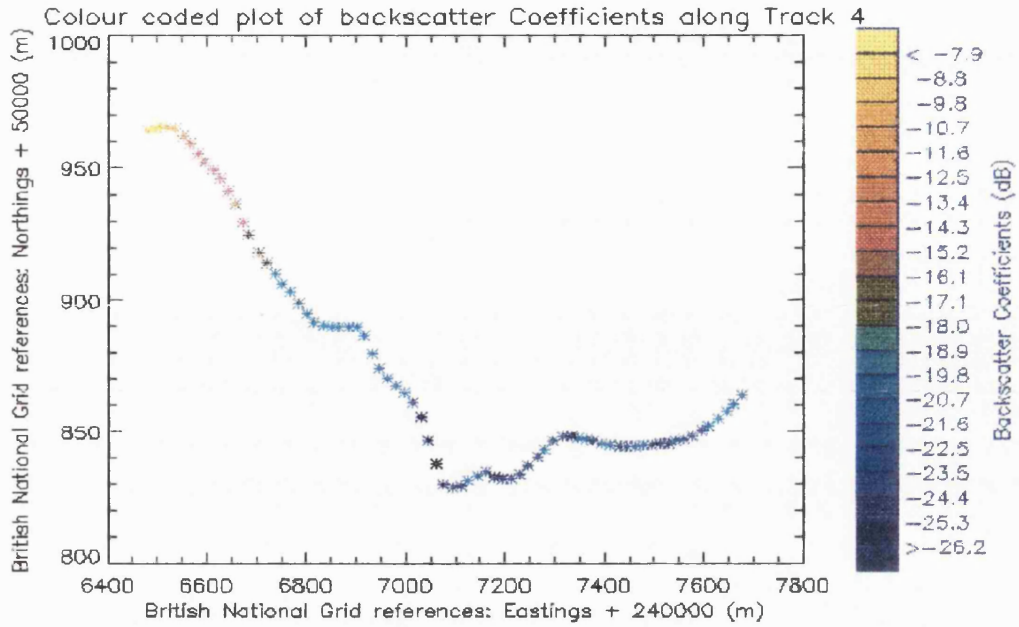

Figure 7.48: Colour coded plot of backscatter coefficient values along Track 4. Each point represents the average backscatter value over all grazing angles for 10 pings.

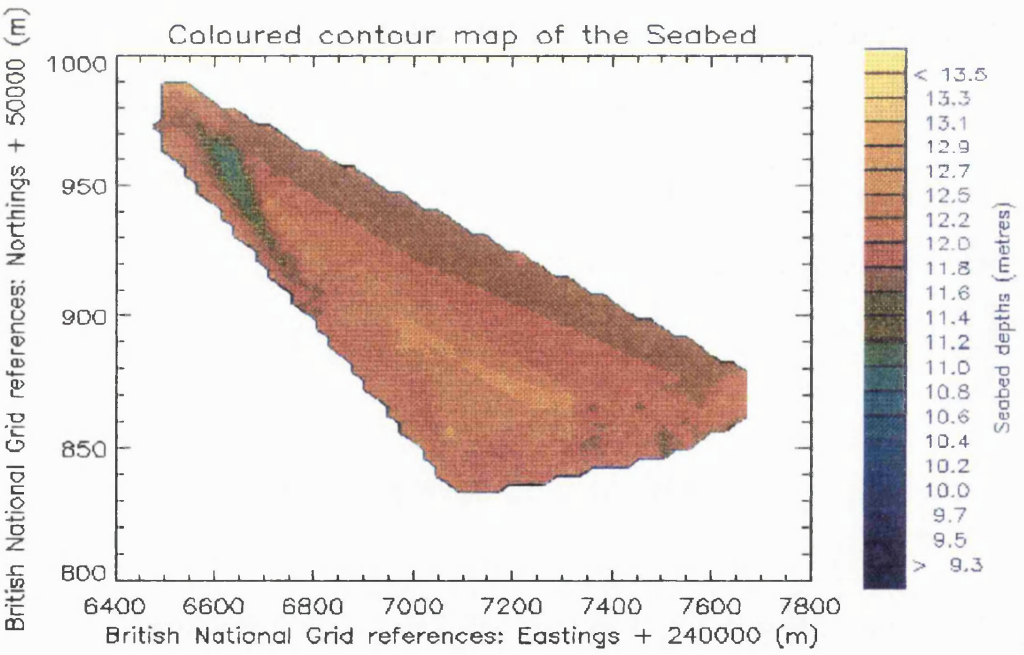

Figure 7.49: Contoured plot of the seabed bathymetry for all of Track 4.

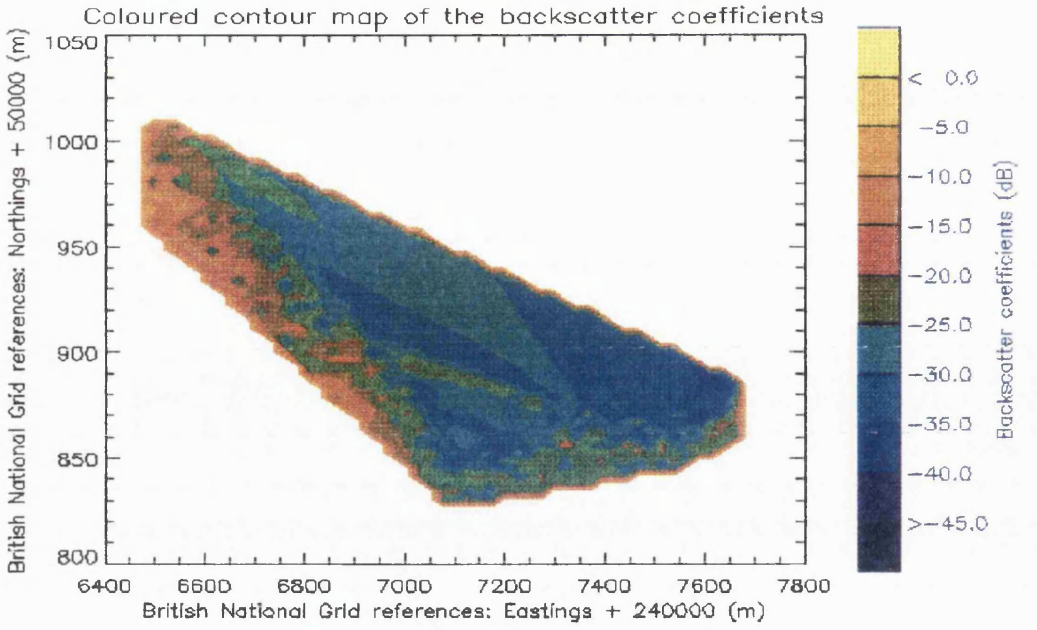

Figure 7.50: Contoured plot of the Backscatter Coefficients along Track 4, this was achieved by using a sliding window technique.

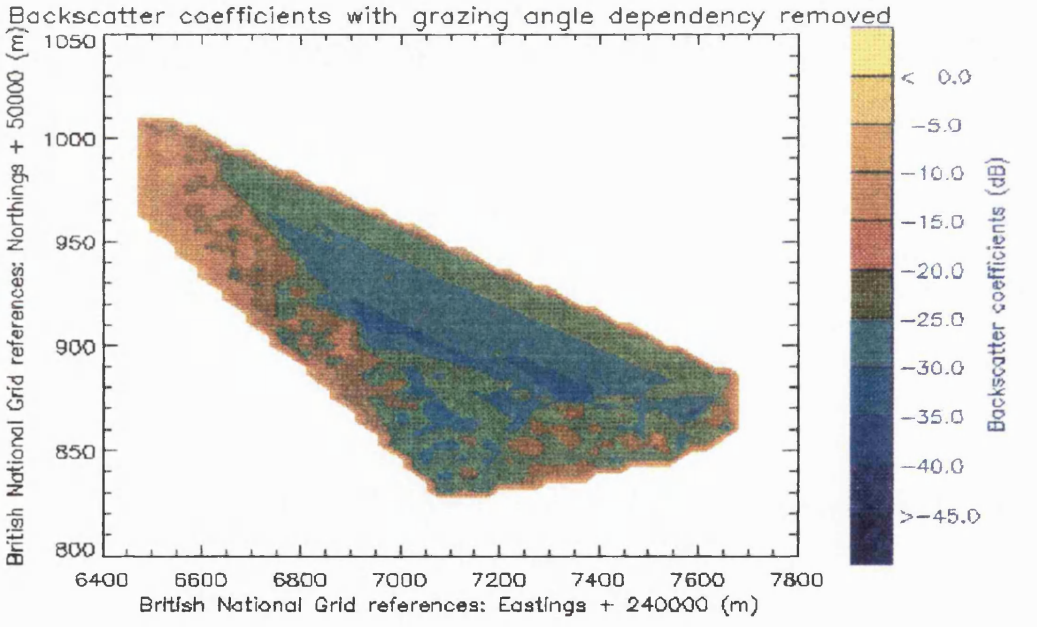

Figure 7.51: Contour plot of the Backscatter Coefficients with the grazing angle dependency removed. These backscatter values are relative to the backscatter coefficient value at the middle grazing angle.

7.7 234 kHz dataset - Overview of Track 5

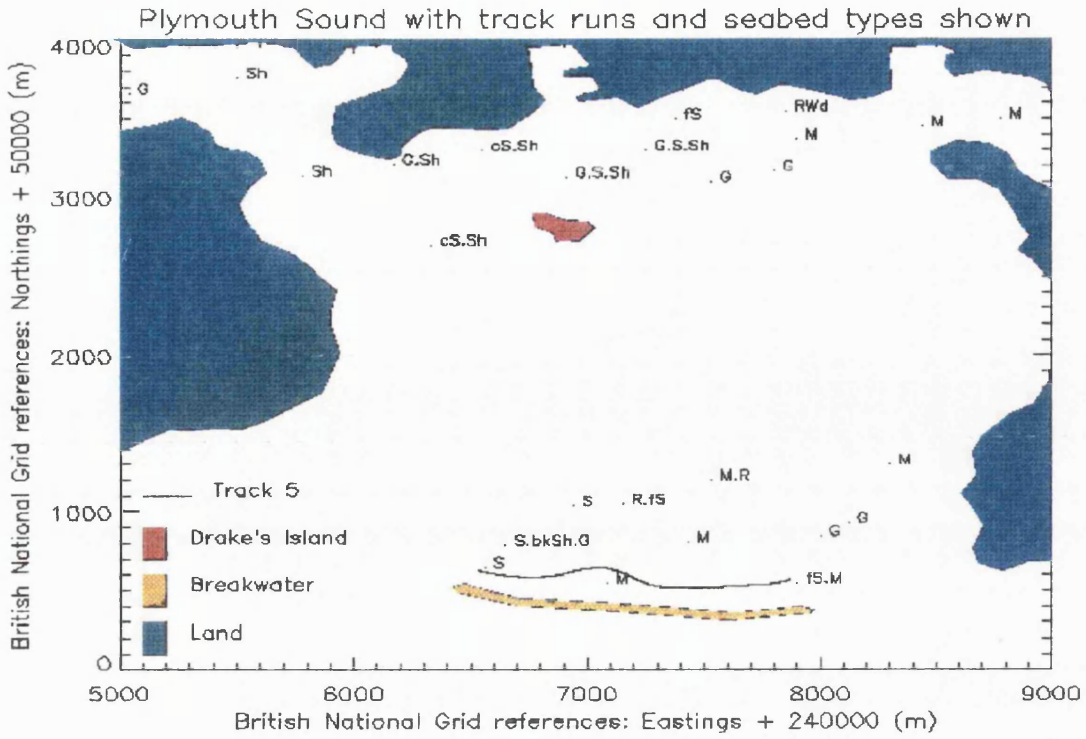

Figure 7.52: Schematic of Plymouth Sound, with seabed types and Track 5 overlaid. For key to seabed symbols see section 7.2.1.

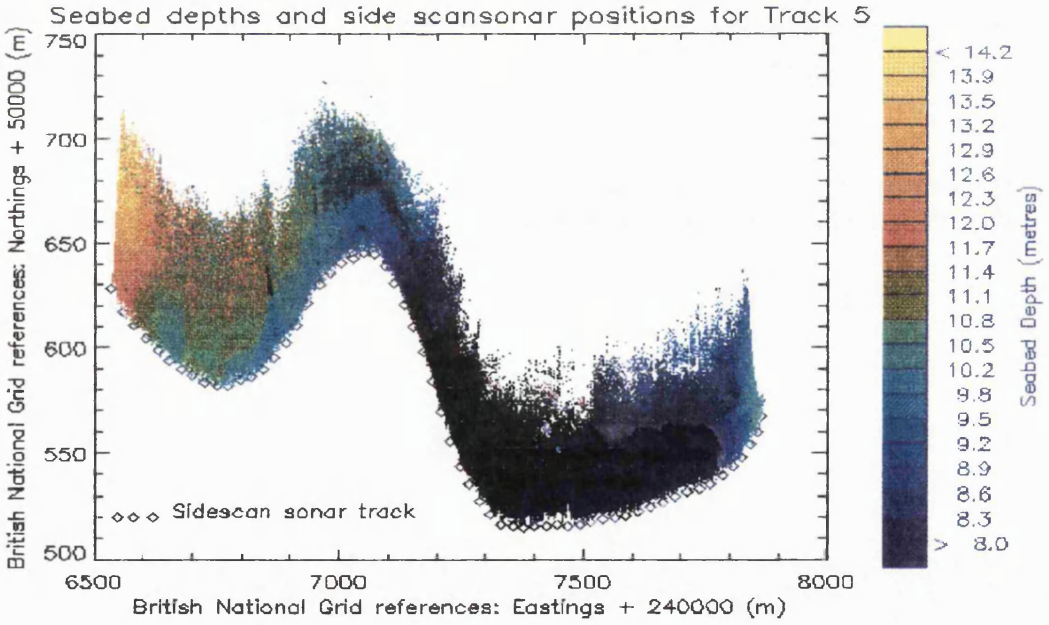

Figure 7.53: A plot of seabed depths with sidescan sonar positions overlaid.

7.7.1 Results for seabed type: Sand

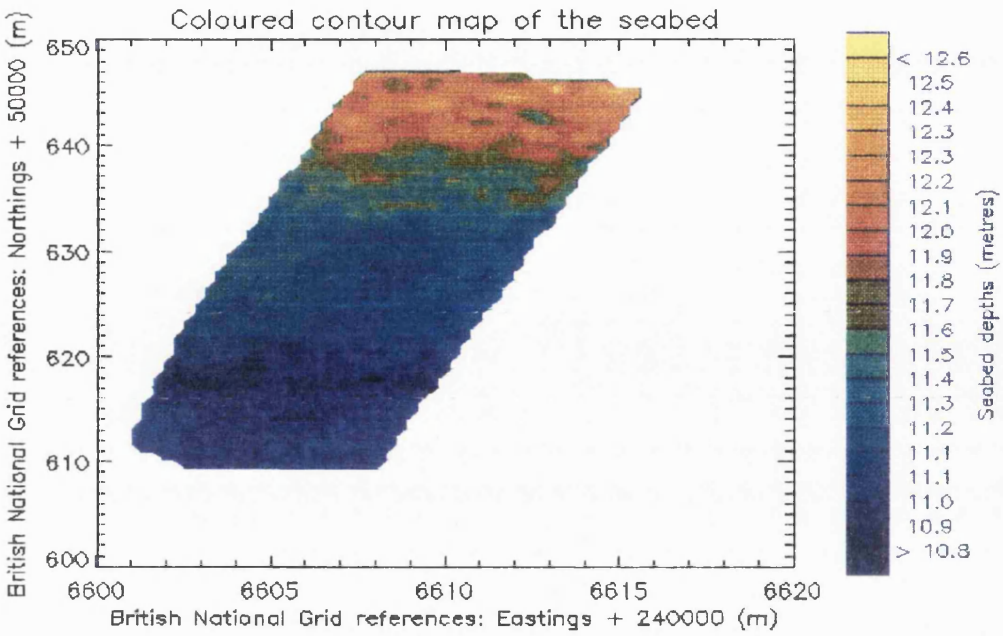

Figure 7.54: Contour plot of the seabed under investigation. Seabed type: Sand

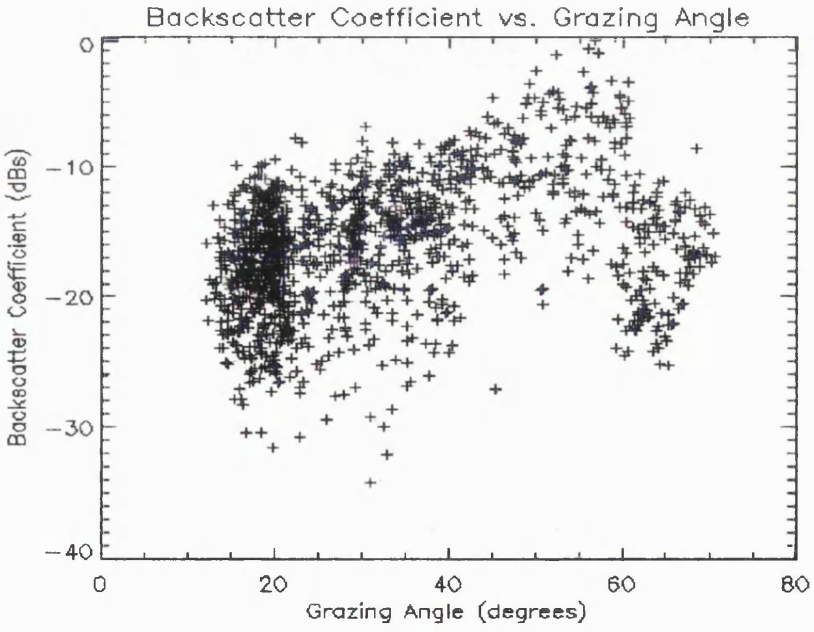

Figure 7.55: A plot of Backscatter Coefficients against Grazing Angle. Seabed type: Sand

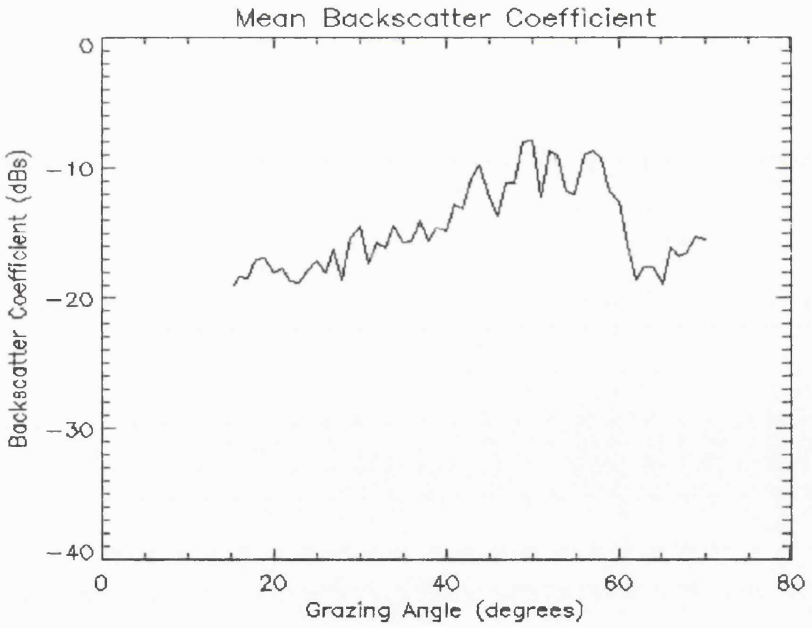

Figure 7.56: A plot of Mean Backscatter Coefficients against Grazing Angle. Seabed type: Sand

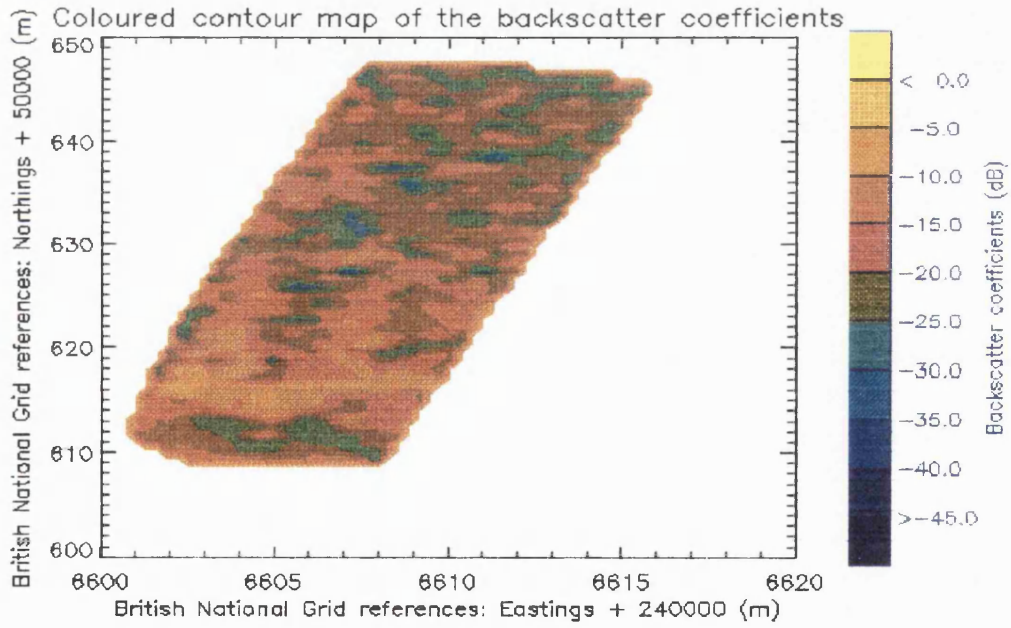

Figure 7.57: Contoured plot of the Backscatter Coefficients. Seabed type: Sand

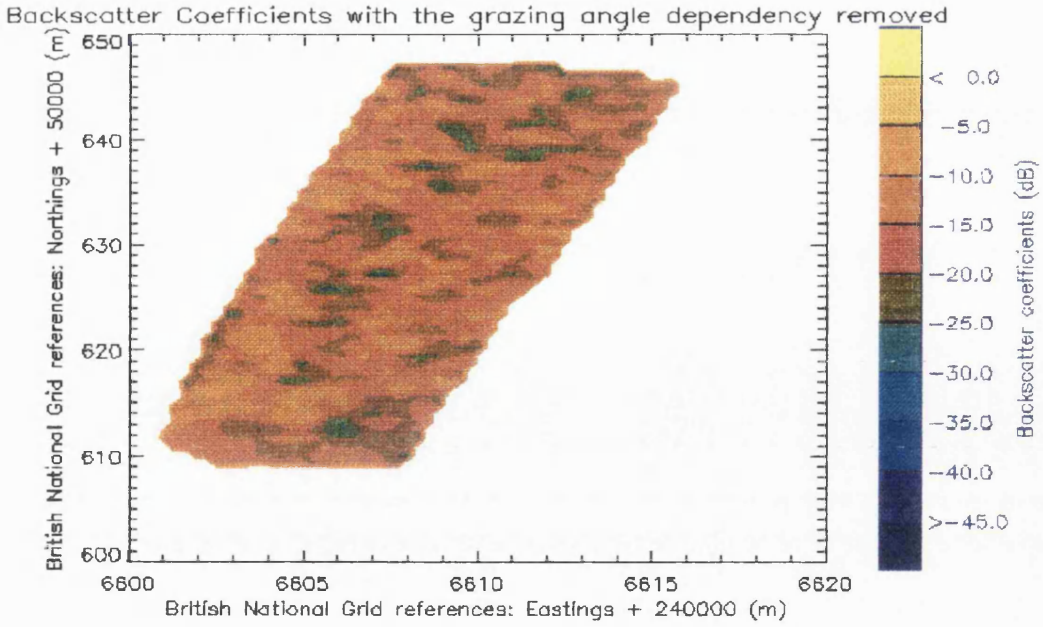

Figure 7.58: Contoured plot of the Backscatter Coefficients with the grazing angle dependency removed. The backscatter values are relative to a grazing angle of 43 degrees. Seabed type: Sand.

7.7.2 Results for seabed type: Fine Sand/Mud

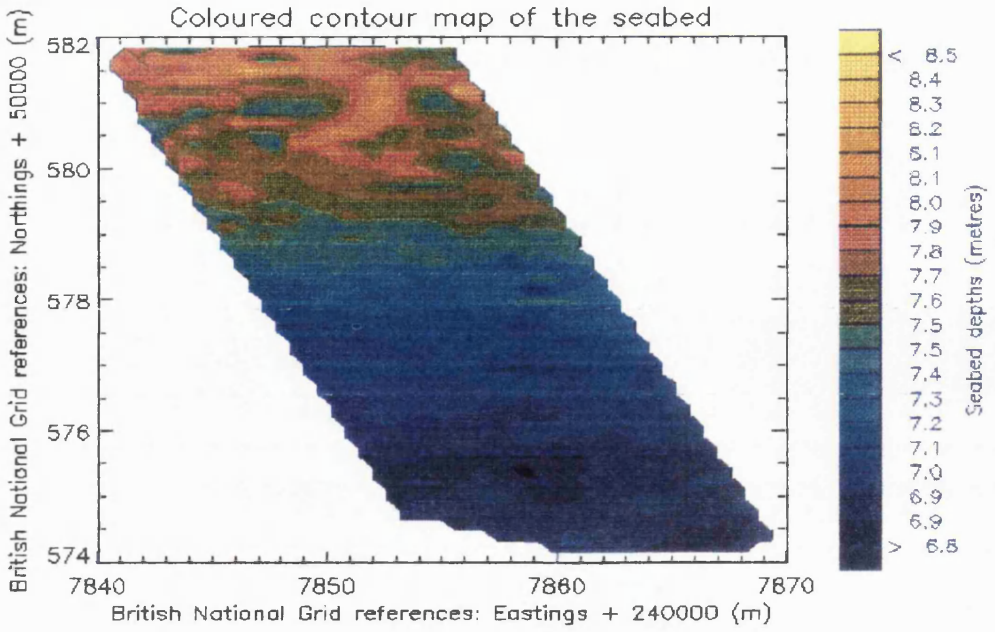

Figure 7.59: Contour plot of the seabed under investigation. Seabed type: fine Sand/Mud

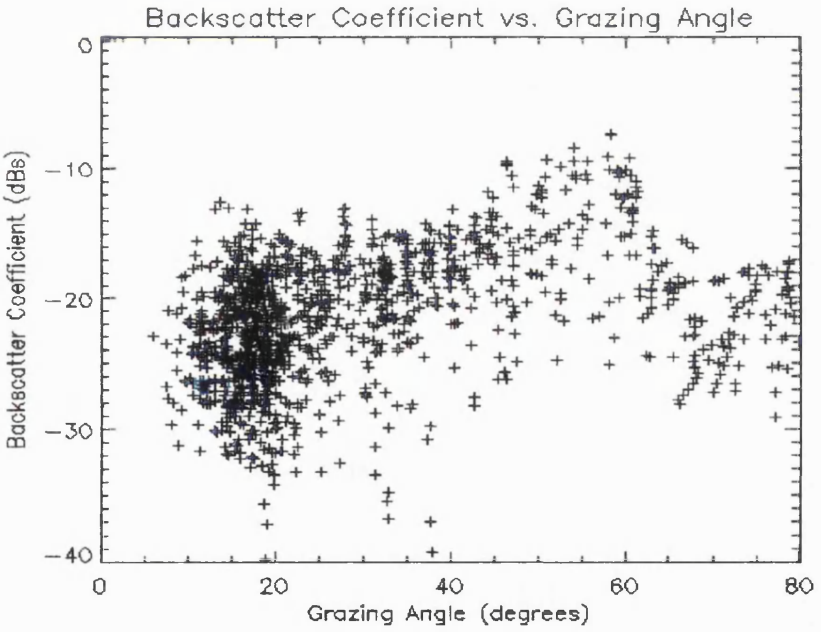

Figure 7.60: A plot of the Backscatter Coefficients against Grazing Angle. Seabed type: fine Sand/Mud

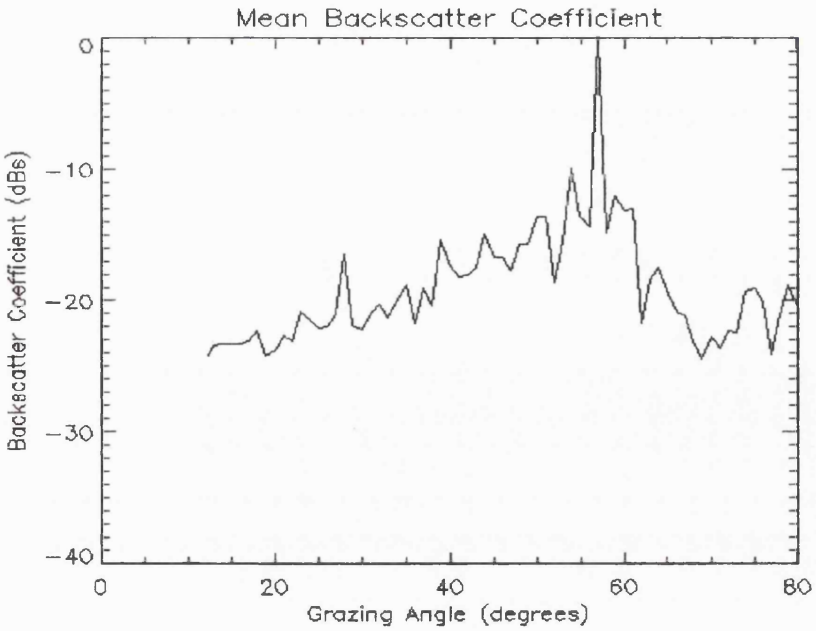

Figure 7.61: A plot of the Mean Backscatter Coefficients against Grazing Angle. Seabed type: fine Sand/Mud

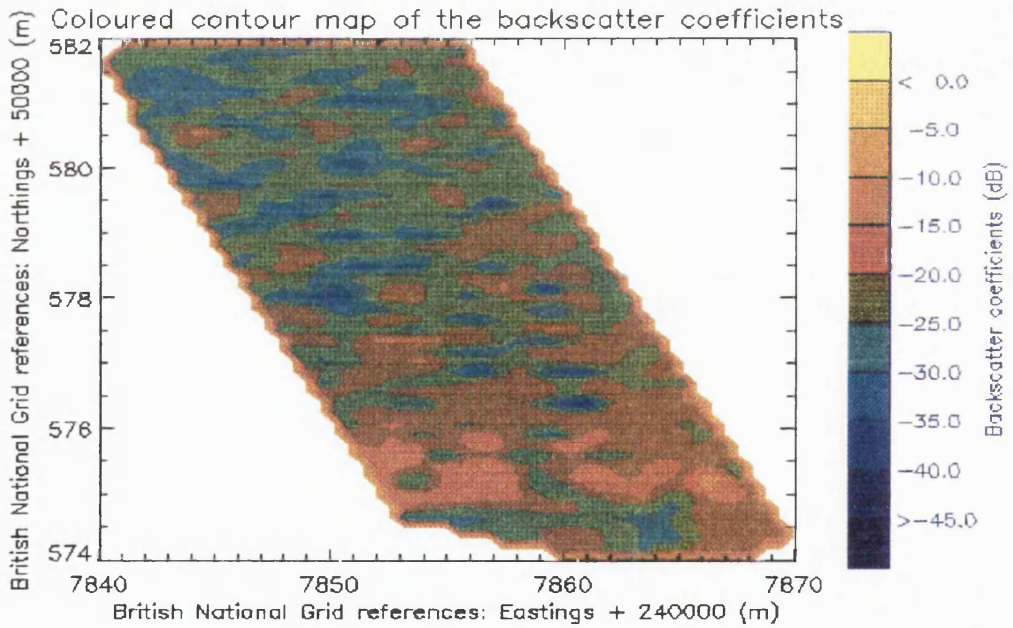

Figure 7.62: Contoured plot of the Backscatter Coefficients. Seabed type: fine Sand/Mud

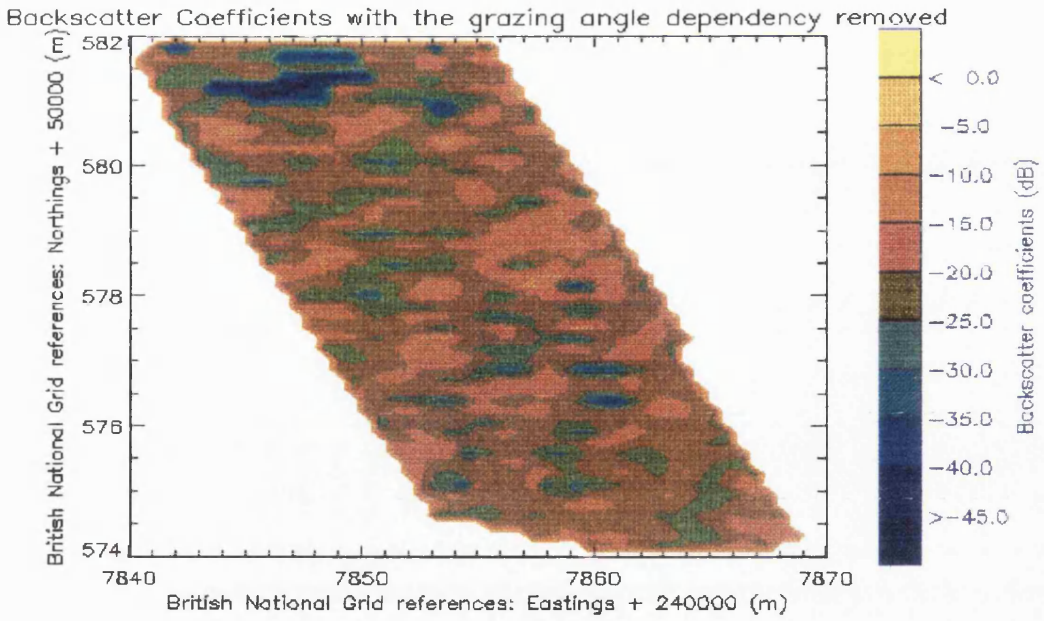

Figure 7.63: Contoured plot of the Backscatter Coefficients with the grazing angle dependency removed. The backscatter values are relative to a grazing angle of 46 degrees. Seabed type: fine Sand/Mud.

7.7.3 Plots covering all of Track 5 data.

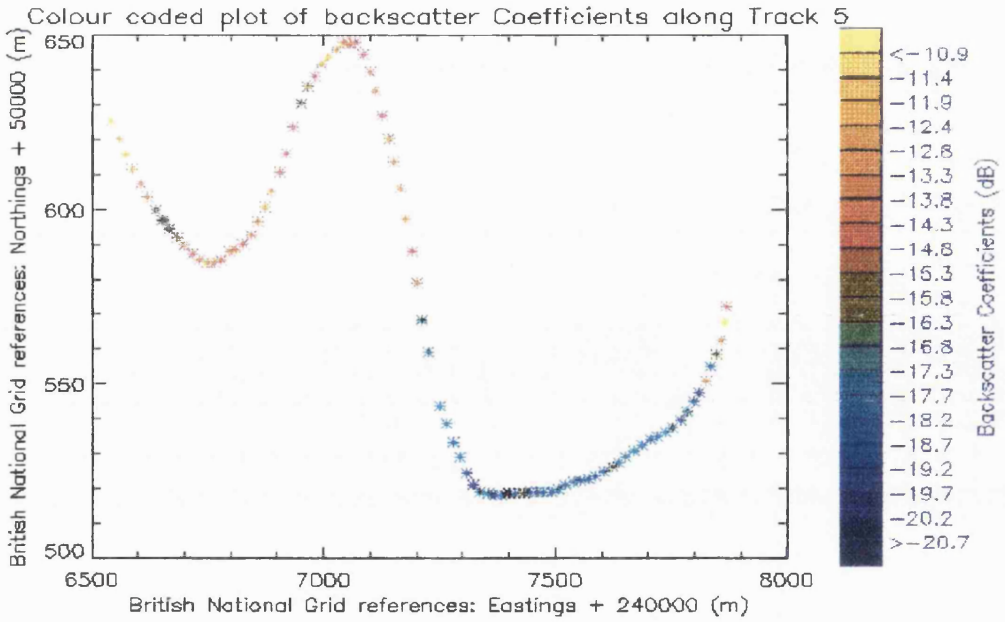

Figure 7.64: Colour coded plot of backscatter coefficient values along Track 5. Each point represents the average backscatter value over all grazing angles for 10 pings.

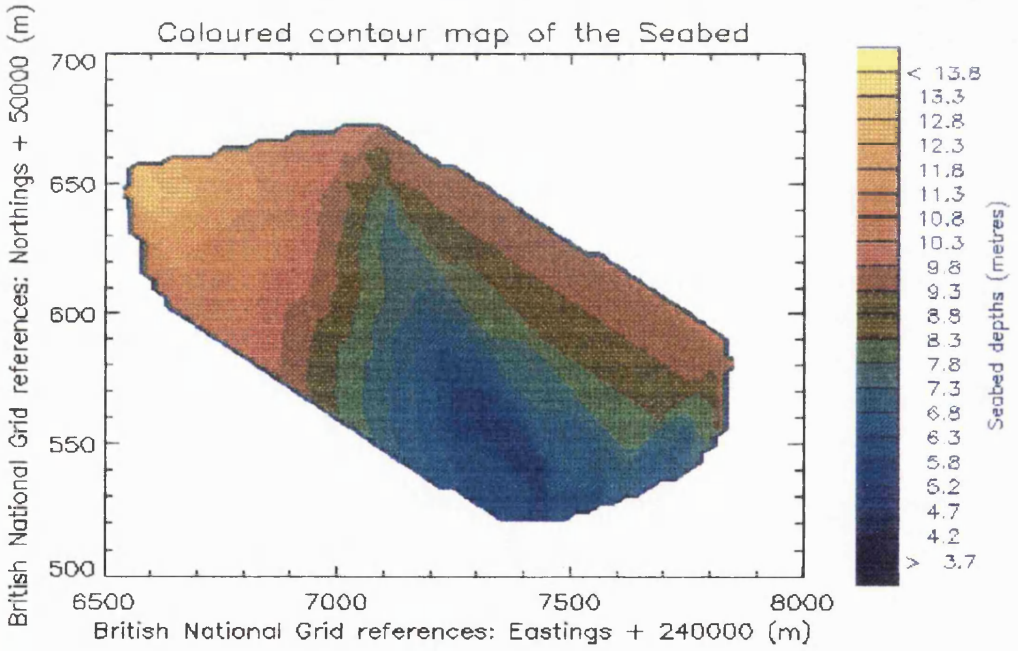

Figure 7.65: Contour plot of the seabed bathymetry for all of Track 5.

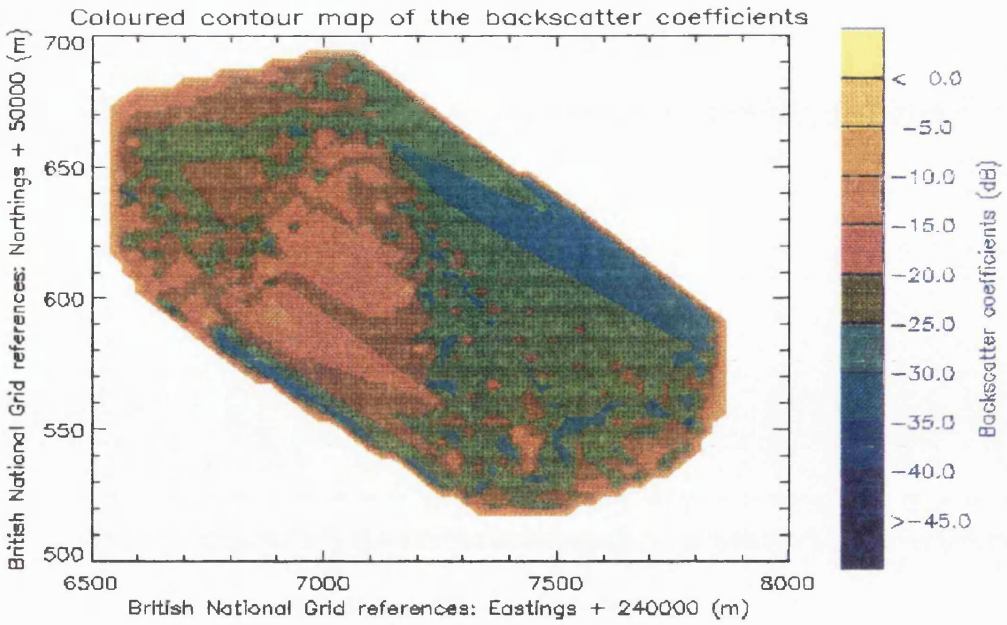

Figure 7.66: Contoured plot of the backscatter coefficients along Track 5, this was achieved by using a sliding window technique.

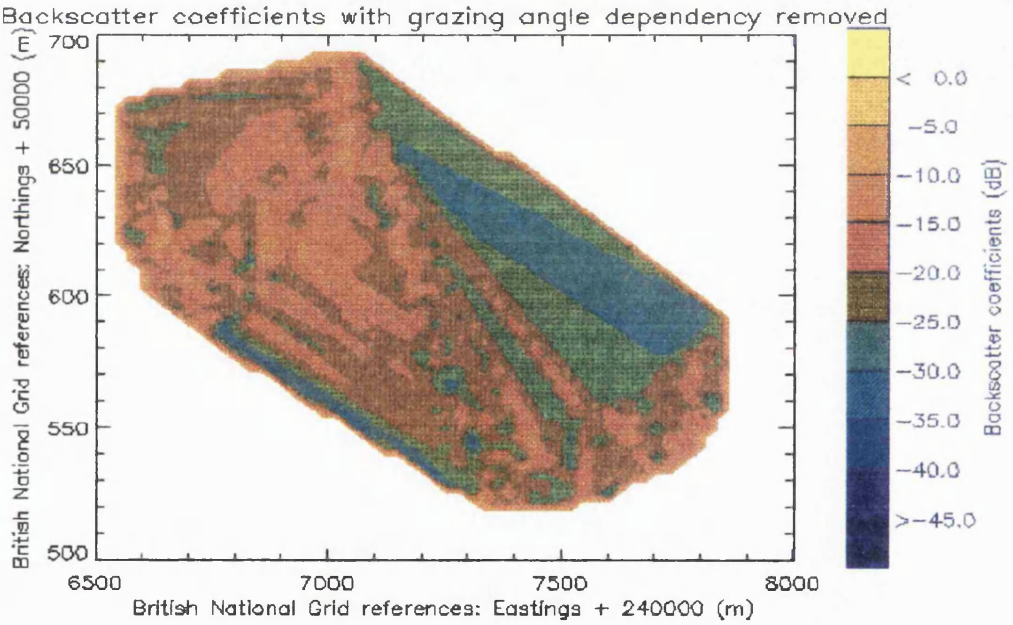

Figure 7.67: Contour plot of the backscatter coefficients with the grazing angle dependency removed. The backscatter coefficient values are relative to the backscatter coefficient value at the middle grazing angle.

7.8 Summary of the results for the 117 kHz Port dataset

Four different seabed types were passed over by Track1 and Track 2. Of the following five figures, the first four show the backscatter coefficients with the grazing angle dependency removed, and the final figure is a summary of all the backscatter coefficients calculated against the grazing angles.

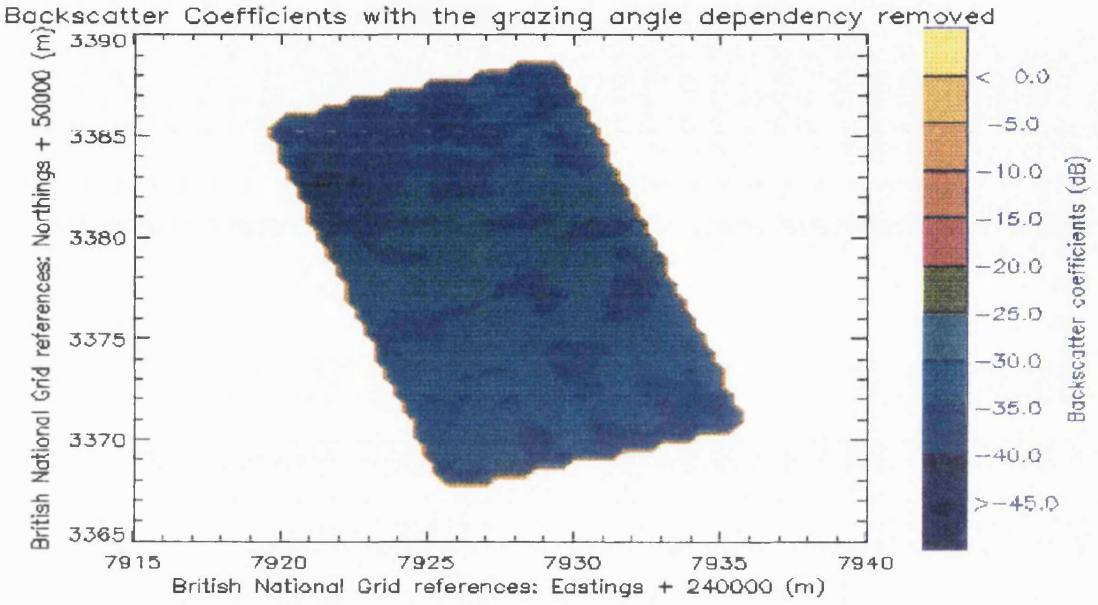

Figure 7.68: Contour plot of Backscatter Coefficients with the grazing angle dependency removed. The backscatter values are relative to a grazing angle of 25 degrees. Seabed type: Mud.

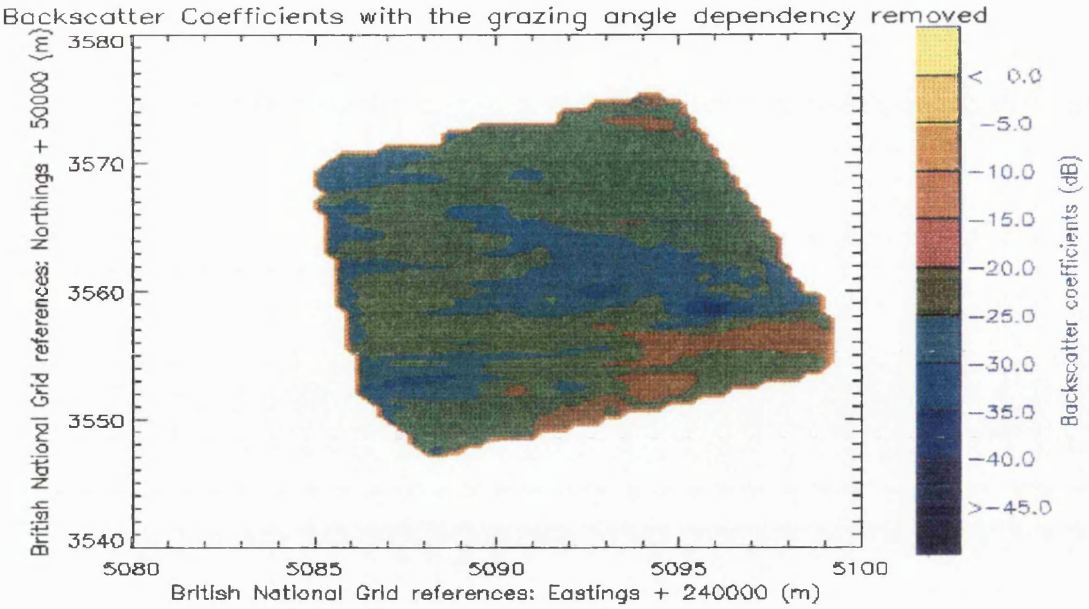

Figure 7.69: Contoured plot of Backscatter Coefficients with the grazing angle dependency removed. The backscatter values are relative to a grazing angle of 28 degrees. Seabed type: Gravel.

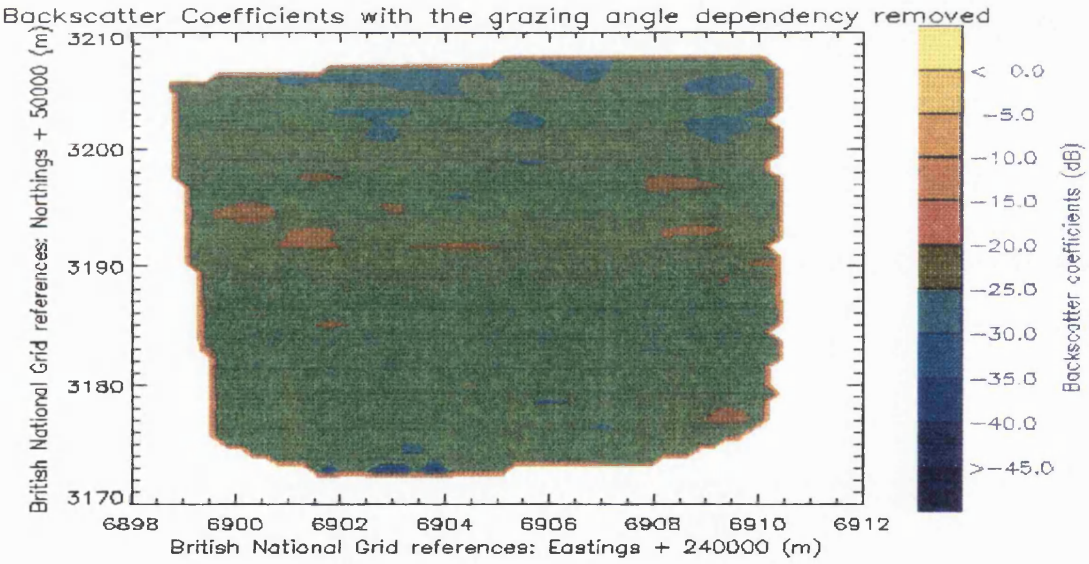

Figure 7.70: Contoured plot of the Backscatter Coefficients with the grazing angle dependency removed. The backscatter values are relative to a grazing angle of 30 degrees. Seabed type: Gravel/Shell/Sand.

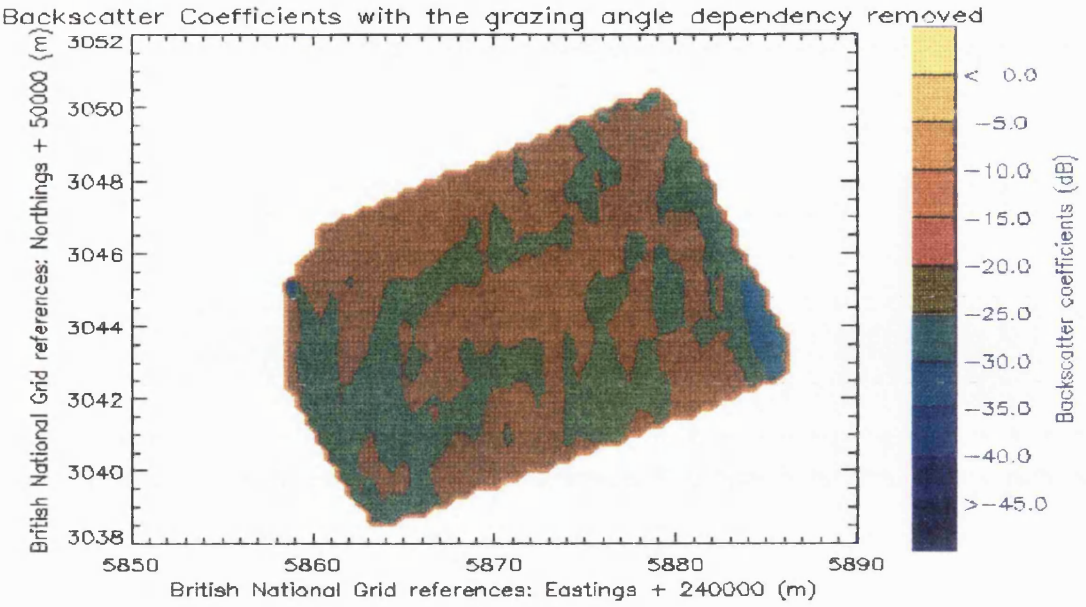

Figure 7.71: Contoured plot of the Backscatter Coefficients with the grazing angle dependency removed. The backscatter values are relative to a grazing angle of 26 degrees. Seabed type: Shell.

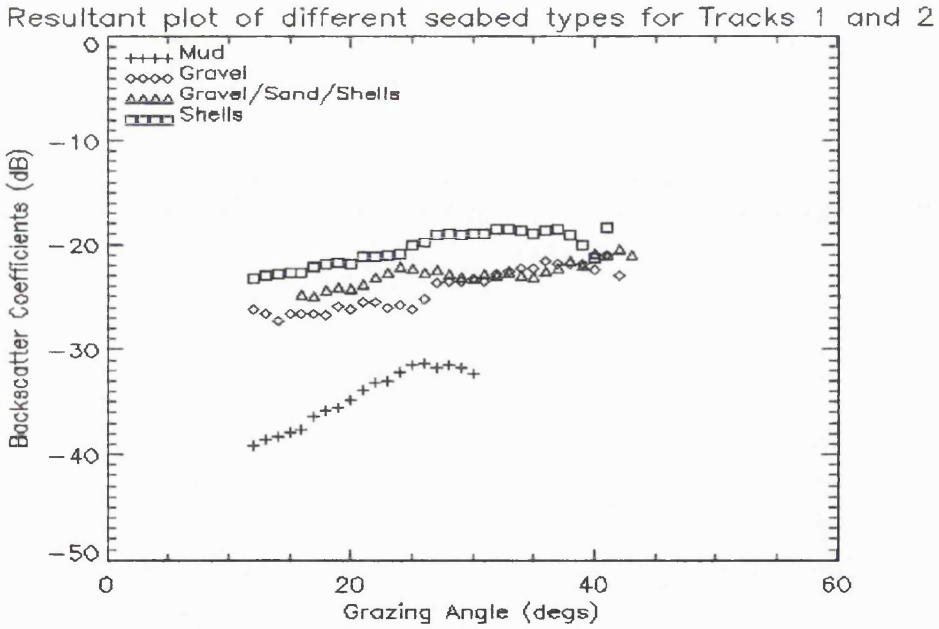

Figure 7.72: Summary of the backscatter coefficients for the 117 kHz Port dataset.

7.9 Summary of the results for the 234 kHz Starboard dataset

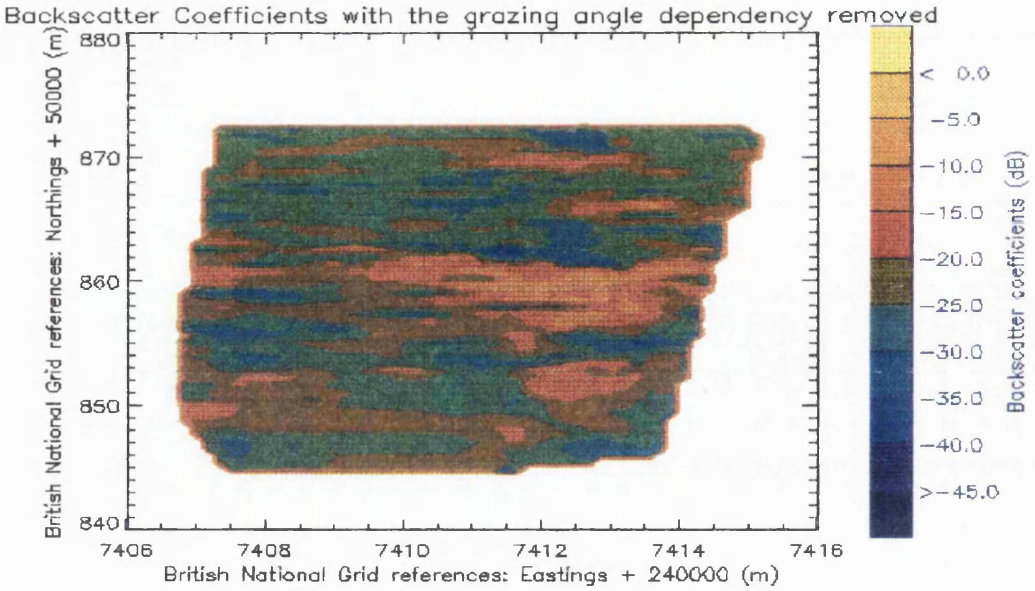

Figure 7.73: Contoured plot of the Backscatter Coefficients with the grazing angle dependency removed. The backscatter values are relative to a grazing angle of 47 degrees. Seabed type: Mud.

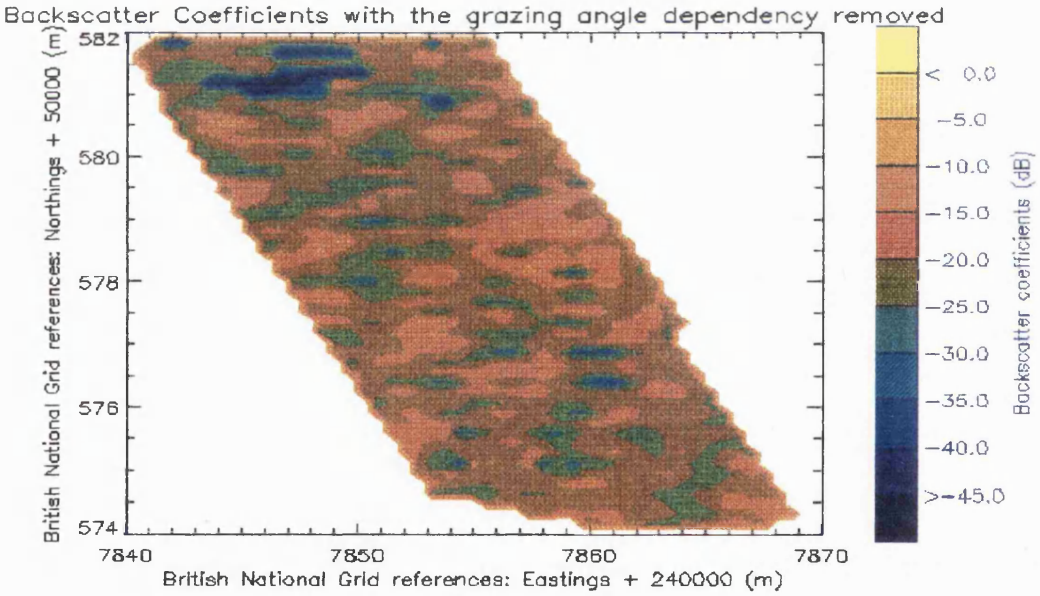

Figure 7.74: Contoured plot of the Backscatter Coefficients with the grazing angle dependency removed. The backscatter values are relative to a grazing angle of 46 degrees. Seabed type: fine Sand/Mud.

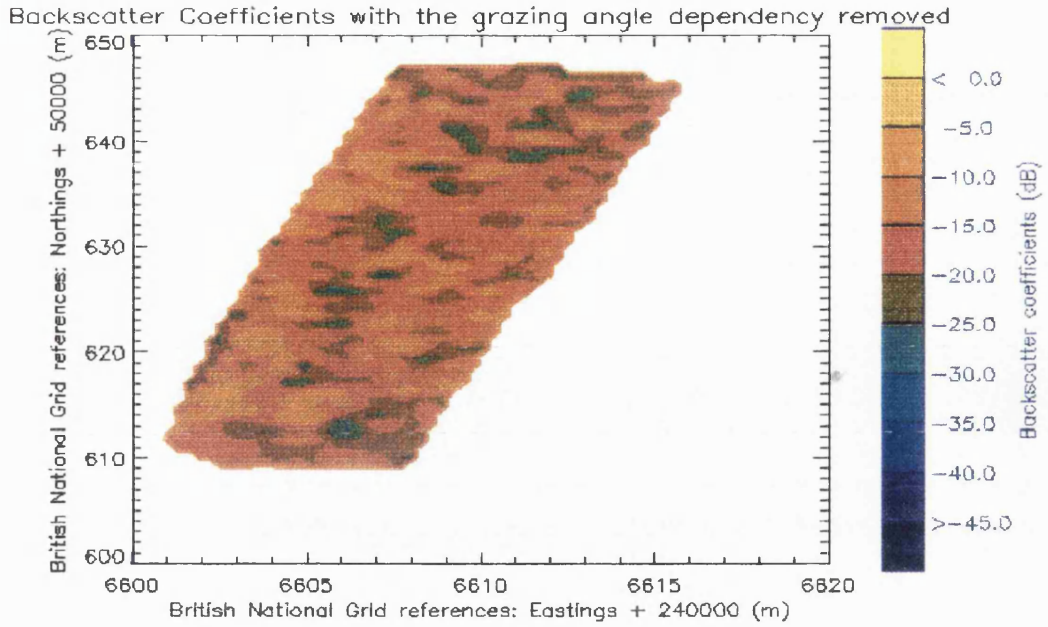

Figure 7.75: Contoured plot of the Backscatter Coefficients with the grazing angle dependency removed. The backscatter values are relative to a grazing angle of 43 degrees. Seabed type: Sand.

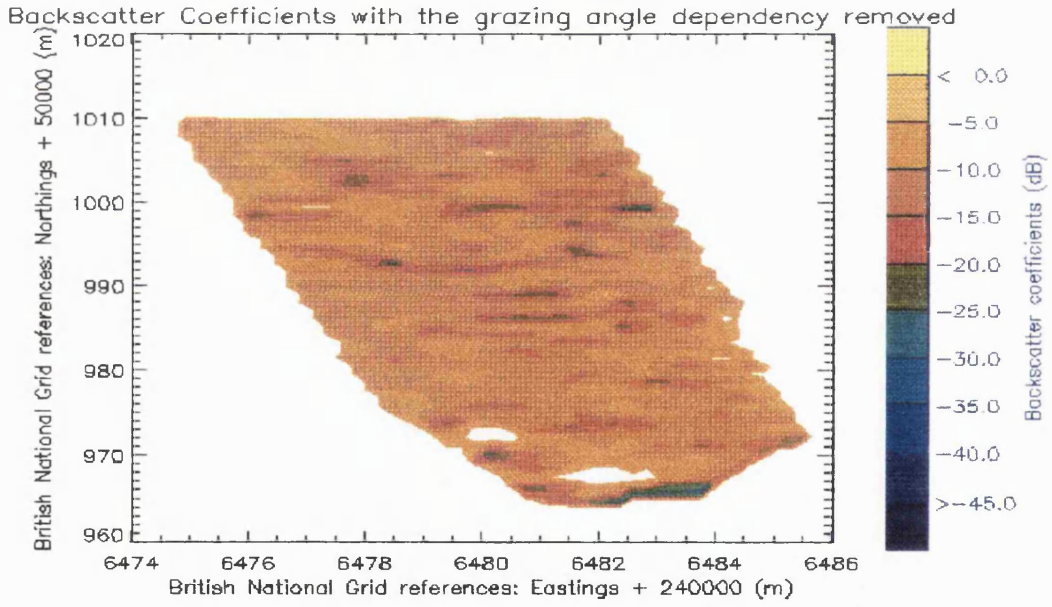

Figure 7.76: Contoured plot of the Backscatter Coefficients with the grazing angle dependency removed. The backscatter values are relative to a grazing angle of 29 degrees. Seabed type: Sand/broken Shell/Gravel.

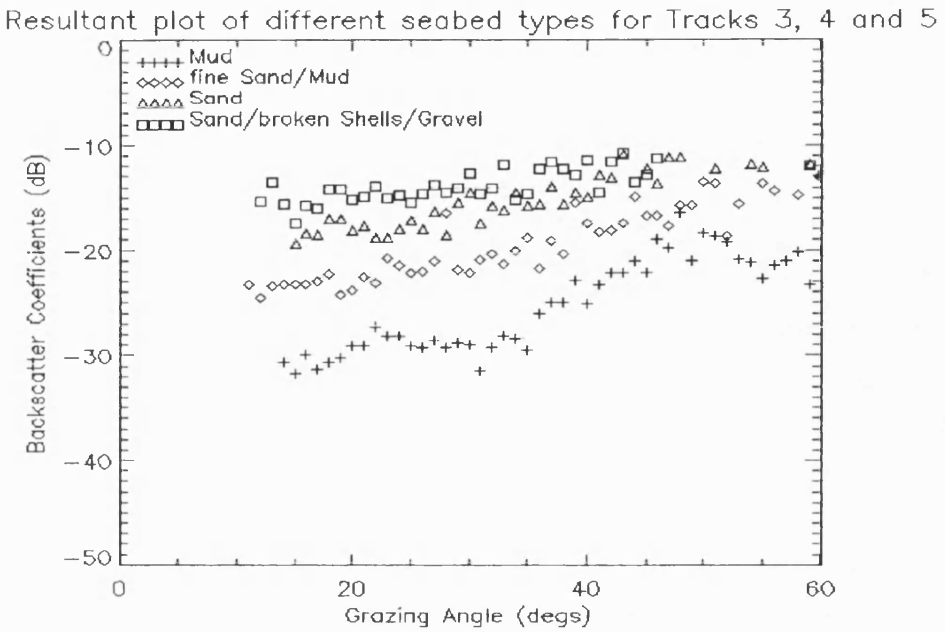

Figure 7.77: Summary of the backscatter coefficient values for the 234 kHz Port dataset.

7.10 Summary of the backscatter coefficients for the Starboard datasets

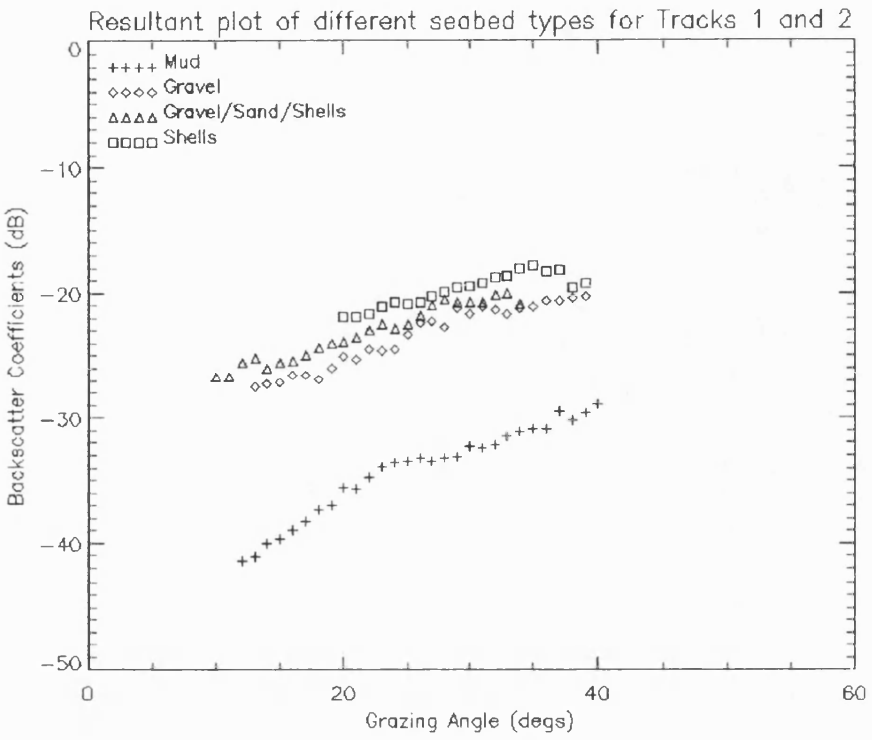

Figure 7.78: Summary of the backscatter coefficient values for the 117 kHz Starboard dataset.

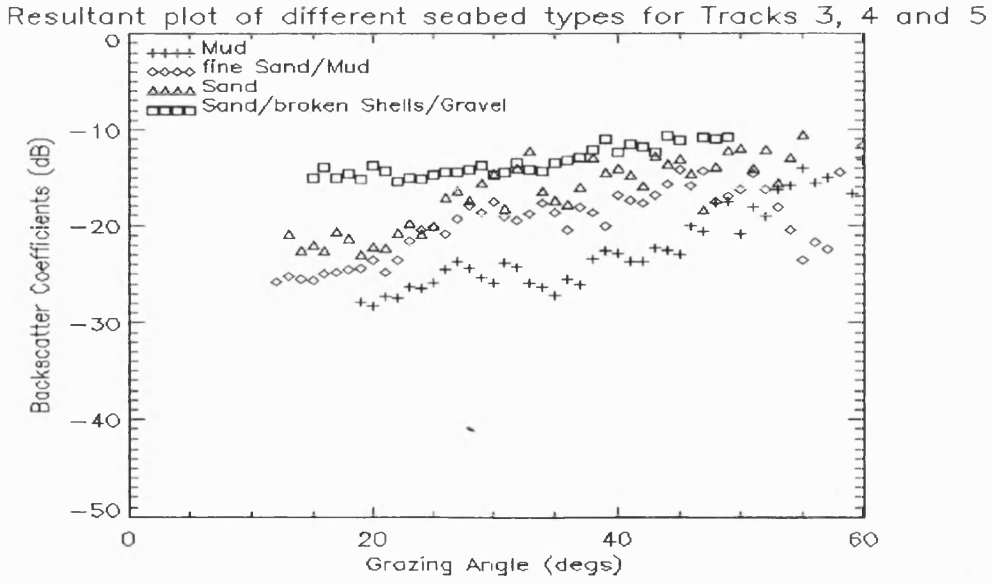

Figure 7.79: Summary of the backscatter coefficient values for the 234 kHz Starboard dataset.

7.11 Discussion of the results

There were seven different seabed types investigated, in eight different locations. All the seabeds investigated had seabed truths associated with them. The analysis of the data was for both the Port and the Starboard side of the sidescan sonar.

For the 117 kHz dataset, the following seabed types encountered were Shell, Gravel/Sand/Sheil, Gravel and Mud. Table 7.1 shows a summary of the results.

For the 234 kHz dataset, the seabed types were Sand/broken Shell/Gravel, Sand, fine Sand/Mud and Mud. Table 7.2 shows a summary of the results.

Seabed Type	Port Dataset	Starboard Dataset
Shell	**-22 dB**	**-22 dB**
Gravel/Sand/Shell	**-24 dB**	**-24 dB**
Gravel	**-26 dB**	**-26 dB**
Mud	**-35 dB**	**-36 dB**

Table 7.1 A summary of the results from the 117 kHz dataset for a grazing angle of 20 degrees. Both the Port and the Starboard results are shown.

Seabed Type	Port Dataset	Starboard dataset
Sand/Broken Shell/Gravel	**-15 dB**	**-14 dB**
Sand	**-18 dB**	**-22 dB**
fine Sand/Mud	**-24 dB**	**-24 dB**
Mud	**-29 dB**	**-29 dB**

Table 7.2 A summary of the results for the 234 kHz dataset for a grazing angle of 20 degrees. Both the Port and the Starboard results are shown.

For the 117 kHz dataset, the difference between the highest backscatter coefficient, which was for Shell, and the lowest backscatter coefficient, which was for Mud, was 14 dB.

For the 234 kHz dataset, the difference between the highest backscatter coefficient, which was for Sand/broken Shell/Gravel, and the lowest backscatter coefficient, which was for Mud, was 15 dB.

Both the Port and the Starboard datasets gave comparable results, for both the 117 kHz and the 234 kHz datasets. The only exception to this was for the 234 kHz analysis of Sand. There was a 4 dB difference in results, this could be due to seabed topography or a different seabed type dominating the results for the Port or Starboard dataset.

The plot for Mud and Gravel/Sand/Shell for the 117 kHz Port dataset shows a drop in the backscatter coefficient value as the grazing angle increases past 28°. This dip might be a demonstration of the effect of exceeding the critical grazing angle, where the acoustic signal can undergo seabed penetration. This effect can also be noticed on the 117 kHz starboard dataset, although it occurs at about 25°.

Overall, the 234 kHz system resulted in higher backscatter coefficients values compared to the range of coefficient values from the 117 kHz system.

Due to the amount of scatter in the backscatter coefficient values for both the Port and the Starboard datasets, it is difficult to detect any dip in the backscatter coefficient values as the grazing angle increases.

The 117 kHz results show a smooth increase in backscatter coefficient values as the grazing angle increases, but the 234 kHz results show a large amount of scatter as the grazing angle increases. This large scatter for the 234 kHz results may be due to seabed topography, or the fact that seabed roughness was comparable, or larger than the wavelength of the 234 kHz system.

One seabed type was common for both the 117 kHz system and the 234 kHz system and that was mud. From table 7.1 and 7.2 the difference in the backscatter coefficient value at 20 degrees was approximately 6 dB, with the 117 kHz system recording the lower value. This could be due to the 117 kHz system undergoing volume attenuation, or the seabed bathymetry affecting the results in the 234 kHz system.
In both cases, Mud was recorded as the lowest value, this is consistent with previous published results.

The removal of the grazing angle bias from the backscatter coefficients contour plots generated a more uniform picture of the seabed under investigation.
The contour plots have an even distribution of values, with patches of high and low backscatter coefficient values easy to see. These high and low could be due to different types of seabed being present or simply a result of the scheme used to colour the backscatter values. If the mean backscatter value lies on the edge of two colours then the scatter in the values will result in a two tone colour contour plot

The most obvious difference between the contour plots for the 117 kHz system and the 234 kHz system is the range of colours used. The 117 kHz contour plot normally consist of two main colours and maybe a third, minor, colour. The 234 kHz contour plot has one main background colour but could have up to 4 other colours on it. This is a result of the large range of backscatter values calculated for the 234 kHz system.
Looking at the resultant contour plots different seabed types can be distinguished, even from the 234 kHz system which has a large scatter in the results.

Chapter 8

Summary and Conclusion

The main aim of this project was to investigate the possibility of classifying the seabed using co-registered bathymetric and backscatter amplitude data from a calibrated interferometric sidescan sonar.

When an acoustic wave strikes the seabed, the backscatter amplitude detected by the receiver is a function of many parameters which include, interface roughness or seabed volume inhomogeneities. Chapter 2 reviewed different theoretical reverberation models for calculating the backscatter coefficient from an area of seabed. The theoretical reverberation models showed a marked dependence of backscatter coefficients to grazing angles less than the critical angle for a wide range of seabed types. The current theoretical reverberation models all showed a good comparison to experimental data.

The experimental data presented in Chapter 2 showed a clear dependence of seabed type to backscatter coefficients at grazing angles that are less than the critical grazing angle. The experimental data showed up to a 25 dB difference in backscatter coefficient going from Clay to Rock. A discussion from published papers illustrated that it is still undecided which seabed reverberation mechanism is dominant, volume or surface reverberation..

The interferometric sidescan sonar used by Submetrix to collect the datasets was presented in Chapter 3. The sidescan sonar has shown itself capable of producing co-registered bathymetric and backscatter amplitude data but, problems still exist with the bathymetric

and backscatter amplitude datasets supplied by Submetrix, these problems were addressed in Chapter 6 and are summarised below.

Poor bathymetric data occurred for two reasons:

1) Submetrix used a fixed gain amplifier, which caused poor depth data at the start and the end of each swath.
2) Poor depth data occurred during the swath due to noise interference, as discussed in Chapter 3.

Both these problems resulted in a pre-processing filter routine that removed any bad data points rather than replacing them.

The backscatter amplitude data was poor for the two reasons:

1) Submetrix accidentally converted the 12-bit backscatter amplitude signal to a 4-bit signal.
2) Due to the error in converting the 12-bit signal to 4-bits, Submetrix used a 75 dB gain on the received signal to get sufficient resolution on the backscatter amplitude signal. This caused the stronger backscatter amplitudes to be clipped.

Pre-processing routines were written so that only good backscatter amplitude data were used, without altering the integrity of the data. One problem that was caused by bit conversion error is that there was very little data at grazing angles below 15 degrees. Most of the theoretical models and experimental datasets published showed a marked dip in the backscatter coefficient values below a grazing angle of 15 degrees, this trend cannot be seen in this thesis using the datasets supplied by Submetrix.

The sonar equation, which the acoustic model was based on, was discussed in Chapter 3. The sonar equations were used to calculate the relationship between the reverberation signal and the unwanted background noise. The individual terms and meanings were discussed before a simple sonar equation was developed to show how an acoustic signal was affected as it traveled from the sidescan sonar transmitter, interacted with the seabed and was received. Building on this simple sonar equation, Chapter 5 showed how the simple sonar equation was used to generate an acoustic model, which was used to calculate the backscatter coefficients for different types of seabeds.

A digitised map of Plymouth Sound was generated and the seabed truth location gained from the Admiralty Chart, 1995 and Fitzpatrick, 1991, entered. The track of the sidescan sonar was plotted onto this map and the locations of where the sidescan sonar passed over an area of seabed truth noted. These areas, or subsets of the data, were isolated and the backscatter coefficients for these areas of seabed's were calculated using the acoustic model.

The acoustic model relied on the fact that the sidescan sonar system was calibrated and could generate co-registered bathymetric and sidescan sonar data. Using the calibration data, the transmit intensity and the receive intensity at the sidescan was calculated. The transmit intensity used the transmit beam pattern and the transmit sensitivity, the receive intensity used the receive beam pattern and the receiver intensity. The use of the beam pattern took into account the motion of the sidescan sonar, which was discussed in Chapter 4.
The area of seabed insonified and the slant range of this area of seabed needed to be calculated, Chapter 5 showed how the acoustic model was developed and how each of the parameters were calculated.

Once the acoustic model was developed a method was devised for calculating for each backscatter coefficient, a grazing angle. Chapter 6 showed how the theory of vector cross-product and the dot-angle product generated the relevant grazing angles. Chapter 6 also showed the steps required to analyse a small area of seabed and the resulting figures were used to display different types of seabeds.

The backscatter coefficients calculated by the acoustic model were dependent upon the grazing angle. When a contour plot of the results was generated it resulted in a 'false' picture of the backscatter coefficient values for that area of seabed in that there remained a grazing angle dependence. The resultant contour plot showed high backscatter coefficient values always occurring near the sidescan sonar with the backscatter coefficients decreasing away from the sidescan sonar.

A method was devised to remove this grazing angle dependency. The backscatter coefficients were all plotted relative to one backscatter coefficient value at the middle grazing angle. Different methods were tried with little discernible difference in results were observed, the above method was chosen due to ease of operation, and the result of this can be seen in Chapter 6.

There were seven different seabed's investigated, in eight different locations. All these seabeds had seabed truths associated with them taken from the Admiralty Chart, 1995 and Fitzpatrick, 1991. Analysis of the data was for the Port and the Starboard side of the sidescan sonar.

For the 117 kHz dataset, the following seabed types encountered were Shell, Gravel/Sand/Shell, Gravel and Mud. The difference between the highest mean backscatter coefficient, which was for Shell, and the mean lowest backscatter coefficient, which was for Mud, was 13 dB. Table 7.1 showed a summary of the results.

For the 234 kHz dataset, the seabed types were Sand/broken Shell/Gravel, Sand, fine Sand/Mud and Mud. The difference between the mean highest backscatter coefficient, which was for Sand/broken Shell/Gravel, and the mean lowest backscatter coefficient, which was for Mud, was 14 dB. Table 7.2 showed a summary of the results.

The 117 kHz dataset consisted of a calibrated dataset, however, the 234 kHz dataset was uncalibrated. Submetrix could only supply beam patterns, transit and receive sensitivities from another 234 kHz system. This affected the backscatter coefficient values, and, unlike the 117 kHz results, the values for the 234 kHz system were not absolute values but relative values.

Both the Port and the Starboard datasets gave comparable results, for both the 117 kHz and the 234 kHz systems. The only exception to this was for the 234 kHz analysis of Sand. There was a 4 dB difference in results, this could be due to seabed topography or a different seabed type dominating the results for the Port or Starboard dataset.

One seabed type was common for both the 117 kHz system and the 234 kHz system and that was Mud. From table 7.1 and 7.2 the difference in the mean backscatter coefficient value at 20 degrees was approximately 6 dB, with the 117 kHz system recording the lower value. This could have been due to the 117 kHz system undergoing volume attenuation, or the seabed roughness affecting the results in the 234 kHz system.
In both cases, Mud was recorded as the lowest value, this was consistent with previous published results.

The plot of the mean backscatter coefficient against grazing angle for Mud and Gravel/Sand/Shell for the 117 kHz Port dataset, Figure 7.72, showed a drop in the backscatter coefficient value as the grazing angle increases past 28°. This dip might have been a demonstration of the effect of exceeding the critical grazing angle, where the acoustic signal can undergo seabed penetration. This effect can also be noticed on the 117 kHz starboard dataset, Figure 7.78, although it occurs at about 25°.

Due to the amount of scatter in the mean backscatter coefficient values for the 234 kHz, Port and the Starboard datasets, it was difficult to detect any dip in the backscatter coefficient values as the grazing angle increases.

The range of backscatter values calculated for different seabed types using the 117 kHz system were relatively small, about 3 dB about the mean backscatter coefficient value, which resulted in a smooth increase in the mean backscatter coefficient values as the grazing angle increased, however, the 234 kHz system had a range of backscatter coefficient values between 5 dB and 10 dB about the mean backscatter coefficient value, this resulted in a large amount of scatter as the grazing angle increases. This large scatter for the 234 kHz results may be due to seabed topography, or the seabed roughness was comparable, or larger than the wavelength of the 234 kHz system.

The removal of the grazing angle bias from the backscatter coefficients by relating the values to one backscatter coefficient at the middle grazing angle resulted in a uniform picture of the seabed under investigation.

The contour plots had an even distribution of values, with patches of high and low backscatter coefficient values easy to see. These high and low could be due to different types of seabed being present or simply a result of the scheme used to colour the backscatter values. If the mean backscatter value lies on the edge of two colours then the scatter in the values will result in a two tone colour contour plot.

The most obvious difference between the contour plots for the 117 kHz system and the 234 kHz system is the range of colours present. The 117 kHz contour plot would normally consist of two main colours and maybe a third, minor, colour. The 234 kHz contour plot would have one main background colour but, four other colours could be present. This was a result of the large range of backscatter values calculated for the 234 kHz system. Looking at the resultant contour plots different seabed types could be distinguished, even from the 234 kHz system which had a large scatter in the results.

The aim of this project was to try and devise a method which could detect different seabed types using co-registered bathymetric and backscatter amplitude data from an Interferometric sidescan sonar. Seven different seabed types were distinguished using two different frequencies, 117 kHz and 234 kHz.
This thesis presented an acoustic model that could calculate the backscatter coefficient for an area of seabed and a technique for calculating the grazing angle, which related to the backscatter coefficient.
Due to limitations in the data supplied the acoustic model could not be used to classify the seabed at low grazing angles .

As the acoustic model has a modular structure, any co-registered bathymetric and backscatter amplitude data from a calibrated interferometric sidescan sonar can be easily entered into the model, and the backscatter coefficients for the area of seabed analysed are presented in a line plot or a colour coded contour plot with the topographic effects removed.

The results obtained using Submetrix's sidescan sonar for the area of seabed investigated should be repeatable and comparable with any results obtained from other datasets using a

similar frequency, calibrated, interferometric sidescan sonar. The resulting graphic displays which show the backscatter coefficients as colour coded contours, has a algorithm where a range of backscatter coefficient values will always have the same colour associated with it. This would mean that if another system used the acoustic model presented in this thesis, then the same colours would be presented for the same seabed types, which would give an easy to compare graphics display package.

In the colour coded contour plots which show the backscatter coefficient values with the topographic effects removed, for the whole of the dataset, it is easy to see how different seabed types can be detected. A good example of this can be seen in Figure 7.12, where the seabed changes from a mixture of Gravel/Shells/Sand to Mud.

With more data, and more accurate seabed truthing, it should be possible to create a database to which an unknown area of seabed could be compared to determine the seabed type. This could be achieved by taking a few mean backscatter coefficient values at certain grazing angles and compare these to the database, another method could be take the mean backscatter coefficient value over the area of seabed under investigation, with the topographic effects removed, and compare this value with the database.

Due to the limitations in the data supplied by Submetrix, the following work needs to be undertaken to provide more confidence in the results:

1) Submetrix should repeat the datasets but with the 234 kHz going over the area covered by the 117 kHz system and vice versa. This would show if the area of seabed covered by the 234 kHz appeared rough to the system.
2) 234 kHz dataset from a calibrated sidescan sonar is required.
3) When Submetrix cure the 12-bit to 4-bit problem, then the model needs to be run on a complete range of backscatter amplitude data with low grazing angle data presented.
4) A sea-trial with the sidescan sonar needs to be carried out in Plymouth Sound with seabed truthing carried out as the data is collected, as this would be the only way that the seabed type for the data would be known.

5) A wider range of seabed could be investigated, Plymouth Sound has a wide range of seabed types and a sea-trial should be organised which could cover the whole range of seabed types.

6) The tracks should be repeated again, this would give more certainty to the results.

References

Admiralty Charts, 1973, "Symbols and abbreviations used on Admiralty Charts", Hydrographic Department, 1973.

Admiralty Chart Number 1967, 1995, " England-South Coast: Plymouth Sound", Hydrographic Department, 1995.

Alexandrou D. and Michalopoulou Z. H., 1992, "On sidescan bathymetry: The slope effect and a method for reducing phase ambiguities", Feb 1992

Alexandrou, D. and Pantzartzis D., 1993, "A Methodology for Acoustic Seafloor Classification", IEEE J. Oceanic Engineering, Vol 18, No 2, April 1993

Babb R. J., 1989, " Feasibility of interferometric swath bathymetry using GLORIA, a long range sidescan", IEEE Oceanic Eng., Vol OE-14, No 4, pp289-298, 1989

Bachmann W, 1973, "A theoretical model for the backscattering strength of a composite roughness sea", J. Acoust. Soc. Am., 54, 712-716, 1973

Barrick D.E. and Peake W.H., 1968, "A review of scattering from surfaces with different roughness scales", Radio Sci, 3, 865-868, 1968

Bass F.G. and Fuks I.M., 1979, "Wave scattering from Statistically Rough Surfaces", (Oxford: Pergamon)

Beck R. A., 1991, "Automatic sea bed classification using Sidescan Sonar", I. O. A., 1991

Beldenson R. H., 1972, " Sonographs of the sea floor", Elsevier publishing company, Amsterdam, 1972

Bell J., 1995, "A model for the simulation of sidescan sonar", Thesis, Herriot-Watt University, 1995.

Boehme H.,1985, "Acoustic backscattering at low grazing angles from the ocean bottom. Part I. Bottom backscattering strength", J. Acoust. Soc. Am., Vol 77, No 3, pp962-974, March 1985

Boehme H. and Chotiros N.P., 1988, " Acoustic backscattering at low grazing angles from the ocean bottom", J. Acoust. Soc. Am., Vol 84, No 3, pp 1018-1029, September 1988

Brekhovskikh L.M. and Lysanov Yu.P., 1991," Fundamentals of Underwater Acoustics", Springer-Verlag

Brown G.S., 1978, "Backscattering from a gaussian distributes perfectly conducting rough surface", IEEE Trans. Ant. Prop., AP-26, 472-482 (corrections in AP-28 943-946, 1980)

Burdic W.S., 1984, "Underwater Acoustic system analysis", Prentice-hall

Cervenka P. and de Moustier C., 1993, "Sidescan Sonar Image Processing Techniques", IEEE Journal of Oceanic Engineering, Vol 18, No 2, pp108-122, April 1993

Chesterman, W.D.,Clynick, P.R. and Stride, A.H., 1958, "Acoustic aid to seabed survey",Acoustica 8:285-290, 1958.

Chesterman W.D., Quinton J.M.P, Chan Y.and Matthews H.R.,1967, "Acoustic surveys of the sea floor near Hong Kong," Inst Hydro, Rev., vol 44 no 1, pp35-54, 1967M.

Chotiros N. P., 1985, " Acoustic backscattering at low grazing angles from the oean bottom. Part II. Statistical characteristic of bottom backscatter at a shallow water site", J. Acoust. Soc. Am., 77, (3), pp975-982, March 1985

Chotiros N. P., 1994, "Reflection and reverberation in normal incidence echo-sounding", J. Acoust. Soc Am, 96, (5), Pt 1, pp2921-2929, November 1994

Hughes Clarke J.E., 1993, "Processing and interpretation of 95kHz backscatter data from shallow-water multibeam sonars", IEEE Oceans 93, pp437-442, 1993

Clay C.S. and Medwin H., 1977, "Acoustical Oceanography", J.Wiley and Sons

Cloet R. L., Edwards C. R., Duncan A. J., 1985, "The University of Bath Swath Sounding System", Proc. Inst. Acoustics, Vol 7, Pt3 1985.

Cloet R. L. and Edwards C. R., 1986, "The Bathymetric Swathe Sounding System", Internat. Conf. Oceanology SUT, Vol 6, pp401 - 413, 1986

Coates R. F. W, 1990, "Underwater Acoustic Systems", Macmillan New Electronics book, chapter 9, pp158, 1990

Czarnecki M. F., 1979, " An application of pattern recognition techniques to side scan sonar data", IEEE 1979.

Davis E. E., 1986, " The use of swath bathymetric and acoustic image mapping tools in marine geoscience", MarineTech, Soc., J., Vol 20, No 4, pp17-27, 1986

de Moustier C, 1988, "State of the art I swathe bathymetry survey systems", Int Hydr. Rev., Vol 65, No 2, pp25-54, 1988

de Moustier C, Lonsdale P. F., and Shor, A. N., 1990a, "Simultaneous operation of the seabeam multibeam echo sounder and the SeaMARC II bathymetric sidescan sonar system", IEEE J. Oceanic Eng., Vol OE-15, No 2, pp84-94, 1990a

de Moustier C., Matsumoto H. and Shor A., 1990b, "Open ocean acoustic calibration of the SeaMARC Iibathymetry sidescan sonar system", Proc IEEE Oceans '90, Washington D.C., pp523-527, 1990b

de Moustier C and Matsumoto H, 1993, "Seafloor acoustic remote sensing with multibeam echo-sounders and bathymetric sidescan sonar systems", Marine Geophysical Researches 15:pp27-42, 1993

Denbigh P.N., 1977, " Phase only sidescan sonar for underwater mapping", Acoust Lett, Vol 1, 84-87, 1977

Denbigh P.N., 1979, " A bathymetric sidescan sonar", Proc Ultrasonics Int Conf., pp321-326, 1979

Denbigh P.N., 1980, "Glint and its effects on the accuracy of a Sea Bed Profiling Sonar", Proc. of the Inst. of Acoustics, pp 7.1 - 7.8, 1980

Denbigh P.N., 1981, " Stereoscopic visualization and contour mapping of the seabed using BASS", Proc. IERE Conf, No 51, pp291-311, 1981

Denbigh, P.N. 1983, "Stereoscopic visualisation and contour mapping of the sea bed using a bathymetric side-scan sonar (BASS)", The radio and Electronic Engineer, Vol 53, No 7/8, pp301-307 1983.

Denbigh P. N., 1989, "Swarth Bathymetry: Principles of Operation and an Analysis of Errors", IEEE Oceanic Eng., Vol OE-14, No 4, pp289 - 298, 1989.

Donovan D. T. and Stride A. H., 1961, " An acoustic survey of the sea floor south of Dorset and its geological interpretation", Philos. Trans. R. Soc., B244, pp299-330, 1961.

Edgecock T.M., 1994, " Towards gain invariant sea bed classification", ", Proc Inst Acoustics, Vol 16, Pt 6,pp217-224, 1994

Ellis D.D., 1993, "Ocean reverberation", Kluwer academic Pubs., 1993

Ewing, M, Vine, A.C., and Worzel, J.L. 1946, "Recent results in submarine geophysics",Geol. Soc. Am. Bull. 57 :909-934

Fahrentholz S., 1963, "Profile of area echograph for surveying and location of obstacles in watreways", Int. Hyd. Rev., 40, 1, pp23-37, 1963.

Fitzpatrick F., 1991, "Studies of sediments in a tidal environment", Thesis, Polytechnic South West, 1991.

Flemming B. W., Klein M., Denbigh P. N., 1982, "Recent developments in side scan sonar techniques", W.G.A Russell-Cargill book, Chapter 5, pp103 - 138, 1982

Fortuin L, 1970, " Survey of literature on refelction and scattering of sound waves at the sea surface", J. Acoust. Soc. Am., 47, 1209-1228, 1970

Gallagher N.C., Wise G. L., 1981, "A Theoretical Analysis of the Properties of Median Filters", IEEE Transaction on Acoustics, Speech, and Signal Processing, Vol ASSP-29, No 6, pp1136-1141, December 1981

Galybin N.N., 1976, "Backscattering of sound by a disturbed sea surface", Sov. Phy. Ac., 22, 193-197, 1976

Gapper G.R. and Hollis T., 1985, "The accuracy of an Interferometric Sidescan Sonar", Proc Inst. Acoustics, Vol 7, Part 3, pp126 - 134, 1985

Geen M.F., Hewitt P.D. and Adams A.R., 1993, "The ISIS Interferometric Seabed Inspection Sonar", Proc I.. O. A ,Vol 15, Part 2, pp187-194, 1993

Glenn M. F., 1970, "Introducing an operational multi-beam array sonar", Int. Hyd. Rev., 47, 1, pp35-39, 1970.

Greischar L. L. and Clay C. S., 1972, "Use of side-scanning sonar for contouring bottom features", J. Acoust. Soc. Am., 51, 3, pp1073-1075, 1972.

Haines R. G., 1963, "Developments in ultrasonic instruments", Int. Hyd. Rev., 40, 1, pp49-57, 1963.

Haines R. G., 1970, "Searoom for the super-tanker", Navy, 75, 6, pp189-190, 1970.

Haralick R.M., Shanmugam K. and Dinstein I, 1973, " Textural features for Image Classification", IEEE Transactions on Systems, Man, and Cybernetics, Vol SMC-3, No 6, Nov 1973

Heaton J.P. and Haslett W.G., 1971, "Interpretation of Lloyd mirror in sidescan sonar," Proc Soc Underwater Tech., vol 1, no 1, pp24-38, 1971

Hersey J. B., 1960, "Sonar uses in Oceanography", Instrument Society of Americal conference pre-print, Instrument Automation Conference, 21-Ny-60, NY 1960

Hickley T. J., 1966, "Narrow-beam transducer sounding system", Int. Hyd. Rev., 43, 1, pp37-42

Horton C.W.Sr and Muir T.G., 1967,"Theoretical studies on the scattering of acoustic waves from a rough surface", J, Acoust. Soc. Am., Vol 41, No 3, 627-634, 1967

Horton C.W.Sr, 1967," Model studies on the scattering of acoustic waves from a rough surface", J, Acoust. Soc. Am., Vol 41, No 3, 635-643, 1967

Howson E. A., and Dunn J. R., 1961, "Directional echo-sounding", J. Inst. of Navy, 14, 3, pp348-359, 1961.

Jackson D. R., 1986a " Application of the composite roughness model to high-frequency bottom backscattering", J. Acoust. Soc. Am., 79 (5), pp1410-1422, May 1986

Jackson D. R., 1986b " High-frequency bottom backscatter measurements in shallow water", J. Acoust. Soc. Am, 80, (4), pp1188-1199, October 1986

Jackson D.R., Briggs K. B., 1992, "High-frequency bottom backscattering: Roughness versus sediment volume scattering", J. Acoust. Soc. Am., Vol 92, No 2, Pt 1, pp962-977, August 1992.

Jackson D. R., 1994, "Models for scattering from the sea bed", Proc Inst Acoustics, Vol 16, Pt 6, pp161-172, 1994.

Kalra A. K. and Fulford J. K., 1994, " Analyses of direct path, low frequency, monostatic reverberations from exposed rocks and sediment covered areas of the ARSRP fine scale experiment", ", Proc Inst Acoustics, Vol 16, Pt 6,pp173-180, 1994.

Kinsler L.E. and Frey A. R., 1962, "Fundamentals of Acoustics", 2nd Ed. J.Wiley and Sons, 1962.

Kunze, W. 1957, "General aspects of application of horizontal echo sounding method to shipping", Int. Hydrography. Rev. 34:63-72, 1957.

Kuryanov B.F., 1963, "The scattering of sound at a rough surface with two types of irregularity", Sov. Phys. Ac., 8, 252-257, 1963

Lesnikowski N. S., 1989, "Deep towed interferometric swathe mathymetry", Oceans 89 IEEE Conf, pp1130-1133, 1989

Lindsay, R.B 1973, "Acoustics - Historical and Philosophical Development", Dowden, Hutchinson and Ross, Stroudsberg, 1973.

Mackenzie K.V., 1961, " Bottom reverberation for 530- and 1030 Hz sound in deep water", J. Acoust. Soc. Am, 33, pp1498-1504, 1961.

Masnadi-Shirazi M.A., de Moustier C. 1992, " Differential phase estimation with the SeaMARC II bathymetric sidescan sonar system", IEEE J. Oceanic Eng., Vol 17, No 3, pp239-251, July 1992

Matsumoto H., 1990, " Characteristics of SeaMARC II phase data", IEEE J. Oceanic Eng., Vol 15, No 4, pp350-360, Oct 1990

Mazel C., 1985, "Sidescan training manual", Klein Associates Inc., 1985.

McDaniel S.T. and Gorman A.D., 1982, "Acoustic and radar sea surface backscatter", J. Geophys. Res., 87, 4127-4136, 1982

McDaniel S.T. and Gorman A.D., 1983, "Examination of the composite-roughness scattering model", J.Acoust. Soc. Am., 73, 1476-1486, 1983

McKinney C. M. and Anderson C. D., 1964, "Measurements of Backscattering of Sound from the Ocean Bottom", J. Acoust. Soc. Am., Vol 36, No 1, Jan 1964

Mitchell N.C. and Somers M. L., 1989, " Quantitative backscatter measurements with a long-range side-scan sonar", IEEE J. Oceanic Eng, Vol 14, No 4, pp368-374, 1989

Mitchell N.C. and Hughes Clarke J, 1994, " Classification of seafloor geology using multibeam sonar data from the Scotian Shelf", Marine Geology, 121, pp143-160, 1994

Mourad P.D. and Jackson D.R.,1989, "High frequency sonar equation models for bottom backscatter and forward loss", MTS/IEEE Oceans 89, conf., 4, pp1168-1175, 1989

Murphy L., 1995, " Standardising seabed classification techniques", 36(7), pp15-19, 1995

Nicholls, M.J.A., 1991, "Automatic Seabed Classification using Sidescan Sonar", U. D. T., 1991

Nolle A.W., 1963, "Acoustical properties of water-filled sands", J. Acoust. Soc. Am., Vol 35, No 9, 1392-1408, 1963

Ogilvy J.A., 1991, "Theory of wave scattering from random rough surfaces", Adam Hilger, 1991

Ol'shevskii V.V., "Statistical methods in Sonar", 1978

Pace N.G. and Dyer C.M., 1979, "Machine Classification of Sedimentary Sea Bottoms", IEEE Transactions on Geoscience Electronics", Vol. GE-17, No.3, 52-56, 1979

Pace N.G., 1985, "The range dependence of normal incidence acoustic backscatter from a rough surface", J. Acoust. Soc. Am., Vol 77, No 1, 101-112,1985

Pace N.G. and Gao H., 1988, "Swathe Seabed Classification", IEEE Journal of Oceanic Engineering, Vol 13, No 2, 83-90, 1988

Pace N.G., 1990, "Acoustics backscatter and seabed characteristics", Proc. Inst. Acoustics, Vol 12, Pt1, 21-32, 1990.

Pace N. G., 1992, "Expression for the time varied gain in a sidescan sonar", July 1992

Pace N. G., 1994, "Low frequency acoustic backscatter from the seabed", ", Proc Inst Acoustics, Vol 16, Pt 6,pp181-188, 1994

Rayleigh Lord, 1945, "The theory of sound", New York:Dover (first edition 1877, New York: Macmillan)

Reed T.B. and Hussong D.M., 1989, " Quantitative analysis of SeaMARC II side-scan sonar imagery", J. Geophys Res., 94, B6, pp7469-7490, 1989

Robinson L.J and Bjorkheim O.I., 1989, " Interferometry-an alternate methodin sonar mapping", Oceans 89 IEEE Conf, pp1134-1135, 1989

Reut Z, Pace N.G. and Heaton M.J.P., 1985, "Statistical Properties of Sidescan Sonar Signals and the Computer Classification of Sea-Beds", Proc. Inst. Acoustics, Vol 7, Pt.3, 102-107, 1985

Ritchie G. S., 1970a, "British hydrography since Cook" The naval review, 58, 1, pp126-134, 1970

Ritchie G. S., 1970b, "Problems in bathymetric surveying presented by modern trends in ship building", The radio and electronic engineer, 40, 5, pp219-224, 1970

Shensa M. and Black C., 1978," Passive Bearing estimation: The removal of bias and 2π ambiguities", J. Acoust Soc Am, Vol 63(1), Jpp 91 - 100, Jan 1978

Shishido M. and Naito K., 1979, " A study on picture improvement for side looking sonar", NEC Research and Development, No 53, pp62-74, April 1979

Skolnik, M.I., 1962,"Introduction to radar systems," chap 12, McGraw-Hill Book Company, New York, 1962

Smailes I.C., 1978, "Bottom Reverberation measurements at low grazing angles in the NE atlantic and Mediterranean Sea", J. Acoust. Soc. Am., Vol 64, No 5, pp1482 - 1486, Nov 1978.

Somers M.L. and Stubbs A. R., 1984, "Sidescan Sonar", IEEE Proceedings, Vol 131, Part F, No 3, pp243 - 256, June 1984

Stanic S. and Briggs K.B., 1988, " Shallow-water high-frequency bottom scattering off Panama City, Florida", J. Acoust Soc Am., Vol 83, No 6, pp2134-2144, June 1988

Stanic S. and Briggs K.B., 1989, "High-frequency acoustic backscattering from a coarse shell ocean bottom", J. Acoust Soc Am., 85, (1), pp125-136, January 1989

Stewart R. A. and Chotiros N. P., 1992, " Estimation of sediment volume scattering cross section and absorption loss coefficient", J. Acoust. Soc. Am, 91, (6), pp 3242-3247, June 1992

Stewart W. K., 1994, " Quantitative seafloor characterization using a bathymetric sidescan sonar", IEEE J. Oceanic Eng, Vol 19, No 4, pp 599-610, Oct 1994

Stride A. H., 1959, "A linear pattern on the sea floor and its interpretation", J. Mar Biol. Assoc. UK, 38, pp313-318, 1959.

Stubbs A. R., 1974, "Telesounding, a method of wide swathe depth measurement", Int. Hyd. Rev., 51, pp23-59, 1974.

Tamsett, 1993, " Seabed characterisation and classification from the power spectra of side-scan sonar data", Marine Geophysical researches, 15, pp43-64, 1993

Thorne P.D., and Pace N.G., 1984," Acoustic studies of broadband scattering from a model rough surface", J. Acoust. Soc. Am., Vol 75, No 1, 133-144, 1984

Tucker D. G., 1960, "Directional echo-sounding", Int Hyd. Rev., 37, 2, pp43-53, 1960.

Tucker D.G., and Gazey B.K., 1966, "Applied underwater acoustics", Pergamon press, 1966

Tucker M. J., 1961, "Beam identification in multiple echo-sounders", Int. Hyd. Rev., 38, 2, pp25-32, 1961.

Tucker, M.J. and Stubbs, A.R. 1961, "A narrow-beam echo-ranger for fishery and geological investigations",Britsh J. Appl. Phys. 12:103-11, 1961

UCDWR, 1946, " Reverberation", NDRC summary Technical report, Division 6, Vol 8, Pt 2, pp247-342, 1946

Urick R.J., 1954, " The backscattering of sound from a harbor bottom", J. Acoust. Soc. Am., 26, pp231-235, 1954

Urick R.J., 1956, " The processes of sound scattering at the ocean bottom and surface", J. Marine Res, 15, 134, 1956.

Urick R.J. and Saling D.S., 1962, " Backscattering of explosive sound from the deep-sea bed", J. Acoust. Soc. Am., 34, pp1721-1724, 1962

Urick R.J., 1967, "Principles of underwater sound for engineers", McGraw Hill, 1967

Urick R.J., 1982, "Sound propagation in the sea", Peninsula Pubs., 1982

Wong How-Kin, Chesterman W. D., 1968,"Bottom Backscattering near Grazing Incidence in Shallow Water", J. Acoust. Soc. Am., Vol 44, No 6, pp1713 - 1718, Dec 1968.